The Flow Physics Around a 4-wheel Landing Bogie Associated with Noise

by

Barry S. Lazos

Presented to the Graduate and Research Committee

of Lehigh University

in Candidacy for the Degree of

Doctor of Philosophy.

in

Mechanical Engineering

Lehigh University

April, 2000

Approved and recommended for acceptance as a dissertation in partial fulfillment of the requirements for the degree of Doctor of Philosophy

Date

Dr. Donald O. Rockwell
Dissertation Director

Accepted Date

Committee Members:

Dr. Donald O. Rockwell
Committee Chairman

Dr. Sudhakar Neti

Dr. Alparslan Öztekin

Dr. Charles R. Smith

Dr. Richard N. Weisman

Acknowledgments

Most of all I want to thank my wife and kids for allowing me to leave them for a year so I could complete my course work on campus. That was a really hard time for me and I know it was for them too. They also deserve credit for not complaining about the long hours I spent at NASA doing my research and writing my dissertation. I love you guys and owe you a lot.

I would also like to thank NASA for supporting me financially through this process, with a special thanks to my branch head, Bill Sellers, for allowing me to spend so much time on this project without interruption. I also want to thank all of my colleagues at NASA who helped me accomplish this work. Among these are Julian Roberson for helping me build the water channel and Bobby Gaddy for his help with the wind tunnel experiments. Dr. Chung-Sheng Yao and Keith Pascal are very much appreciated for their valuable guidance during DPIV setup and data reduction, and Kurt Severance was a big help with representing the experimental results in a way that was easier to analyze and present. Ben Anders, an especially dear friend, was always a valuable resource during data analysis. His fluids experience and natural curiosity made him a joy to talk with and figure things out.

I also very much appreciate the help of my advisor, Prof. Donald Rockwell, who's wisdom and advise made this accomplishment possible. Finally, I want to thank my committee members for the time they spent on me and the insight they provided me.

Table of Contents

List of Figures

Abstract

The mean flow field around a four-wheel landing gear bogie has been studied in an effort to identify regions of flow noise production. Two different models and facilities, with different experimental techniques, were used. Each of the models consisted of a simplified version of a Boeing 757 main landing gear.

Initial studies were conducted in a water channel using a 13% scale model at a Reynolds number of 15,000. Qualitative flow visualization techniques were used to identify general flow field characteristics. Results indicate the gap region between the in-line wheel is potentially important; the turbulent wake from the wing-side of the fore wheel passes through the gap to the ground-side of the wheels. Evidence was discovered to suggest that separation characteristics on the wing- and ground-sides of the fore wheel have a significant effect on the flow characteristics in the gap region.

More detailed studies were conducted in a wind tunnel using a 31% scale model, at a Reynolds number of 600,000. Experimental techniques included oil flow visualization, mean static pressure measurements, and Digital Particle Image Velocimetry (DPIV). Topological analysis of the surface streamline patterns identified combinations of basic patterns that are not currently addressed in the literature. DPIV results identified a vortex that persists in the gap region between the in-line wheels. Evidence is also provided which indicates this vortex does not remain stationary within the gap region. Regions of flow separation and attachment are defined using DPIV. These regions confirm the interpretation of the surface

separation and attachment patterns obtained with oil flow visualization. These regions are likely associated with significant noise production.

1 Introduction

1.1 Background

For nearly three decades aircraft noise has been a primary concern in the development of the civil aviation industry. In 1970, due to environmental concerns, the Federal Aviation Administration (FAA) established flyover noise level restrictions and guidelines for future noise limits. During the following year, a Joint DOT-NASA (1971) study on civil aviation research and development found that aircraft noise was the largest single impediment to the growth of the civil aviation industry. The two major sources of aircraft noise are the engines and the airframe, with engine noise currently the most prominent. Yet advancing technologies promise to soon reduce engine noise to levels below airframe noise. Gibson (1972) noted that the rapid development and implementation of such technologies make airframe noise "the ultimate noise barrier."

Airframe noise results from pressure fluctuations created by interactions between the aircraft surface geometry and the surrounding fluid. The noise generation mechanism(s) associated with a particular region depends on the incoming flow characteristics and the local development of the flow structure. Flow noise produced by aircraft components usually involves turbulent flow and is associated with one or more of the following mechanisms: turbulent boundary layer flow, steady and unsteady wake flow, turbulent inflow and vortex instability and deformation. An understanding of the flow physics around a particular airframe component is important in order to gain an understanding of the associated mechanisms of noise generation. Such an understanding will allow for effective noise prediction and development of noise reduction techniques.

Landing gear assemblies are considered a significant source of airframe noise. In fact, recent studies show landing gear is a dominant source of airframe noise for some modern aircraft such as the Boeing 777 (Sen, 1996). A literature review bye the author suggests that multiple wheel-set configurations are noisier than single wheel-set configurations. Figure 1.1 is an example diagram of a 4-wheel landing gear configuration.

The geometric complexity of landing gear configurations has thus far precluded an adequate knowledge of the surrounding flow field. Specifics of the associated noise generation mechanisms are also unknown. The present study considers a simplified version of a 4-wheel landing gear bogie modeled after the main landing gear on a Boeing 757. The purpose of the investigation is to determine mean flow field characteristics around the wheels that are associated with noise production. This information can then be used to improve noise prediction schemes and prescribe noise reduction methods.

1.2 Research Motivation

1.2.1 Noise Prediction Considerations

During the 1970's, an intense research interest developed in the area of airframe noise. At that time, most of the effort was directed toward the development of noise prediction schemes. These schemes are classed as either total aircraft or component schemes. Total aircraft schemes utilize flyover noise data gathered from aircraft in various configurations to predict noise levels for aircraft not included in the data set (Healy, 1974; Gibson, 1974; Hardin et al., 1975; Putnam et al., 1975; and Fink, 1977). While these schemes are somewhat successful, they rely entirely on empirical data for their predictions and disregard the flow physics associated with the noise.

The more refined component schemes predict total aircraft noise by summing the calculated noise of individual sources. The drag-element method developed by Revell is based on the hypothesis that sound generated by an object in a flow is related to the steady-state drag it experiences (Revell et al., 1975). The distributed-source analysis method, advanced primarily by Hayden (Hayden et al., 1975), is based on flow noise theory (Lighthill, 1952; Lighthill, 1954; Curle, 1955) and relates the fluctuating forces on a body to the subsequent spectrum of radiated sound pressure. It is considered by some to be closest to the actual physical noise generating mechanisms since it requires that the source mechanism at each component be identified (Heller and Dobrzynski, 1978).

The literature suggests that the primary fluid dynamic sources of undercarriage gear noise are turbulent inflows and wakes. Bluff body wakes are known to produce compact dipole noise fields and result from landing gear components such as wheels, axles, struts, and shafts (Crighton, 1991). Turbulent inflows impacting a rigid surface produce pressure fluctuations that manifest themselves as dipole-like sources (Hayden et al., 1975). Landing gear components are often impacted by turbulent wakes from upstream components that are either outside of or within the landing gear system. The collective wake of landing gear components can also be responsible for enhanced noise levels at locations downstream, when it impacts aircraft components such as deflected flaps or engine nacelles (Preisser, 1980; Herkes and Stoker, 1998).

To gain fundamental insight into the frequency content of the noise field generated by landing gear, we can consider bluff body wake noise only and assume that each component sheds a simple two-dimensional wake. At low Reynolds numbers, the components will produce a fairly narrowband frequency, which can be scaled on their diameter. As Reynolds number increases, shedding becomes increasingly random and the frequency band broadens (Bliss & Hayden, 1976). Therefore, we expect a landing gear system comprised of various diameter components to radiate a fairly broadband noise spectrum with the low-frequency region dominated by the wheels and the high-frequency region dominated by the remaining smaller diameter components (Hayden et al., 1975).

As mentioned above, landing gear systems are composed of many different components, some of them geometrically complex. Therefore it may be advantageous to idealize the system to provide at least a first order analysis of gear noise. Such an idealization was used by Hersh et al., (1976) in a component scheme to predict noise level; in this case, each landing gear bogie was replaced with either a vertical or horizontal cylinder. The authors suggest that the scheme did well at predicting Overall Sound Pressure Level (OASPL), but as a consequence of the idealization, allows consideration of only the bluff body wake mechanism. Such an idealization also prevents the prediction of source directivity and frequency content, among other important noise field parameters.

Since our goal is not merely to determine noise level, we must consider a more rigorous approach to landing gear noise prediction. Such an approach must go beyond the above idealization and include at least fundamental geometric components such as wheels, axles and support struts. By including these components we will be able to consider the turbulent inflow noise production mechanism and the three-dimensional aspects of the developed flow field.

Heller and Dobrzynski (Heller and Dobrzynski, 1977a; Heller and Dobrzynski, 1977b) demonstrate the importance of turbulent inflow and three-dimensional wake to noise generated by landing gear with in-line wheel sets in two consecutive studies. In the first, the sound radiated from two- and four-wheel landing gear configurations was investigated. Models included the wheel well, support struts, axles and wheels and were exposed to flow from a wall-jet. The authors conclude that the likely dominant noise source for the four-wheel bogie is "the interaction of the wake from the forward wheel set with the rearward wheel set."

In the follow up study, the authors utilized a model of a four-wheel bogie attached to the undersurface of the wing of an aerodynamically clean glider. The model was instrumented with fluctuating pressure transducers on a fore and an aft wheel. The results indicated that the strongest unsteady flow occurred in the region aft of the forward wheel-set and over the entire rear wheel-set. Using a potential flow calculation (Fig 1.2), along with the experimental results, the authors conclude that the significant pressure fluctuations on the rear of the fore wheel and the front of the aft wheel are due to flow separation and wake impingement respectively.

Preisser (1980) provides further evidence of the importance of turbulent inflow, especially for an in-line wheel geometry, in a study of airframe noise from a supersonic transport. Radiated noise levels were measured from various components of a .015 scale model operated in an anechoic open jet facility. The findings show that each main landing gear bogie, consisting of six rows of two-wheel in-line sets, contributed significantly to airframe noise while the nose landing gear bogie, consisting of a single two-wheel set, contributed negligibly. Although the mechanisms responsible for the high level of main gear noise were not investigated, it seems clear that the wake from the fore wheels impinging on the aft wheels had a significant effect.

In light of the above discussion, for accurate noise prediction, both noise production mechanisms of wake flow and turbulent inflow must be considered for landing gear configurations. In order to include both mechanisms, we must use a component prediction scheme and model at least the basic geometric components of the landing gear system. The component scheme of choice is the distributed-source analysis method described by Hayden et al. (1975). It comes closest to incorporating the actual physical noise source mechanisms and provides the important noise field parameters of level, source directivity, and frequency content. But, as Harden et al., (1975) state, "All predictions of radiated noise (using the distributed-source method) are intimately related to the details of the local flow fields." Therefore, in order to use such a scheme the flow physics associated with the noise must be well understood.

1.2.2 Noise Abatement Considerations

Due to geometric complexities, and thereby a lack of understanding of the underlying flow physics, very little effort has been given to reduction of noise generated by landing gear. In the only recorded attempt to reduce noise, Dobrzynski and Buchholz (1997) conducted an experiment using a full-scale operational 4-wheel landing gear from an A320 Airbus aircraft. Tests were conducted in the German Dutch Wind Tunnel (DNW) over a Reynolds number range characteristic of practical approach flight conditions. Acoustic data were acquired using a microphone array to determine noise spectra and radiation directivity. Leg and brake fairings were added to determine the effect of streamlining some of the less aerodynamic components, but no attempt was made to inhibit flow interaction between the in-line wheels (Fig 1.3). Results showed that adding the fairings reduced noise by only about 3 EPNdB[1]. The authors suggest that the limited noise reduction potential of the fairings is due to "tire-wake/tire interaction noise." Such speculation comes from the source location results, which identified the region between the fore and aft wheels as one of significant noise production, whether or not the fairings were installed.

Any suggested techniques for noise reduction must not only be effective in their implementation, but acceptable to aircraft manufacturers. Acceptable noise reduction techniques should follow guidelines such as ease of implementation and maintenance, limited weight differential, and low cost. These guidelines lessen the value of techniques such as that mentioned above. In order to develop effective noise reduction techniques that meet guidelines of acceptability, it is first important to know details of the associated noise production mechanisms. For landing gear, the above study suggests that specifics of the flow field around the wheels are particularly important.

1.3 Current Objectives

The above discussion portrays the current state of understanding of landing gear noise and its sources. Thus far, most of the work conducted in this area has concentrated on noise prediction capabilities. Very little work has addressed the flow physics that produces the noise or methods of reducing it.

While noise production is inherently dependent on the fluctuating characteristics of the flow, insight can be gained into the origin of noise through an understanding of the mean flow features. Surface mean flow characteristics can identify likely regions of high noise production such as flow separation and reattachment locations. Surrounding mean velocity and vorticity fields can identify mean flow structure and even mean flow states that may be responsible for significant noise production. With these flow features identified, predictive capabilities are enhanced and abatement techniques can be developed more readily.

---

[1] EPNdB are the units of Effective Perceived Noise Level (EPNL).

The current investigation aims to provide an understanding of the mean flow physics around a 4-wheel landing gear bogie. In order to accomplish this, the current research objectives are to:

(i) Determine the qualitative mean velocity field around a four-wheel bogie. While Heller & Dobrzynski (1977b) present what appears to be a calculation of the mean flow field around a four-wheel bogie, there is no known experimental evidence to support it.

(ii) Determine the surface flow features on both the fore and aft wheels using surface oil flow visualization. The topological patterns will help identify regions of flow separation and reattachment and can be used to infer flow features off the surface.

(iii) Determine the mean surface pressure signature around the entire periphery of the fore and aft wheels. This information will complement evaluation of the surface streamline patterns and identify regions of flow impingement.

(iv) Determine the mean velocity and vorticity fields in a plane bisecting the in-line wheels using Digital Particle Image Velocimetry (DPIV). This data will also help to identify any mean flow state changes between the wheels.

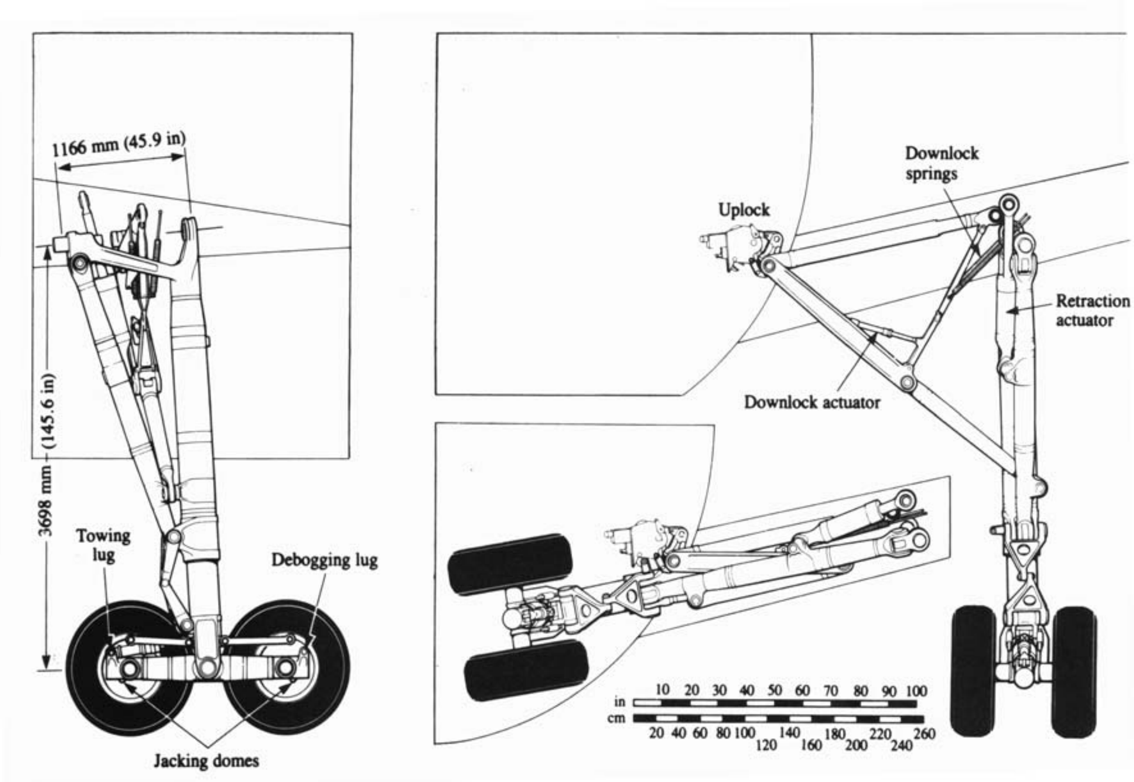

Figure 1.1 Example schematic of a 4-wheel landing gear bogie for an A310 Airbus aircraft.

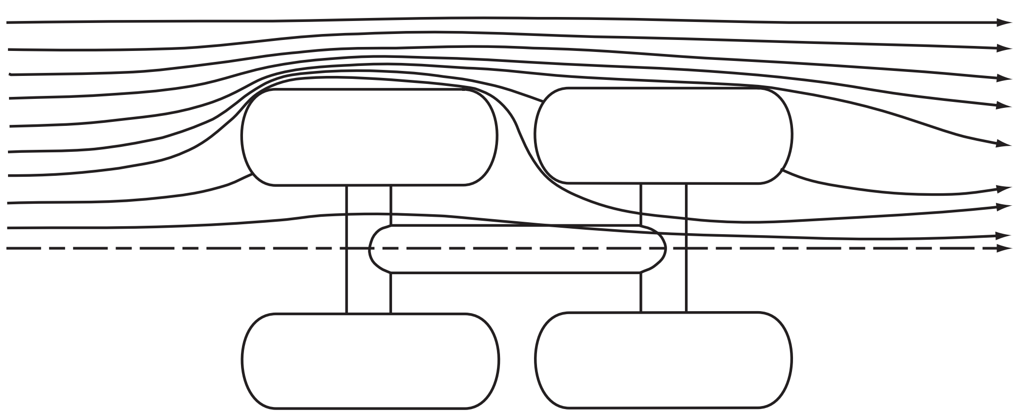

Figure 1.2 Mean flow representation around 4-wheel bogie from Heller & Dobrzynski (1977b).

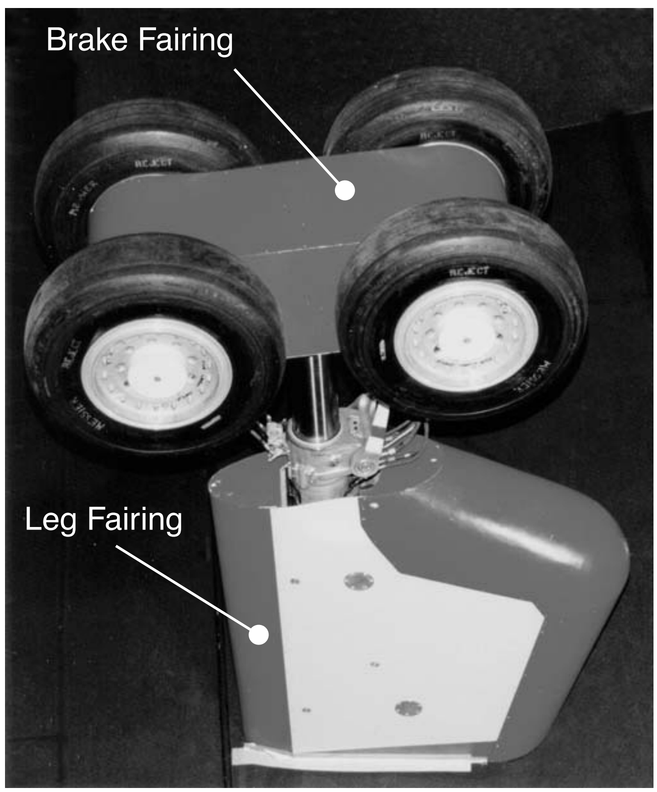

Figure 1.3 Streamlined fairings applied to 4-wheel landing gear bogie from Dobrzynski and Buchholz (1997).

2 Experimental Facilities and Techniques

Two different facilities were used for the present study. The first was a water channel where low Reynolds number qualitative flow visualization experiments were conducted. The second was a wind tunnel known as the Basic Aerodynamics Research Tunnel (BART), which allowed qualitative as well as quantitative experiments were conducted at a range of higher Reynolds numbers. Both facilities are located at the NASA Langley Research Center in Hampton, Virginia.

Two different models were constructed, one for each facility. Each was configured to represent a simplified version of a Boeing 757 main landing gear (fig 2.1). This particular landing gear was chosen because it is a 4-wheel configuration and was readily available for detailed inspection.

2.1 *Water Channel and Model*

The water channel used for the present study is a closed circuit facility with a test section area of 33- x 30.5-centimeters and a length of 244 centimeters. Optical accessibility into the test section is provided on all four sides. For the current tests, the water level was maintained at 33 centimeters. Flow straighteners are positioned ahead of the contraction to reduce turbulence levels. Water was pumped at a continuous rate of 11.35×10^{-3} m^3/s to maintain a constant test section speed of 11.4 cm/s. Figure 2.2 is an oblique diagram of the facility with the model installed.

The model was constructed using an aluminum cylindrical support structure with molded Plexiglas wheels (fig 2.3). The wheel diameter was 13.2 centimeters, thereby making it a 13% scale model with a Reynolds number of Re_d = 15,000. The model was inserted into the open channel in an upright position and supported from the top. Blockage, calculated as the ratio of model frontal area to test section cross-sectional area, was about 20%. One of the model wheels was outfitted with five dye ports along the tread area and was subjected to controlled rotation using a servo motor installed in the axle. Figure 2.4 shows a cut-away section of the wheel with the dye ports and motor highlighted. Dye visualization and particle trace studies were conducted in the water channel with this model. Since the water channel is open and the model support strut passed through the waters surface, a 1.6 mm thick Plexiglas sheet with a cutout for the model support was laid on the surface of the water behind the model during testing to reduce surface disturbances.

During dye visualization tests, the ported wheel was rotated to test sites every 10 degrees and held stationary. Dye, consisting of a 70/30 mixture of water and food coloring, was injected at each test site location from zero to 350 degrees and videotaped from various angles as it traveled downstream. Dye was injected from both a fore and an aft wheel simply by rotating the model 180 degrees to position the ported-wheel in the front or rear.

Particle trace studies were conducted by adding silver coated glass spheres to the water. These spheres had a nominal diameter of 14 microns. A light sheet was created by scanning the beam of a Coherent Innova 90 argon ion laser with a maximum power setting of two watts. The scanning device was a simple in house construction of an oscillating mirror operating at a frequency high enough to image the particles as a continuous line. The sheet was oriented in the streamwise direction either horizontally or vertically to illuminate two different planes of flow around the model. In the horizontal position the light sheet passed through the plane described by the wheel centerlines while in the vertical position the lightsheet bisected the wheels (fig 2.3). Video and still images were recorded of particles passing through the sheet. Exposure time was adjusted to image the particles as lines in order to highlight their paths.

2.2 Wind Tunnel and Model

The Basic Aerodynamics Research Tunnel (BART) is an open circuit wind tunnel with a test section area of 71- x 102-centimeters and a length of 305 centimeters. The interior of the test section is optically accessible from all sides except the floor. An orthogonal motion traversing rig surrounds the test section and has a location readout accuracy of 10 microns in the x and y directions and 1 micron in the z direction. The useable speed range of the tunnel is between approximately 20 and 56 m/s. A schematic diagram of the facility with the traversing rig in place is shown in figure 2.5.

The model was constructed similarly to the previous model. A dimensioned schematic is shown in figure 2.6. Steel was used for the cylindrical support structure and molded Plexiglas for the wheels. It was installed in the tunnel upside-down since the supporting apparatus for the facility was under the test section floor. The model wheel diameter was 30.5 centimeters making it a 31% scale model with a tunnel blockage of about 14%. Testing was conducted at four different tunnel speeds to provide Reynolds numbers of 0.4, 0.6, 0.8, and 1.2 million. One of the wheels was outfitted with 50 pressure taps along its periphery and made rotatable using a servo motor installed in the axle. Figure 2.7 shows a cut-away sketch of the wheel with the motor and pressure taps highlighted. Tests performed using this model included oil flow visualization, measurement of mean static pressures, and PIV measurements.

2.2.1 Oil Flow Visualization

Oil flow visualization was conducted to determine the surface streamline patterns on the fore and aft wheels at the four Reynolds numbers mentioned in the foregoing. One of the model wheels was marked at precise locations with fiduciary points and all oil flow experiments were conducted using this wheel by placing it either on the front or rear of the model. The fiduciary points were used to provide accurate mapping of the acquired two-dimensional oil flow images onto a three-dimensional computer representation of the model. A picture of the model in the tunnel with a fiduciary point highlighted is shown in figure 2.8.

Oil flow studies were conducted by brushing a mixture of Kerosene and Titanium Dioxide powder onto the wheel with the tunnel flow off. Immediately after application of the mixture, the test section was closed and the tunnel was rapidly brought up to speed. A constant speed was then maintained until the oil mixture had sufficiently dried.

An image of the outboard side of the wheel was acquired with the wheel in place in the tunnel. Oil was then removed from the outside of the wheel and, after loosening an anchor screw, the wheel was extracted from the tunnel using a large suction cup. The wheel was then placed in a specially prepared booth where six images were acquired around the wheel tread area by rotating the wheel every 60 degrees. A final image was acquired of the inboard side of the wheel. Image acquisition was accomplished using a Kodak DCS 460 digital camera with an image resolution of 3060 x 2036 pixels. The photographic booth was constructed using a white bedding sheet hung in a cylindrical fashion from the ceiling and was used to provide diffuse lighting to eliminate glare and reflections.

2.2.2 Static Pressure Measurement

Mean static pressures were acquired on the ported wheel surface using a Pressure Systems Inc. ESP8400 pressure acquisition system. Pressures were acquired around the entire wheel circumference at measurement stations every 2 degrees by rotating the wheel via the servomotor. Positioning accuracy using the servo motor was determined to be approximately plus or minus 0.3 degree. At each measurement station, 30,000 data samples were acquired simultaneously at each of the 50 ports over a 90 second period. The samples acquired at each port were then averaged to produce the mean. Surface static pressures were measured on both a fore and an aft wheel by simply rotating the model 180 degrees to position the ported-wheel in the front or rear. Tunnel static and total pressures were also acquired at each measurement station so that dimensionless pressure coefficients could be determined. All acquired data were differentially referenced to atmospheric pressure.

To maintain accuracy of the measurements, the pressure acquisition system was calibrated before each data run, where a data run consisted of pressure acquisition over either the top or bottom half of the wheel. Since many of the components of the system were located in the test area, the ambient temperature there was closely monitored. If test area temperature varied by more than 1 degrees Celsius, the system was again calibrated before continuing data acquisition. This ensured that variation in component accuracy due to temperature was reduced.

For each ported-wheel position, front or rear, tunnel speed was adjusted and maintained to achieve the previously mentioned Reynolds numbers of 0.4, 0.6, 0.8, and 1.2 million. Mean pressures were acquired at each Reynolds number using a differential pressure transducer rated at either 10 inches of water or 1 psi. Cursory measurements were acquired around the wheel to determine the maximum pressure for each combination of Reynolds number and ported-wheel position. The Transducer range was chosen so that most of the available scale could be used without exceeding the limits, thereby providing the greatest accuracy. At least two data sets, consisting of the mean pressure at each static port around the entire wheel, were averaged together to produce final a data set of mean static pressure for each test condition.

2.2.3 DPIV Measurement Details

Digital Particle Image Velocimetry (DPIV) was used to determine the velocity field in a vertical plane bisecting the wheels. This plane had the same positioning as the vertical light sheet plane used in the water channel studies shown in figure 2.3. In general, DPIV is a technique that uses two digital images of a particle field taken at some small time difference, Δt, to determine velocity vectors at discrete locations in the image plane. Illumination of the particle field is accomplished using a laser light sheet, the thickness of which defines the depth of the image plane. Consideration must be given to particle size and density, since it is important that particles properly follow the flow and are numerous enough within the image plane to obtain accurate results. A comprehensive review of PIV is given by Adrian (1991), and the unique characteristics of DPIV are addressed by Willert and Gharib (1991).

The vertical data plane acquired in the current study extended in the streamwise direction from $x = -50$ to 658 mm and in the cross-stream direction from $z = -194$ to 194 mm. It consisted of 160 side-by-side image planes measuring 36- x 36-mm, each overlapping its neighbors by 4 mm. The size of the image planes was made small to provide the spatial resolution necessary for future analysis, beyond the scope of the current work. Figure 2.9 shows the position of each image plane relative to the coordinate axes located at the center of the fore wheel.

Seeding of the flow was accomplished using four TSI model 9306 6-jet atomizers. The seed material was Swan™ mineral oil, a common drugstore item, which, when atomized, produces a median particle size of about 0.7 micron. Since the BART facility is an open circuit tunnel, the entire room enclosing it was filled with particles. This ensured the flow was sufficiently seeded at all data locations, providing an even distribution of particles throughout the tunnel test section.

Particle images were acquired using a Kodak ES 1.0 digital camera with a pixel resolution of 1018 by 1008. One hundred image pairs were acquired at each data location in groups of 50 at a rate of 5 Hz. Two Spectra-Physics Quanta Ray GCR-3 Nd:Yag lasers illuminated the particle field with 500 mJ of energy per pulse at a 532 nm wavelength. Light sheet thickness was adjusted from between 1 to 2 mm, with the wider value approached to reduce error due to out-of-plane motion. Timing of the laser firing and image acquisition were accomplished through electronic circuitry that coupled the two together. The delay time, Δt, between acquisition of a pair of images ranged from 2 to 9 microseconds and was adjusted toward the smaller value, again, to reduce error due to out-of-plane motion. Figure 2.10 is a schematic diagram of the timing and recording equipment components and connections. Figure 2.11 shows the setup for the PIV system and the placement of the laser light sheet for acquisition of data above the wheels. Data acquisition below the wheels was accomplished by adjusting the light sheet optics to pass it through a Starfire™ glass window installed in the floor under the wheels.

2.2.4 DPIV Interrogation

Interrogation of particle image pairs was performed to determine the velocity vectors associated with the displacement of particles from image one to image two. Critical parameters used in DPIV interrogation are image magnification and the time delay between acquisition of the first and second image in a pair, Δt. Image magnification was determined by adjusting the camera lens so that it precisely imaged the width of a square measuring 36- x 36-mm. With the exact width of the CCD array known, the ratio of the image width to the CCD array width yielded a magnification of four. Accurate measurement of Δt was accomplished using photo sensors to detect the firing of each laser and an electronic counter to determine time between firings to the nanosecond.

The interrogation technique correlated image pairs to provide the three most likely vectors at a given interrogation spot. Each interrogation spot measured 64 by 64 pixels and overlapped its neighbors by 16 pixels. The three most significant correlation peaks were identified with each peak located to sub pixel accuracy within the interrogation spot, using a Gaussian fit. The location of each peak then prescribed the magnitude and direction of a vector originating at the center of the spot. Analysis of this sort over the entire image area yielded a 60 by 60 vector array with a spatial resolution of about 1 mm.

To determine which of the three vectors resulting from the cross correlation was the most appropriate, a routine called Cleanvec (Meinhart et al., 1994) was used. This routine takes the three vectors and displays them as either black, red, or green depending on the magnitude of the corresponding correlation peak. Black represented the most likely choice, red the second most likely choice, and green the third mostly likely choice. The routine can be run either manually or in automated mode. In the manual mode, the user views each vector array and selects the most appropriate vectors by hand. In the automated mode, the user selects global and local statistical criteria for determining the validity of a vector choice. The strategy of the automated mode consists of: (1) removing all, or as many as possible, of the bad vectors, then (2) replacing the bad vectors with alternative vectors, based upon statistical information about the remaining good vectors. Cleaning the set of 100 images at each image plane was performed using the automated mode with statistical criteria chosen from a manual analysis of 10% of the images.

Figure 2.1 Boeing 757 main landing gear.

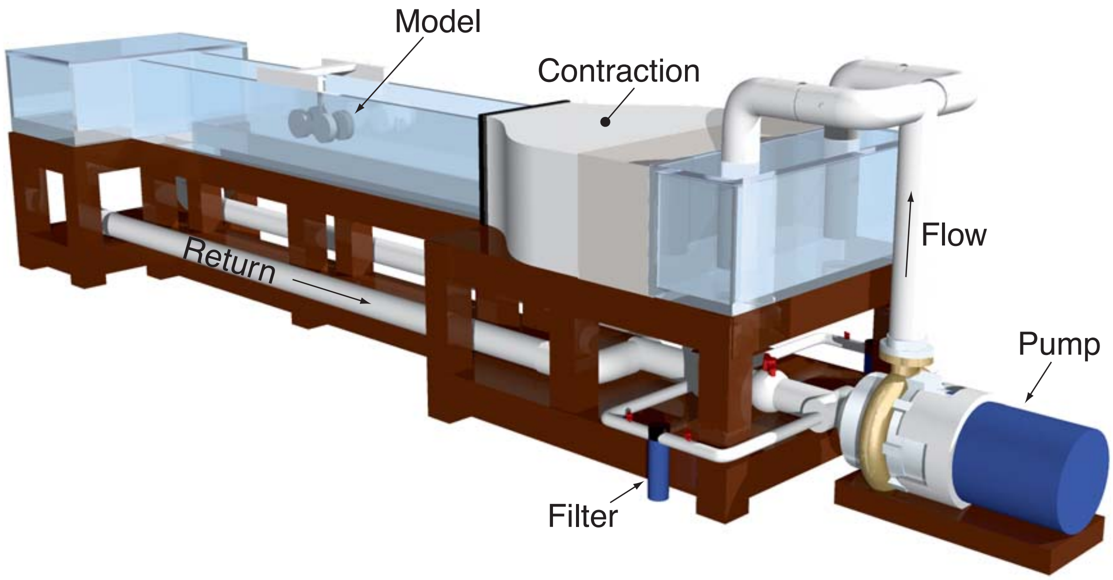

Figure 2.2 15- x 12-inch water channel facility.

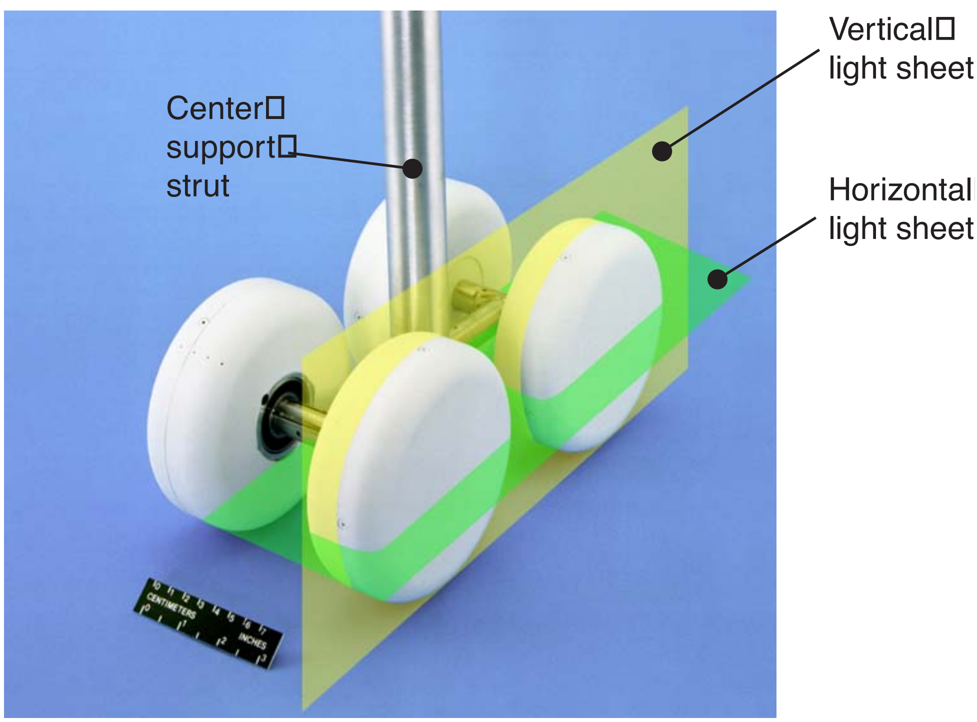

Figure 2.3 Thirteen percent scale model of Boeing 757 landing gear used in water channel studies. Light sheet positions are highlighted.

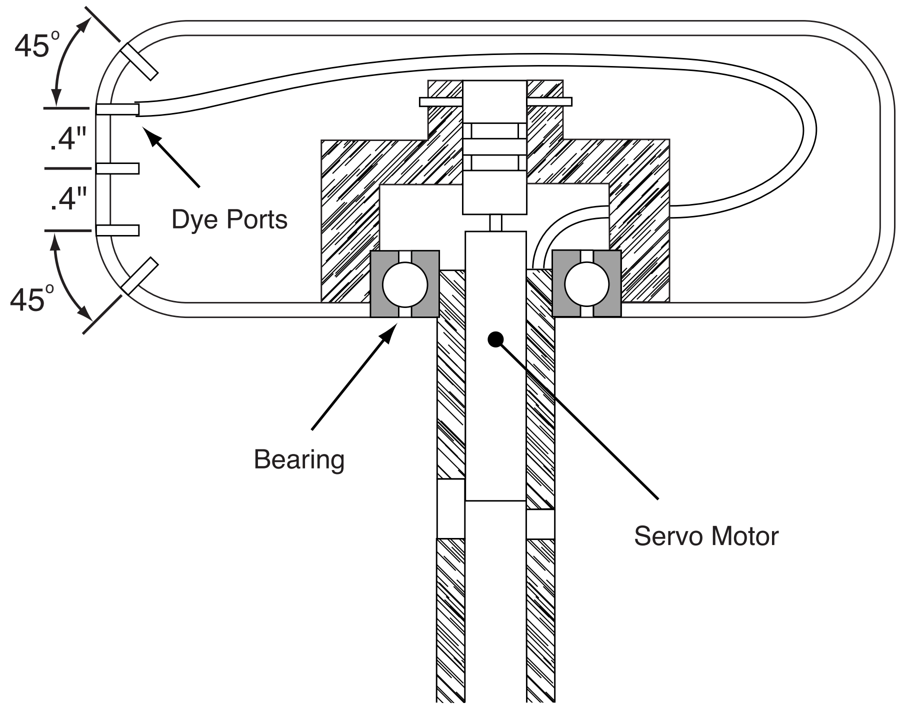

Figure 2.4 Cut away section of dye ported wheel on model used in water channel studies.

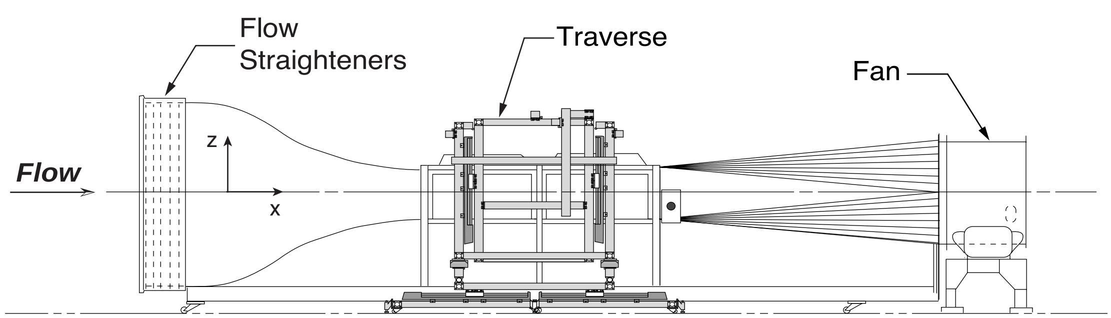

Figure 2.5 Schematic diagram of Basic Aerodynamics Research Tunnel (BART).

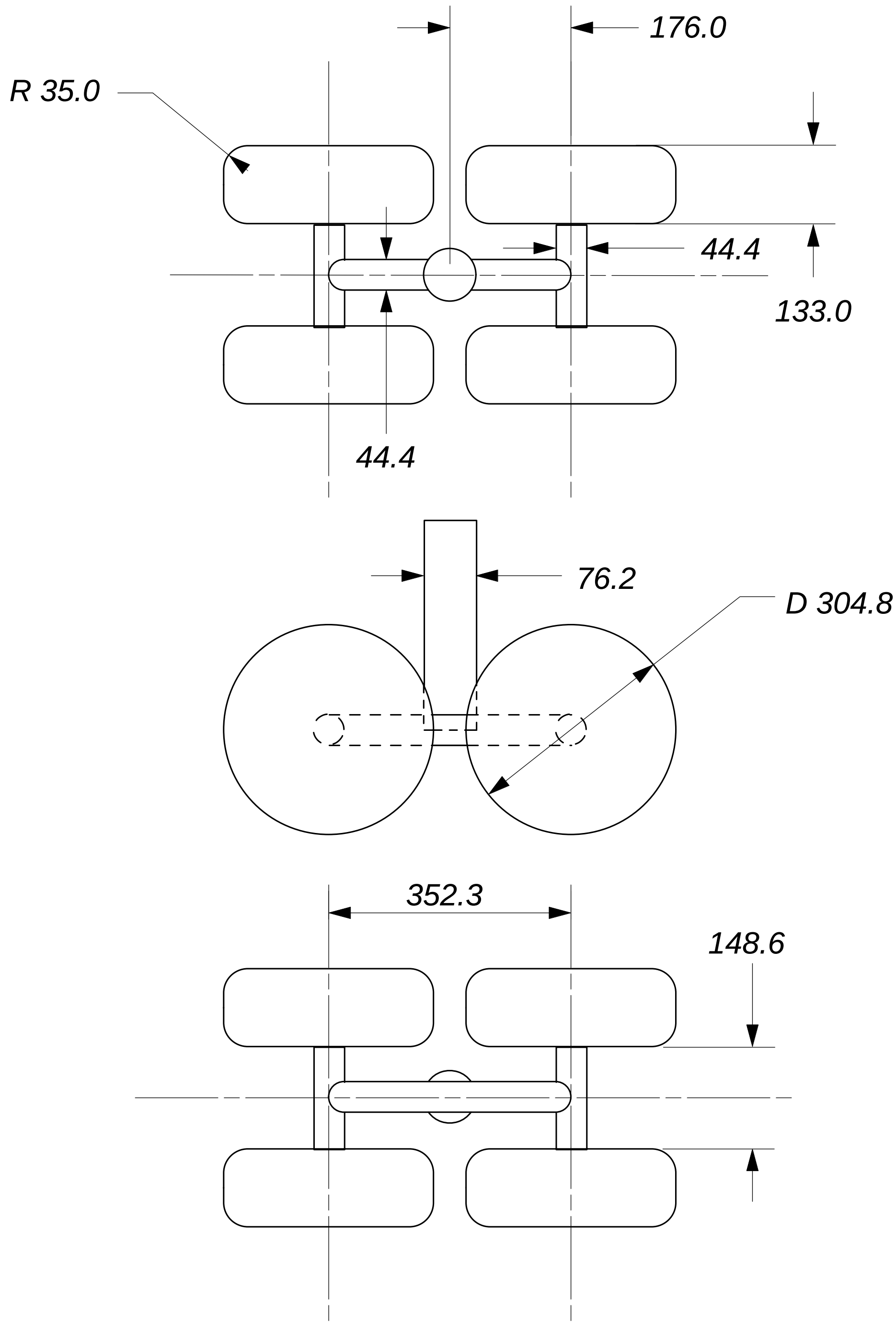

Figure 2.6 Dimensioned schematic of wind tunnel model. (Dimensions in millimeters.)

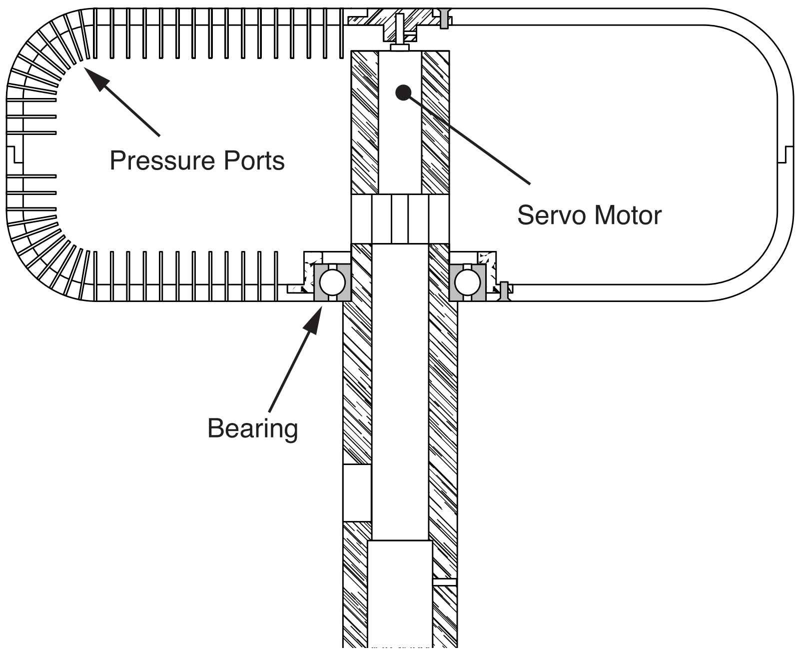

Figure 2.7 Cut away section of pressure ported wheel on model used in wind tunnel studies.

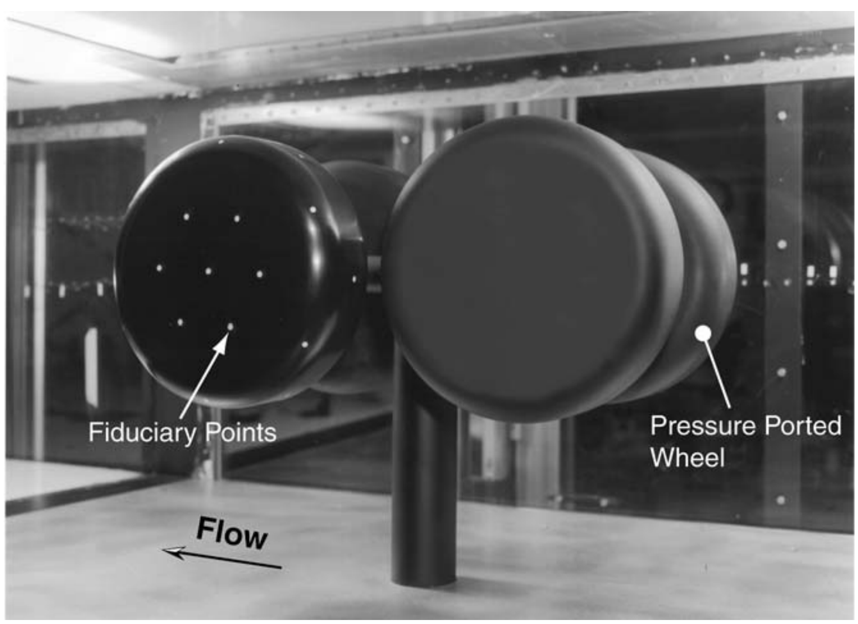

Figure 2.8 Model installed upside-down in BART Facility.

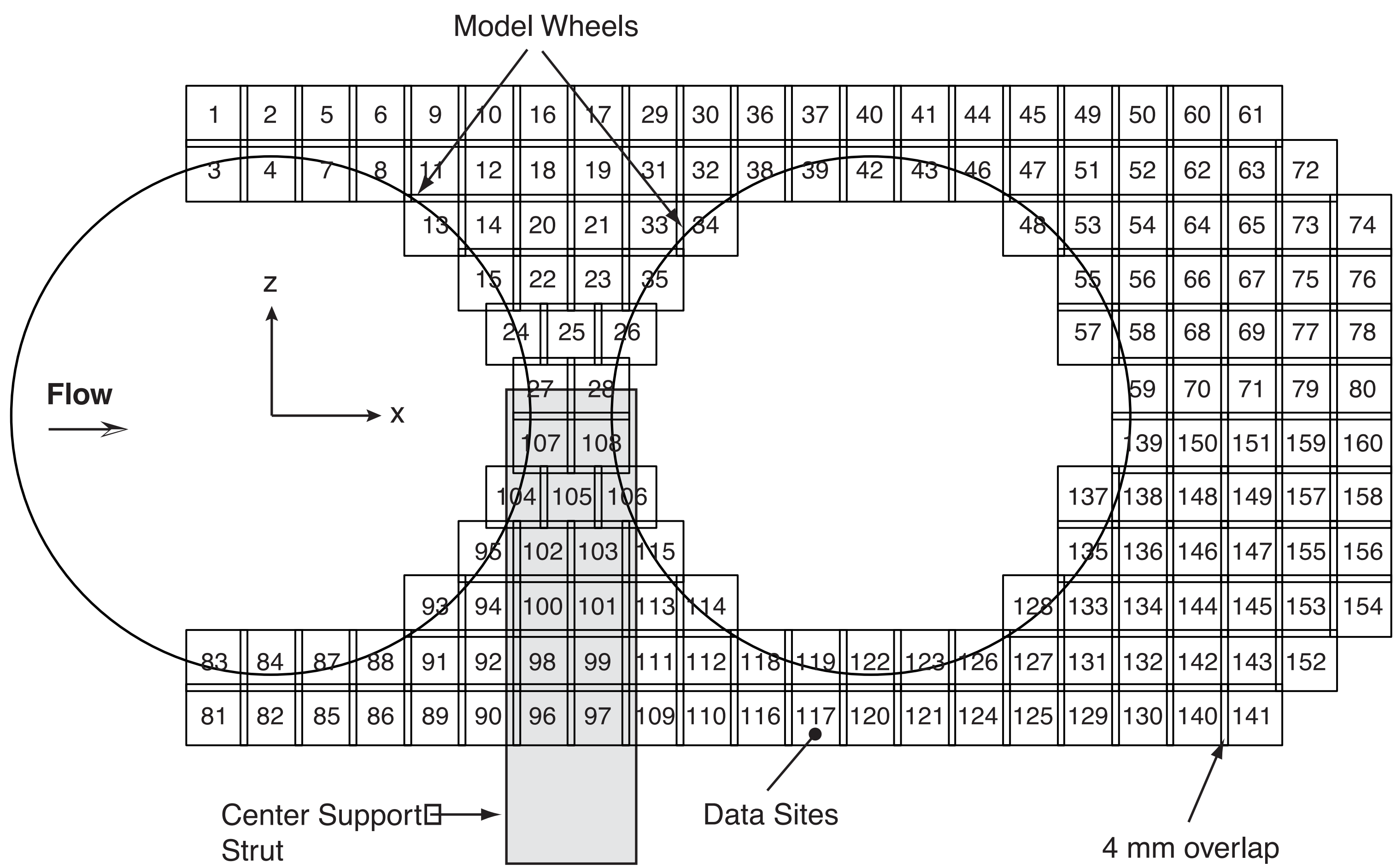

Fig 2.9 DPIV data locations around the model wheels.

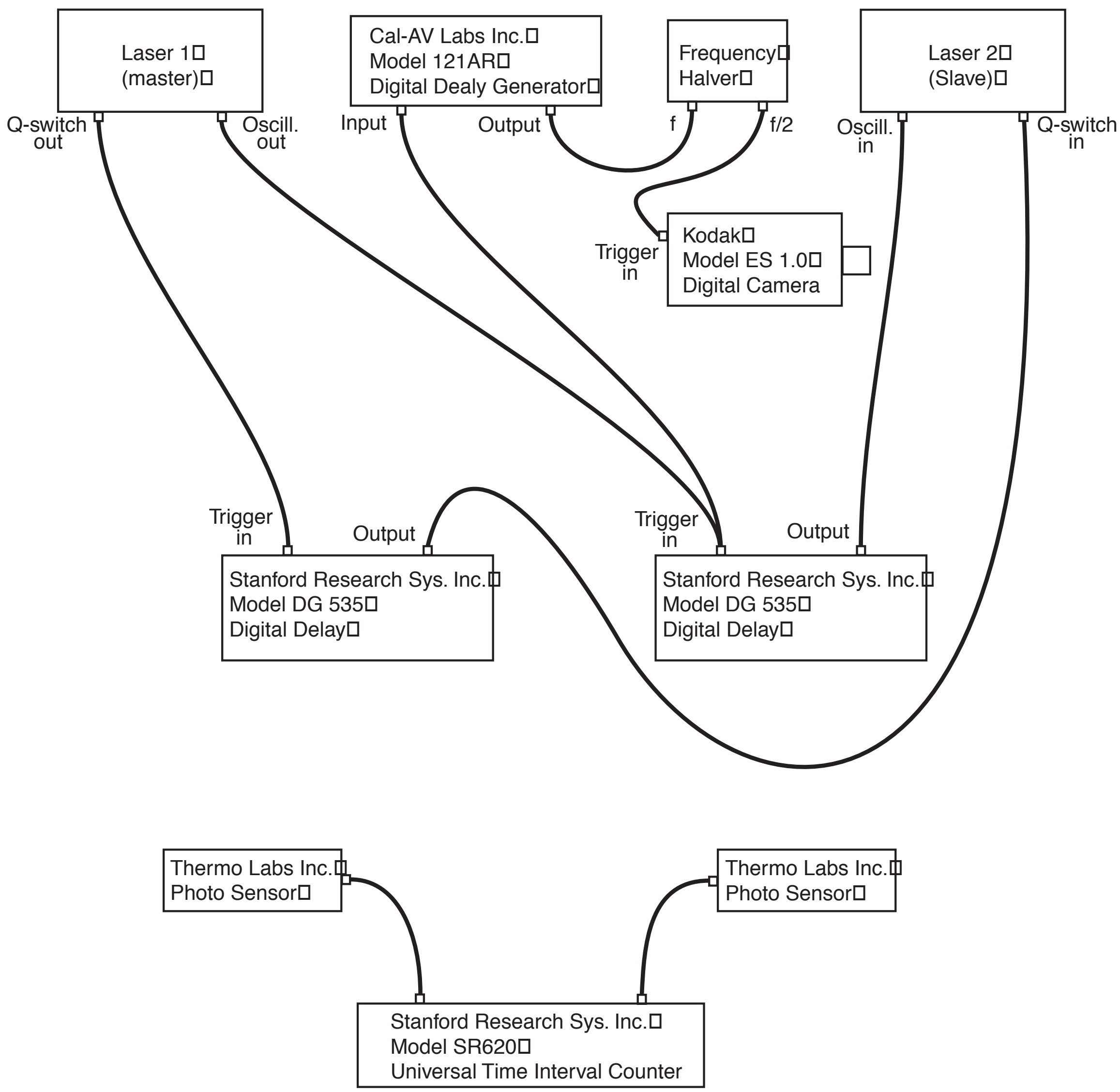

Figure 2.10 Schematic of test equipment components and connections.

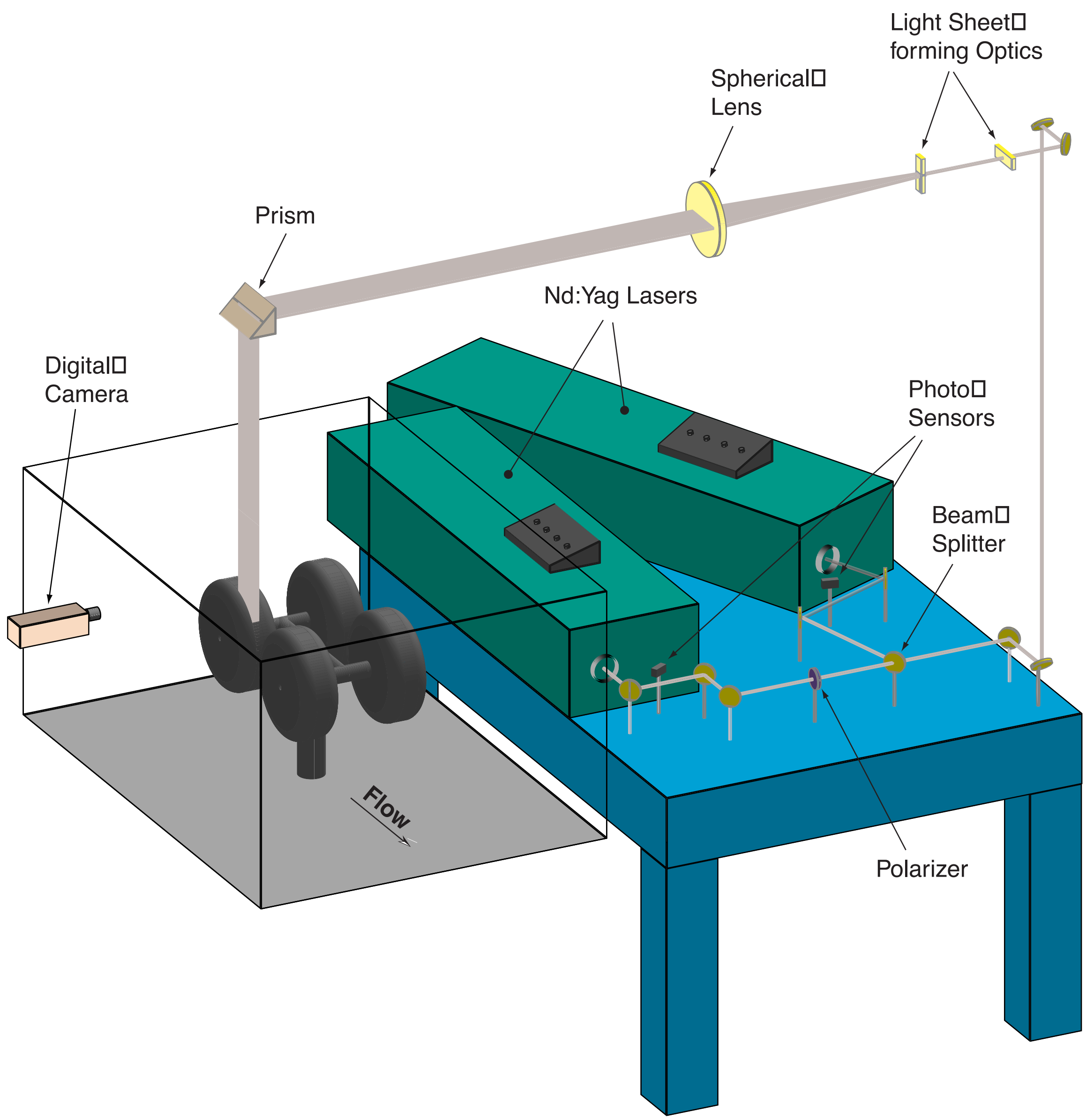

Figure 2.11 PIV equipment setup.

3 Qualitative Characteristics of Mean Flow

The mean flow field around a four-wheel landing gear has never been determined experimentally. In view of the complexity of this configuration, and therefore the corresponding flow patterns, a qualitative overview is highly desirable as a prelude to quantitative measurements. The initial phase of this investigation consisted of qualitative visualization of the mean flow around a simplified model of a Boeing 757 landing gear installed in a water channel. The techniques, as described in section 2.1, included dye injection and particle tracing. While the Reynolds number for these studies is relatively low, $Re_d = 15{,}000$, it is expected the results will provide a general account of the flow field beyond Reynolds number dependence, and will provide useful information to guide the more rigorous investigation of the flow field described later in this work.

3.1 Dye Visualization

Dye released at each of the ten degree sites reveals streaklines near the surface of the model originating at each of the dye ports. At locations on the wheel where the boundary layer is laminar, the dye lines remain smooth and intact. But as soon as any turbulence or a region of separation is encountered the lines become very erratic, tending to break up into fragments. While this makes observations within a turbulent region difficult, the ability to identify where turbulent and separated regions exist is, in itself, valuable.

In order to present the dye visualization results in a coherent fashion, the data videos were reviewed and two dimensional renderings of the results were constructed in three views for each wheel. Rendering began by first marking the display monitor with an indelible pen to identify dye port locations for each test site. With these specific locations highlighted, the paths of the streaklines were readily determined. Several views of the dye injection process were used in the rendering procedure and overlapping regions were compared to reduce error.

3.1.1 Fore Wheel

Shown in figure 3.1 is a rendering of the front surface of the fore wheel with the dye streaklines identified in red, green and blue. Coloring of the dye lines serves only to identify their origin; red lines originate from ports along the wheel centerline, green lines originate from ports on either side of the centerline, and blue lines originate from ports on the outside edges of the wheel tread area. The numerical values along the face of the wheel identify the rotation angle of each test site. Positive wheel rotation is in the counterclockwise direction when viewed from the outboard side.

The results indicate that the incoming flow stagnates at a point just to the wing-side of the horizontal centerline and inboard of the vertical centerline, at a location between the green and red dye ports. The offset in the horizontal direction is associated with a pressure difference between the inboard and outboard sides of the wheel. The flow obstruction created by the axle slows the incoming fluid, creating a lateral pressure gradient across the face of the wheel. Flow emanates from the stagnation point in all directions and forms of a three dimensional pattern. Note that the flow lines are very symmetric on either side of the horizontal centerline, indicating that the center support strut does not significantly affect the flow over this portion of the wheel. The figure also shows that most of the flow across the wheel surface between ± 30 degrees is deflected either to the inboard or outboard side, under the influence of regions of lower pressure on those sides.

Looking at the wing-side[1] of the fore wheel, figure 3.2 shows the observed streakline features. Here the magenta line represents dye injected with the ports at a zero degree rotation angle. The dashed lines represent broken or fragmented dye lines. In reality these are not coherent lines at all but are meant to highlight the path the dye travels after streakline breakup occurs. As the dye is injected from the front of the wheel, a portion of it travels over the outboard edge until it reaches the end of wheel curvature. Here it separates from the wheel surface, traveling downstream intact, as a line. Eventually this dye line marks vortices that are shed from the edge of the wheel. These vortices increase in scale as they convect downstream. The dye marker then breaks up and diffuses into a localized region between the outboard surface of the wheel and the fragmented dye line depicted in the figure. The fluid within this region becomes increasingly turbulent as it travels downstream till it reaches the wheel edge, where the majority of it is entrained between the fore and aft wheel and drawn across the forward face of the aft wheel. On the inboard side of the fore wheel the same sort of circumstances prevail; however, the vortical roll-ups

[1] The side of the model from which the support strut extends will be referred to as the wing-side of the model; the opposite side will be referred to as the ground-side.

appear to be more stationary and somewhat smaller in diameter. These are hypothesized to comprise the system of vortices developed ahead of a cylinder upon separation in a laminar junction flow (Seal et al, 1995; Coon & Tobak, 1995; Visbal, 1991).

Higher pressure occurs on the inboard side of the wheel as a result of the flow obstruction created by the axles and center support strut. This is evident in figure 3.2 as all streaklines originating from the wheel centerline outboard, tend toward the outboard side of the wheel where the pressure is lower. Even those streaklines originating interior to the center line abruptly change course from an inboard to an outboard direction as they travel downstream. Laminar flow separation occurs in a horseshoe like pattern across the wing-side face of the wheel, as indicated by the yellow line in the figure. It begins near the lateral center of the wheel at about -104 degrees and extends down both sides to about -130 degrees. After separation, the dye lines fragment with some of the dye recirculating underneath the separated flow, back to the line of separation. Most of the fragmented dye, however, separates completely from the wheel and is drawn ground-ward between the fore and aft wheels.

Figure 3.3 shows that the streaklines on the ground-side of the fore wheel make a similar pattern to that on the wing-side, shown in the previous figure. The most significant difference between the two sides is the location and shape of the line of separation. On the ground-side, separation occurs significantly further upstream. It begins at about 86 degrees and extends down the inboard side only, to about 100 degrees. The likely explanation for the difference is the effect of the center support strut, which is the only asymmetry in the model.

3.1.2 Aft Wheel

As previously mentioned, dye studies on the aft wheel were conducted by merely rotating the model 180 degrees about the center support strut to position the ported wheel in the rear. This rotation also placed the ported wheel on the opposite side of the model, relative to that reported in Section 3.1.1. Symmetry conditions about the vertical centerline suggest, however, that such a repositioning will produce no significant effects. Positioning of the dye ports at the various test sites was again achieved by rotating the wheel. Rotation in the counterclockwise direction is defined as positive.

Shown in figure 3.4 is a rendering of the dye streakline formation on the forward face of the aft wheel. Over the azimuthal range of -60 to 60 degrees, the dye lines were never completely stable. This observation suggests that the entire forward face is subjected to incident turbulence; some places more so than others. On the wing-side of the wheel, the dye lines remained steady for the most part, with only infrequent oscillations. Therefore they are drawn as solid lines in the figure. On the ground side, from about 10 to 60 degrees, the dye lines broke up rapidly, indicating the flow was significantly turbulent. Note that several of the dye ports in this region have two lines extending from them. This represents the observation that dye lines originating from these points alternated between two mean trajectories. From the streakline characteristics, it is possible to deduce a line of attachment. This line is assumed to follow the cyan arc drawn in the figure. The dye lines tend to diverge from this arc. The blue lines in contact with the arc were noted to alternate between two mean trajectories, as indicated in the figure.

Observations of the wing-side of the aft wheel are depicted in figure 3.5. The magenta lines again represent dye injected from the ports while at zero degree rotation. For the most part, the dye diffused rapidly after injection from these ports, so the dye lines are drawn as fragmented. This figure shows how the marked fluid becomes more turbulent as it travels across the forward face to the inboard side of the aft wheel. At the edge of the wheel, the flow separates, increasing the level of turbulence. This turbulent fluid then travels downstream and impacts the rear axle. In the region between -30 and -90 degrees, the dye lines remain relatively intact experiencing only occasional oscillations. The yellow line in the figure marks the separation location at about -90 degrees. This rather shallow angle suggests laminar separation, as expected, since limited turbulent activity was observed in this region.

On the ground-side of the wheel, represented in figure 3.6, the dye lines were all very erratic and broke up rapidly. This portion of the wheel is obviously in the wake of the fore wheel. A distinct line of separation was not apparent on this wheel, but the occasional upstream flow of the blue dye lines indicated unsteady flow separation along the inboard and outboard edges of the wheel between 120 and 130 degrees. The red and green lines on the interior portion of the wheel showed no signs of separation.

3.2 Particle Path Study

Particle path studies were also conducted in the water channel by adding silver coated glass micro-spheres to the water. Specifics of this procedure are outlined in section 2.1. Video and time lapsed imagery of the particles in a laser light sheet provide instantaneous images of streamlines. Studies were conducted with the light sheet in both a streamwise-vertical and horizontal plane. In the following discussion, the angular origin of each wheel is its leading edge and positive angles are counterclockwise.

To view the flow around the wheels in a streamwise-vertical plane bisecting the in-line wheels, several images were acquired with the light sheet introduced through the top and the bottom of the test section. The obstruction of the model support above the model made it necessary to project the light sheet at two different streamwise angles in order to illuminate, from the wing-side, the entire region between the fore and aft wheels. These two images are shown in figures 3.7 and 3.8. In the first image, the light sheet is projected at an angle in the downstream direction. In the second, the light sheet is projected at an angle in the upstream direction.

Figure 3.7 clearly shows separation on the wing-side of the fore wheel at about $-10($ degrees. From there, the wake of the fore wheel is drawn in the ground-ward direction in front of the aft wheel, while the region above is basically potential flow. The separation of these two flow regions occurs at the stagnation point, highlighted in figure 3.8, on the front of the aft wheel between $-3C$ and $-4C$

degrees. This accounts for the infrequent turbulent activity observed on the forward face of the aft wheel beyond -40 degrees in the dye visualization studies. The figure also shows flow separation on the wing-side of the aft wheel at about -90 degrees, where the roll up of longitudinal vortices is readily apparent.

For the case where the light sheet is projected from underneath the test section, figure 3.9 shows the flow characteristics on the ground-side of the model and in between the wheels. Flow separation from the ground-side of the fore wheel is highlighted in the figure at about 90 degrees. Following separation, the wake travels downstream and mixes with the turbulent flow passing between the wheels from wing-side. This creates a highly turbulent region which impacts the ground-side of the aft wheel and forms a turbulent layer along the wheel contour. As fluid travels along the contour, the turbulent layer swells and shrinks with time as turbulent eddies are entrained from above. Its thickness in the figure measures about 13 mm, which is the greatest thickness observed in the video. The significant kinetic energy of the turbulence allows the boundary layer along the wheel to remain attached through extreme angles. Figure 3.10 shows separation from the back of the aft wheel at about 160 degrees, but the video shows that it is unsteady and varies between 140 and 180 degrees.

Figure 3.11 shows the wake region behind the aft wheel. Its angular extent along the wheel is much smaller than might be expected due to the delayed separation along the ground-side of the wheel. The video shows an average wake arc of about 110 degrees which propagates wing-ward as it travels downstream.

At this point it is important to note an interesting and potentially significant observation that became evident while video taping the flow with the light sheet in this orientation. Recall, from figures 3.7, 3.8 and 3.9, that the mean flow direction in the gap between the fore and aft wheels is ground-ward. The following evidence suggests that separation conditions on the wing- and ground-sides of the fore wheel greatly affect the mean flow characteristics in this region. During testing, a small air bubble approximately 2 mm in diameter, attached itself to the ground-side of the fore wheel at the point of flow separation. Observations were that this small disturbance at this specific location resulted in a state change in the mean flow between the wheels. Instead of flow in the ground-ward direction as was previously observed, the mean flow between the wheels switched to the wing-ward direction. Once the bubble was removed, the previously observed flow pattern was recovered. Further discussion of shifts to different mean flow states between the wheels will be presented later in this report.

A horizontal plane of the flow was illuminated by changing the orientation of the light sheet. This plane passed through the centerline of the axles. A corresponding image of the illuminated particle paths is shown in figure 3.12. The figure shows that fluid traveling along the outboard face of the fore wheel separates at the back edge and travels downstream to impact the outboard edge of the aft wheel. Recall from the dye visualization studies that this fluid is highly turbulent.

The single image shown here suggests that the flow is steady, but video of the particle paths show that it is rather dynamic. At times, large turbulent eddies in the wake of the fore wheel are ejected out into the freestream and travel down the outboard face of the aft wheel. When flow characteristics are as shown in the figure, the incident flow splits and a portion travels down the outboard face of the aft wheel. The rest carries turbulent eddies across the forward face and over the inboard edge of the aft wheel to impact the axle downstream.

3.3 Concluding Remarks

A qualitative analysis of the flow field around a 13% scale model of a 4-wheel landing gear bogie was conducted in a water channel using dye visualization and particle tracing. Tests were conducted at a Reynolds number based on wheel diameter of 15,000. Analysis of video tape and still images identify mean flow characteristics around the model that are unique to this geometry and may contribute to noise production.

The model exhibits geometric symmetry on either side of a vertical plane parallel to the freestream, passing through the centerline of the center support strut. Therefore, we might expect flow conditions on either side of this plane to exhibit symmetry. Similar geometrical symmetry does not exist, however, about any horizontal plane, due to the presence of the center support strut (fig 2.3). Therefore, when considering the flow patterns on either side of a plane passing through the wheel axles, differences are expected. Qualitative visualization has shown that the most significant asymmetry of the flow field is the location of separation on the wing- and ground-sides of the fore wheel. This asymmetry affects all other features of the flow at downstream locations. Separation is delayed on the wing-side, and the flow is deflected ground-ward between the wheels. In turn, this asymmetry affects separation conditions on the aft wheel. Laminar separation is observed on the wing-side and turbulent separation on the ground-side. Since the turbulent characteristics on the ground-side of the wheel delay separation, the downstream wake behind the aft wheel is deflected in the wing-ward direction.

When considering flow features important to noise generation, it is appropriate to confine our assessment to the effects of shedding vorticity in the near-wake and turbulent inflow. These are viewed as the most significant noise contributors for this geometry. On the fore wheel, flow separation occurs on both the wing-side and ground-side of the wheel. The consequent turbulent wake impinges upon the aft wheel downstream. The wing-side flow from the fore wheel is expected to be an extremely significant noise contributor. After impingement upon the aft wheel, the flow is deflected into the gap between the fore and aft wheels, where it mixes with flow from the opposite side of the gap. This mixing creates an especially turbulent region which impinges upon the ground-side of the aft wheel. It then develops into a layer of turbulent fluid that remains attached to the aft wheel through angles as great as 180 degrees, before separating.

Another potentially significant noise contributor is the turbulent flow that develops along the outside of the fore wheel. At the downstream edge of the wheel, the flow separates. This separated flow then impinges in the forward edge of the aft wheel. At the stagnation point, the flow splits. Part of it traveling along the outside of the aft wheel. The remainder is directed across the forward face and around the inboard edge of wheel. From there it is directed downstream where it eventually impinges upon the rear axle.

Finally, the wake of the aft wheel is a potentially significant noise generator in two ways. As previously mentioned, shedding of vorticity into the wake region is an expected source of landing gear noise. Another potential source, is impingement of the wake of the wheels on downstream components such as the flaps (Block, 1977). The preceding results show that the aft wheel wake tends toward the airframe, making it more likely to impact downstream components.

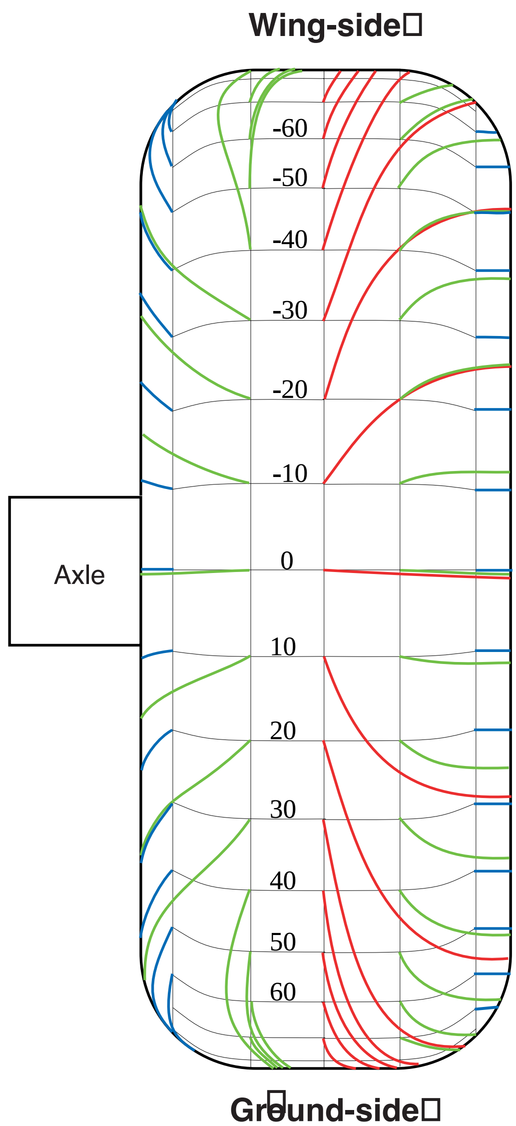

Figure 3.1 Dye streaklines along forward face of fore wheel.

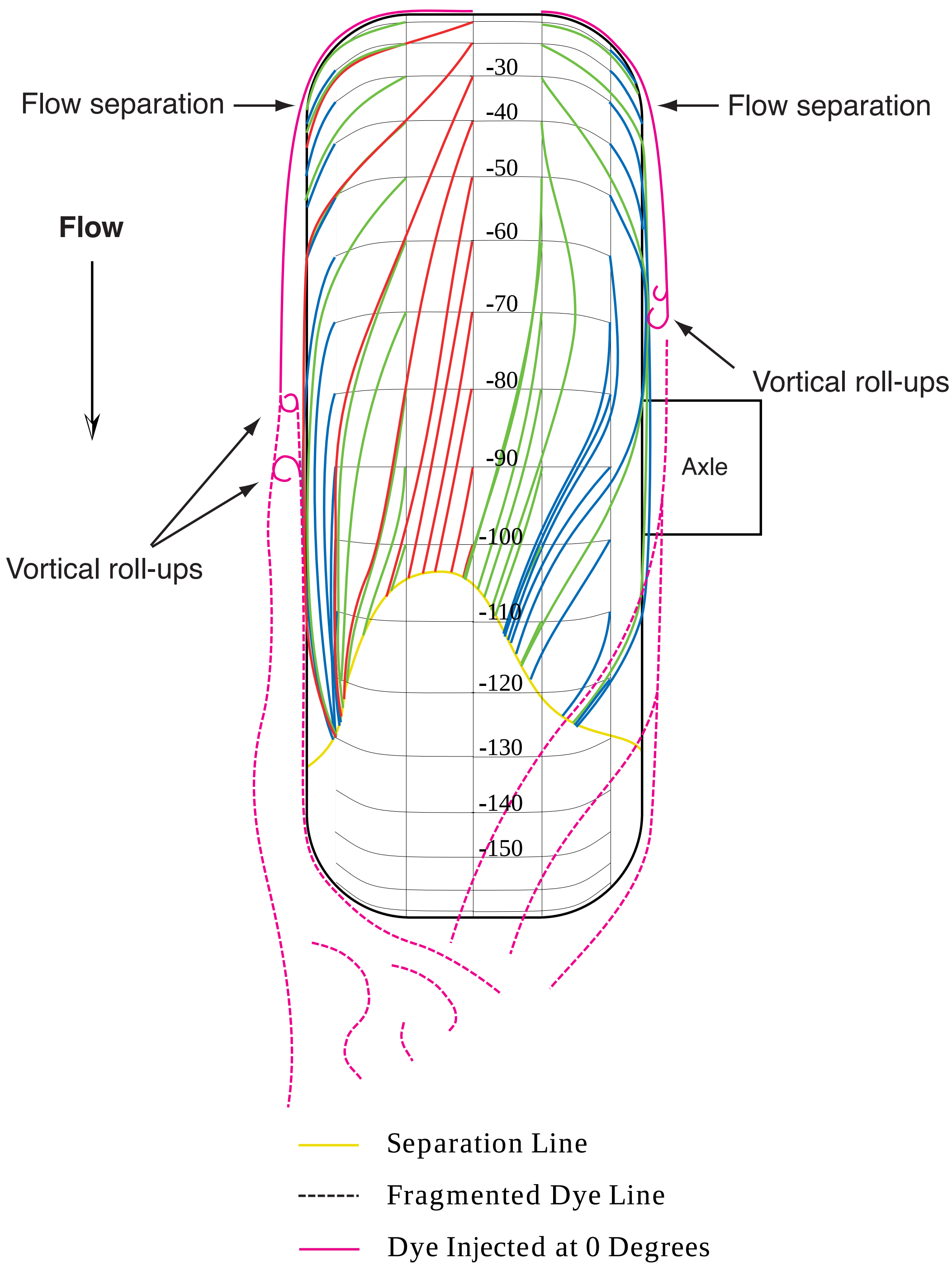

Figure 3.2 Dye streaklines along wing-side of fore wheel.

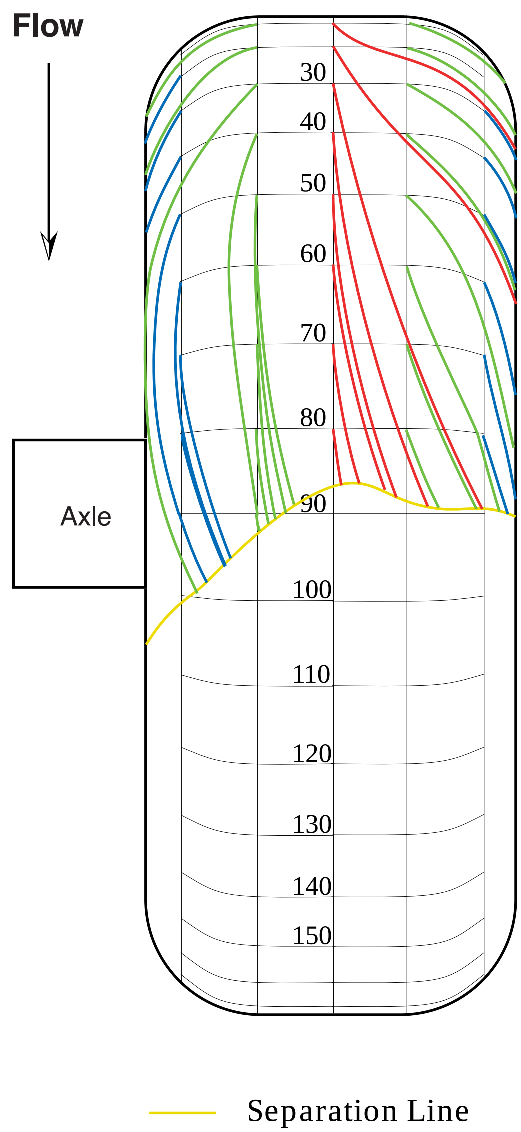

Figure 3.3 Dye streaklines along ground-side of fore wheel.

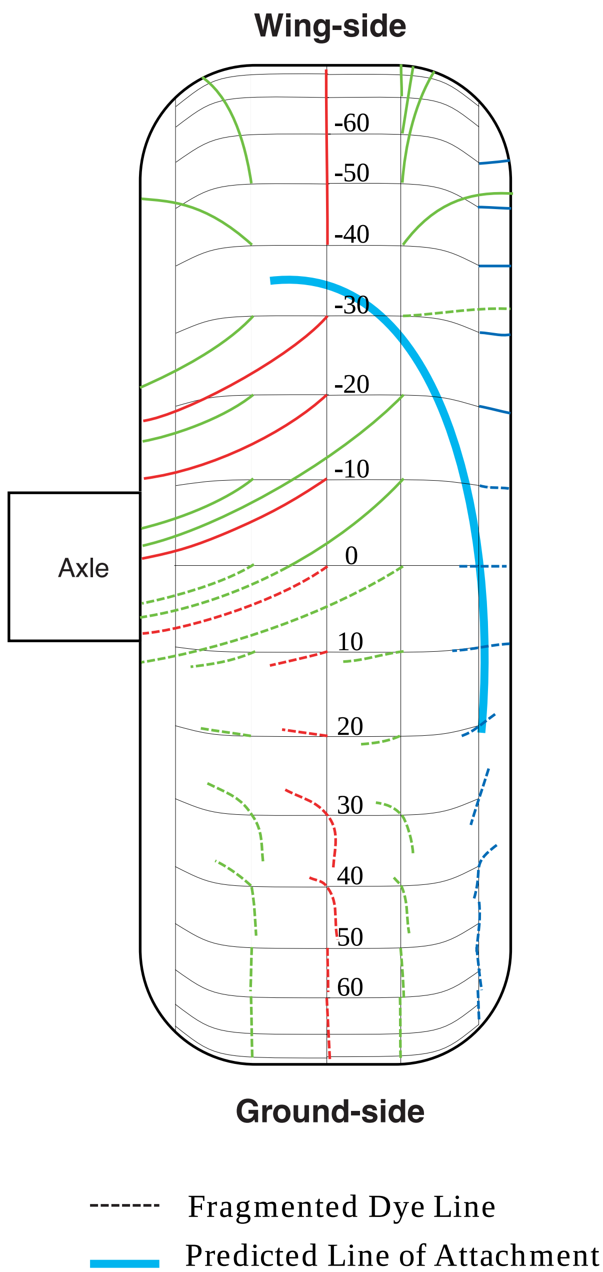

Figure 3.4 Dye streaklines along forward face of aft wheel.

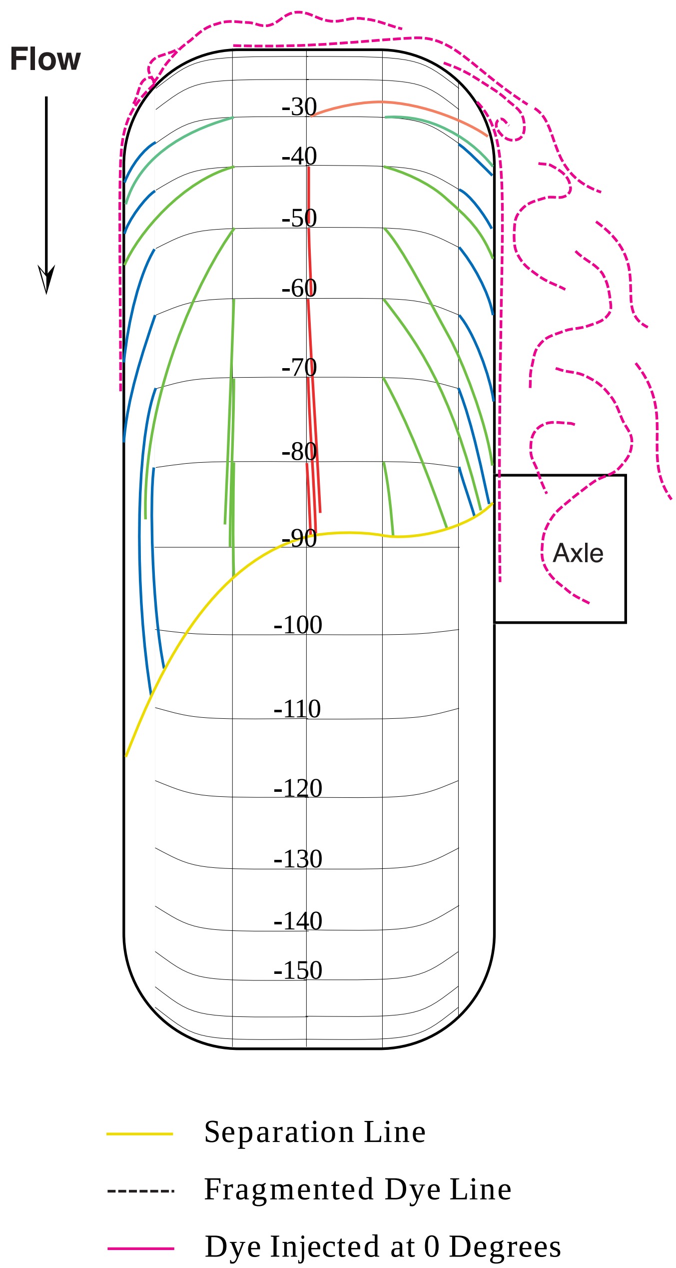

Figure 3.5 Dye streaklines along wing-side of aft wheel.

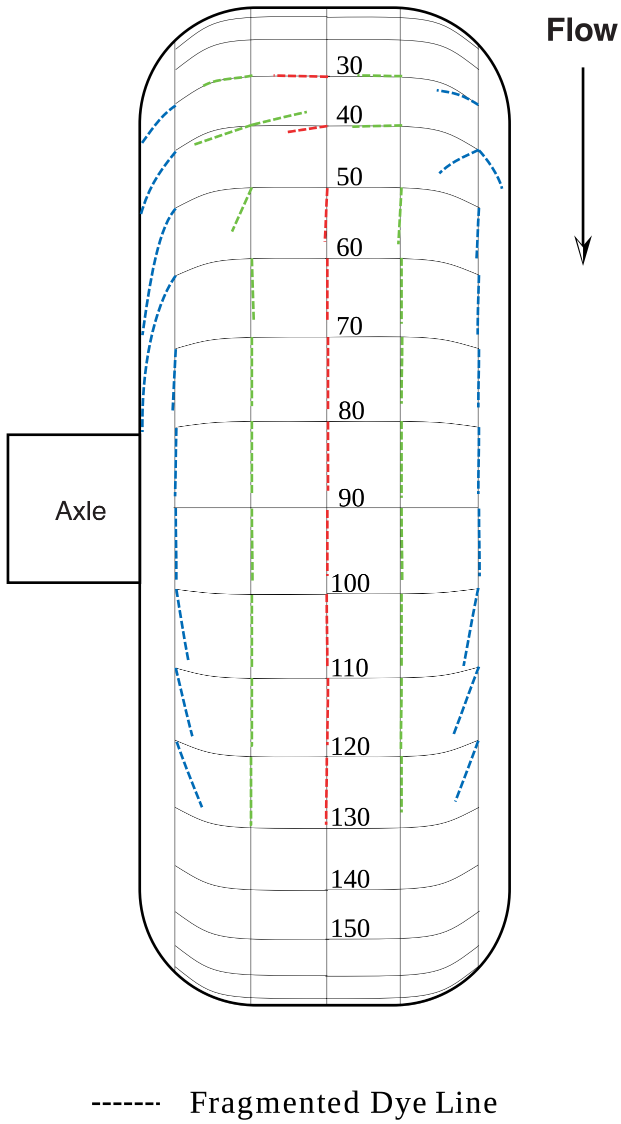

Figure 3.6 Dye streaklines along ground-side of aft wheel.

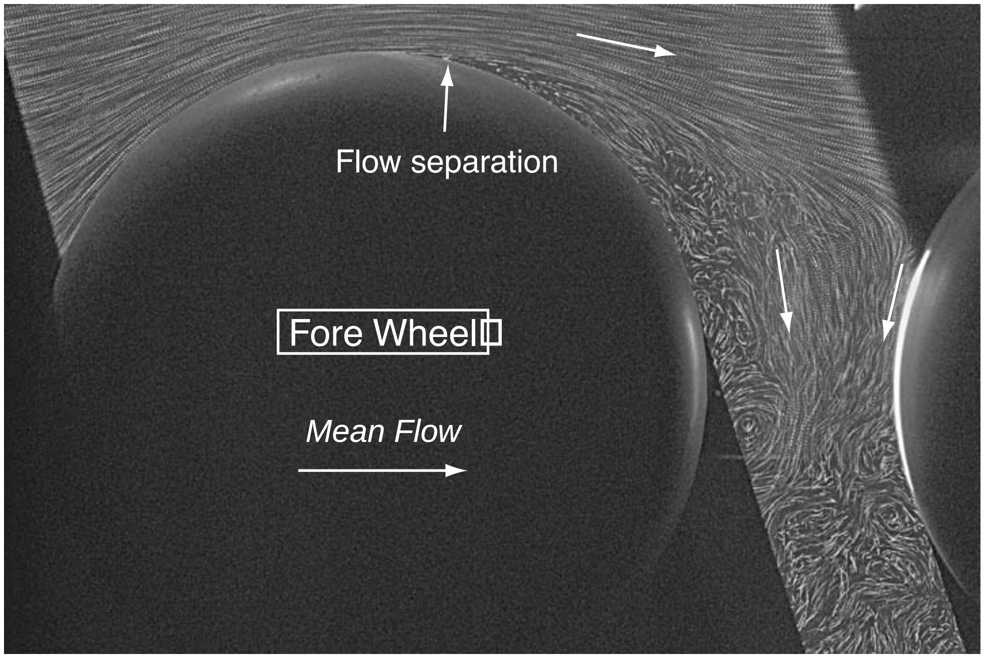

Figure 3.7 Particle paths along center plane of in-line wheels. Light sheet source angled downstream. View: wing-side fore wheel and between in-line wheels.

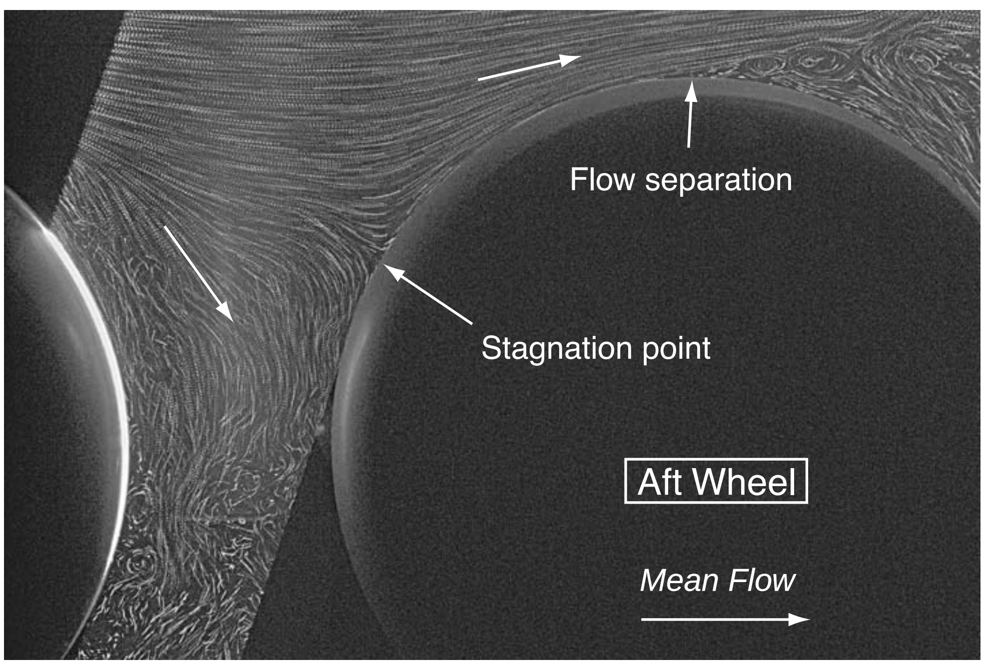

Figure 3.8 Particle paths along center plane of in-line wheels. Light sheet source angled upstream. View: wing-side aft wheel and between in-line wheels.

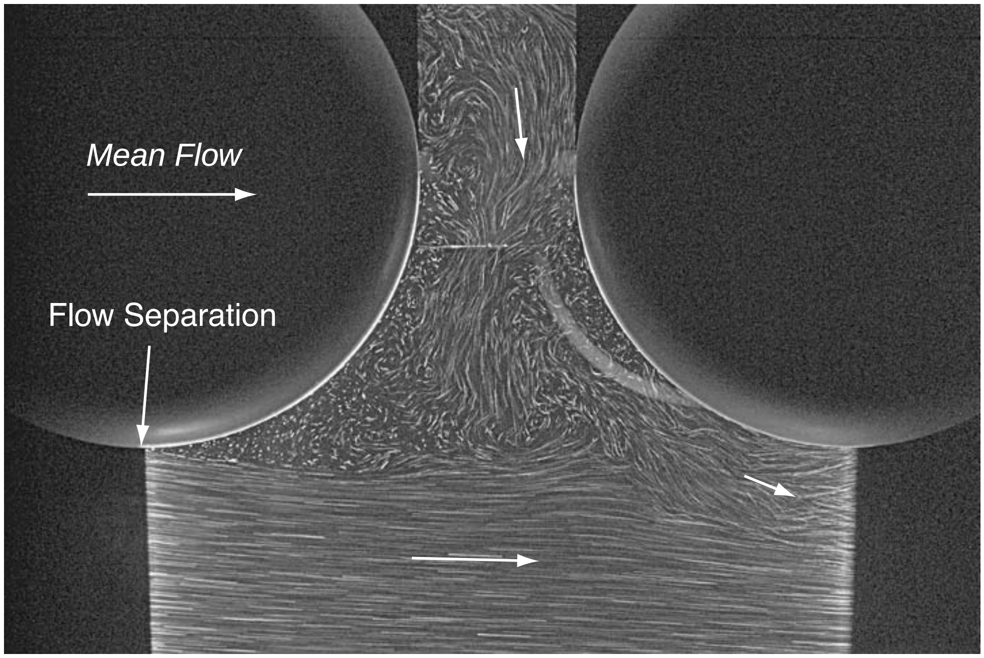

Figure 3.9 Particle paths along center plane of in-line wheels. View: ground-side and between fore and aft wheels.

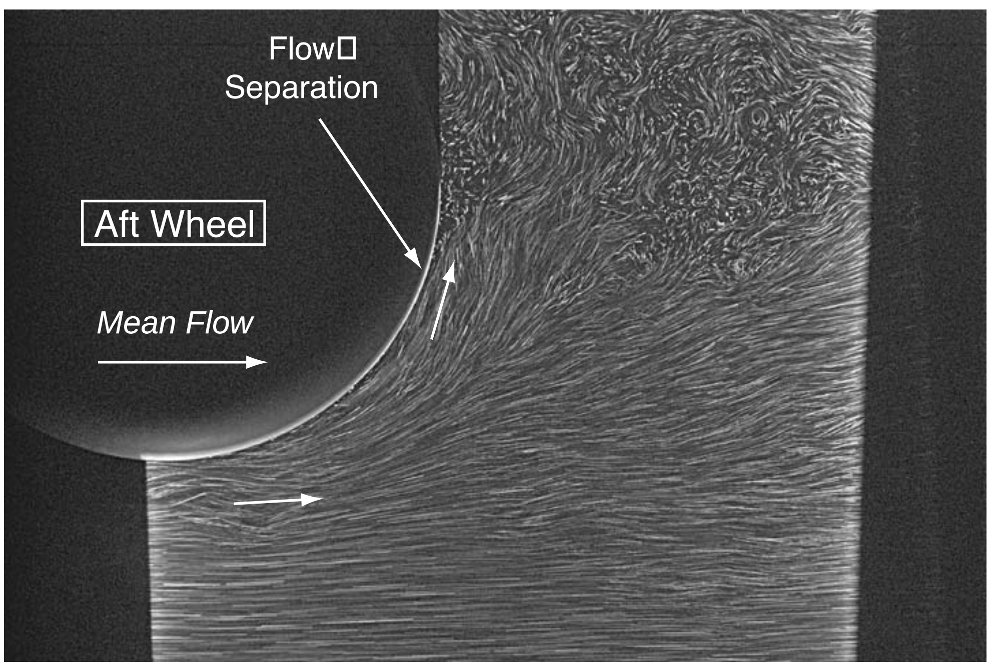

Figure 3.10 Particle paths along center plane of in-line wheels. View: ground-side and behind aft wheel.

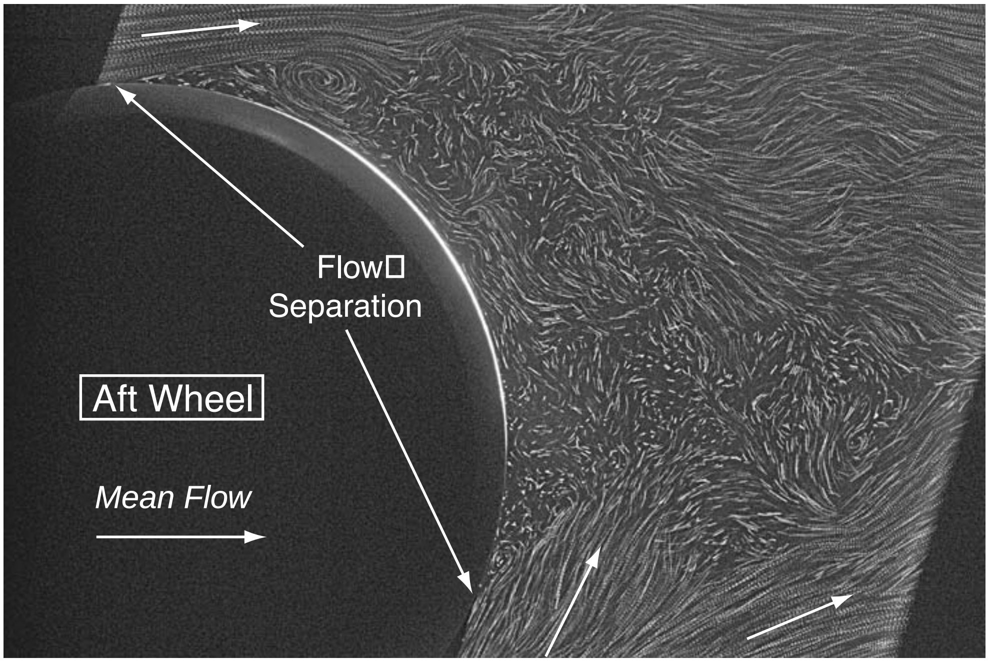

Figure 3.11 Particle paths along center plane of in-line wheels. View: wing-side and behind aft wheel.

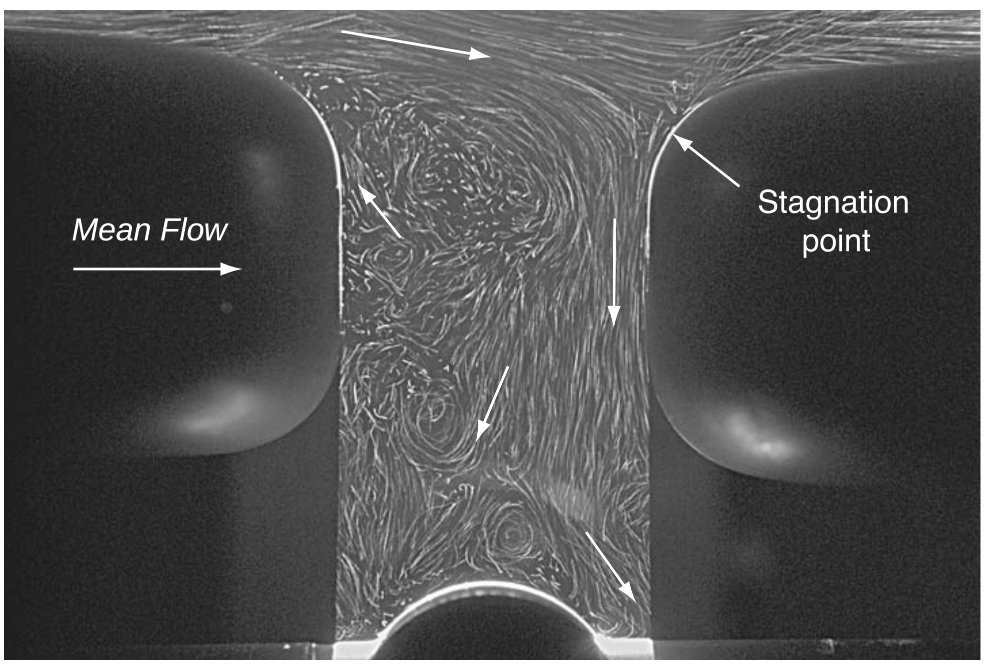

Figure 3.12 Particle paths in horizontal midplane of wheels. View: between fore and aft wheels.

4 Detailed Features of Mean Flow Field

In the previous section, a qualitative and cursory examination was performed of the flow field around a model of a 4-wheel landing gear bogie. While the studies provided valuable insight into the general flow field characteristics, the facility and experimental techniques used were limiting. Studies in the water channel had to be conducted at a low Reynolds number because flow speeds were necessarily low, and the test section was small. Dye visualization provided useful information in laminar flow regions, but was relatively ineffectual in turbulent or separated flows. Particle tracing yielded a good representation of the flow field, but provided information in only two-dimensions.

Changes in some of the mean flow field characteristics are expected at higher Reynolds numbers. Therefore, this phase of the investigation was conducted in the Basic Aerodynamics Research Tunnel (BART), which provided Reynolds numbers closer to flight conditions. While tests were conducted at four different Reynolds numbers in this facility, the following discussion will concentrate on data acquired at Re_d = 600,000. Three experimental techniques were used to gather mean flow field data: oil flow visualization; surface static pressure measurements; and Digital Particle Image Velocimetry (DPIV). Specifics of the facility and the model are presented in Section 2.2.

4.1 Wheel Surface Characteristics

Since the flow field around the configuration of interest is three-dimensional, the data acquired should be able to characterize features of the three-dimensionality. One of the easiest ways to do this is to determine flow features at the model surface; which are linked to the three-dimensional flow away from the surface. This was accomplished on the fore and aft wheels by measuring mean surface static pressures and characterizing surface shear stress lines with oil flow visualization. Details of these two experimental techniques are given in Sections 2.2.1 and 2.2.2.

To more efficiently analyze the pressure and shear stress data, values of pressure coefficient were mapped, together with the oil flow images, onto three-dimensional computer representations of the model wheels. Accurate positioning of the oil flow images was accomplished by adding fiduciary marks to the imaged wheel before testing. The pressure coefficient is determined as $C_p = \frac{P - P_s}{P_t - P_s}$, where P is the measured pressure, P_s is the tunnel static pressure, and P_t is the tunnel total pressure. Values of pressure coefficient are represented visually in the following figures using a color map with white representing the highest value and blue the lowest.

After mapping the data sets, six different images were recorded of both the front and rear wheel computer representations: four images around the wheel periphery and one each of the outboard and inboard faces. A topological analysis of shear stress lines was then conducted on each of the 12 images using topology concepts described by Tobak & Peake (1982), Hornung & Perry (1984), Perry &

Chong (1987), and Chapman & Yates (1991). Renderings of the perceived shear stress lines are represented in either yellow or blue depending on which color best contrasted with the image background. In the following discussion, the azimuthal location on the wheels is defined in the same manner as that used for the water channel studies, with positive angles toward the ground-side of the model. Recall, however, that for the wind tunnel studies, the model was inverted in the facility.

4.1.1 Interpretation of Surface Shear Stress Patterns

If the surface of a body is coated with a thin layer of oil containing a suspension, and placed in a potential flow, a pattern will persist in the oil as the flow moves the particles of the suspension. These patterns are a result of shear stresses developed as the fluid acts on the oil film, and the particle streaks formed in the oil are commonly called shear-stress lines.

Critical point theory (Perry & Fairlie, 1974) tells us that certain recurring patterns are expected in the shear-stress lines around singularities in the skin-friction vector field. At these points, the vector magnitude is zero and the direction of the corresponding skin-friction vector is indeterminate. Patterns predicted by theory include foci, nodes and saddle points. Other patterns that consistently emerge, but are not predicted by theory, include positive and negative bifurcation lines. These patterns are summarized in figure 4.1.

If we are to use the patterns formed in the shear-stress lines to make predictions about the external flow field, we must consider the relationship they have with one another. Using the equations of motion that govern the oil, of thickness h, applied to the surface of a body, Squire (1962) solved directly for the components of velocity at the oil surface.

$$u_2 = \lambda\left\{\left(\frac{1}{\mu_1}\frac{\partial p}{\partial x}\right)\left(\frac{z^2}{2} - h\,z\right) + \left(\frac{\partial u_1}{\partial z}\right)_{z=h} z\right\} \tag{4.1}$$

$$v_2 = \lambda\left\{\left(\frac{1}{\mu_1}\frac{\partial p}{\partial y}\right)\left(\frac{z^2}{2} - h\,z\right) + \left(\frac{\partial v_1}{\partial z}\right)_{z=h} z\right\} \tag{4.2}$$

The corresponding coordinate system is shown in figure 4.2. In the above equations, the subscripts 1 and 2 refer to the boundary layer flow and the oil respectively; μ is the viscosity and $\lambda = \mu_1/\mu_2$. Dividing equation 4.2 by 4.1,

$$\frac{dy}{dx} = \frac{\dfrac{\partial v_1}{\partial z} + \dfrac{1}{\mu_1}\dfrac{\partial p}{\partial y}\left(\dfrac{z}{2} - h\right)}{\dfrac{\partial u_1}{\partial z} + \dfrac{1}{\mu_1}\dfrac{\partial p}{\partial x}\left(\dfrac{z}{2} - h\right)} \qquad (0 \le z \le h) \tag{4.3}$$

we obtain a relationship between the oil streamline direction and the external flow velocity. Evaluating equation 4.3 at z=0, it is clear that if the oil film thickness, h, is small enough to be unaffected by the pressure gradient, the oil streamlines (shear-stress lines) will be aligned with the streamlines of the external flow nearest the wall, such that, $dy/dx = \partial v_1/\partial u_1$. Lighthill (1963) suggests that because of this relationship, shear-stress lines may be called 'surface streamlines' or 'limiting streamlines'. Hunt et al (1978) points out that while a link between shear-stress lines and surface streamlines is clear, two assumption must be made to expect similar critical point patterns in the skin-friction vector field and the velocity vector field. First, we must assume that a singular point in one corresponds to a singular point in the other.

Second, we must assume that the characteristics of skin-friction and velocity are the same near these points.

Considering the close relationship between the two vector fields and making the assumptions of Hunt et al (1978), we can use patterns in the shear-stress lines (hereafter referred to as surface streamlines) to infer off-surface characteristics of the external flow field. The literature demonstrates that this can be done quite successfully (Chapman & Yates, 1981; Peake & Tobak, 1982; Hornung & Perry, 1984; Chong & Perry, 1986; Perry & Chong, 1987; Dallmann et. al., 1990).

Since singularities in the surface streamline vector field occur at points of flow attachment and separation, we begin initially by considering which flow patterns correspond to attachment and which correspond to separation. Referring again to figure 4.1, all patterns that correspond to flow attachment are shown in the left-hand column, those that correspond to flow separation are shown in the right. The obvious trend here is that when surface streamlines diverge from a point or line, that point or line represents flow attachment. When surface streamlines converge on a point or line, that point or line represents flow separation. Note a saddle-of-attachment has the same flow pattern as a saddle-of-separation when it is rotated by 90 degrees. Note, too, that far from the singularity located at the center of a saddle point, the critical lines, which are highlighted in the figure, appear as bifurcations. The critical line of an attachment saddle appears as a positive bifurcation and the critical line of a separation saddle appears as a negative bifurcation. Throughout the following figures, critical lines and bifurcations will be color coded as they are in figure 4.1.

By combining the simple surface streamline patterns presented in the foregoing, more complex external flow features can be inferred. For example, Hornung & Perry (1984) refer to the experimental work of Werlé (1962) and the analysis of Legendre (1965) to combine a saddle, a stable node and a positive bifurcation to infer a Werlé-Legendre separation (fig 4.3). Chong & Perry (1986) use a fifth order Taylor Series expansion of the three-dimensional momentum and continuity equations about singular points to show that the surface streamline pattern of a saddle-of-separation in relative line with a saddle-of attachment, represent what they call an owl-face of the first kind. Figure 4.4a shows the calculated surface streamline pattern for the offset saddles, while figure 4.4b shows the calculated off surface streamlines.

In the following discussion, basic flow patterns cited in figure 4.1, as well as their combinations, will be highlighted in the figures. Using the diagnostic logic of the aforementioned authors, off surface flow features will be inferred corresponding to these patterns. Terminology used to describe surface flow patterns and inferred off surface flow features are defined in figure 4.5. Figure 4.5a portrays the characteristic recirculation within a separation bubble. Figure 4.5b illustrates an open ended separation bubble. Such a separation bubble consists of an upstream saddle-of-separation and a downstream saddle-of-attachment, as with any separation bubble. In this case, however, the critical lines of the saddles do not connect to one another, and the bubble is cylindrical in shape. In figure 4.5c, the recirculation pattern is portrayed in the surface streamlines under a symmetric separation bubble. Figure 4.5d is a three-dimensional representation of the closed separation bubble that produces the surface pattern of 4.5c.

4.1.2 Fore Wheel

Shown in figure 4.6 is a composite image of the front of the fore wheel with color coded static pressure signature and oil flow lines. Renderings of the surface streamlines are in yellow with arrows, which indicate their direction. The axle is included to identify wheel orientation, and a representative fiduciary mark is highlighted.

In the center of the wheel, an ellipse is drawn around a node of attachment. This identifies the high pressure region that is visually apparent in the oil flow. The center of the oval, which is marked with a green dot, is where one might expect the stagnation streamline. This position does not correlate, however, with what was observed in the dye visualization experiments discussed in Section 3.1.1. While the mark is inboard of the vertical centerline, as expected, it is displaced in the ground-ward direction from the horizontal centerline, i.e., opposite of what was previously observed. Using the mean pressure data, the position of the highest pressure value was located on the wheel. This point is marked by the red dot in the figure and reflects the expected shift in the stagnation streamline location due to the flow obstruction created by the axles and the center support strut. To resolve the disparity between the visually apparent and the measured location of maximum pressure, five pressures to either side of the pressure peak are plotted in figure 4.7.

The figure shows that pressure is skewed toward the ground-side of the wheel and the pressure peak does not lie in the center of the maximum pressure region.

Returning to figure 4.6, we see that the surface streamlines emanate from the high pressure center. Most tend toward the outboard side of the wheel where the pressure is lowest, as is apparent in the pressure signature.

On the outboard face of the wheel, represented by figure 4.8, the pressure signature indicates a large favorable pressure gradient in the middle of the wheel, along the forward edge. This is seen as the color variation from red, to green, to deep blue. This gradient is associated with a rapid acceleration of fluid around this corner of the wheel. At the end of surface curvature, the flow experiences a sudden adverse pressure gradient and a laminar saddle-of-separation is formed. This is highlighted in the figure with its critical line colored red, and labeled **A**. It extends along the entire front edge of the wheel. After separation, it is hypothesized that the flow undergoes transition and turbulent reattachment occurs. The saddle-of-attachment is highlighted in the figure just downstream of the saddle-of-separation. Its critical line is colored purple, and labeled **B**. It also extends along the front edge of the wheel.

Between the critical lines of the saddle-of-separation and the saddle-of-attachment, the flow is postulated to recirculate in what was previously defined as an open ended separation bubble in figure 4.5. Note that the surface streamline connecting the singularities at the center of each saddle is in the upstream direction. Considering the regions near the wing- and ground-sides of the wheel, the surface streamlines between the critical lines become increasingly tangent to the critical lines. At the points labeled C, on the critical line B, which is associated with the saddle-of-attachment, the flow direction reverses, resulting in the formation of positive bifurcations on each end. These are highlighted in the figure as dashed white and purple lines. These bifurcation lines follow the same course set by the critical line and extend over the edges to the ground- and wing-sides of the wheel. The flow direction along the critical line associated with the saddle-of-separation is maintained, as it follows a similar course over the edges of the wheel.

Figure 4.8 shows that, after reattachment along the front edge of the wheel, surface streamlines are oriented in the downstream direction along the outboard face of the wheel. In this region, the pressure is relatively constant. At the downstream edge of the wheel, surface curvature results in another adverse pressure gradient, and turbulent separation occurs along a negative bifurcation, labeled D. The figure also shows that a large number of surface streamlines merge into the ground-side end of the bifurcation, at E. On its wing-side end, the bifurcation forms an arc where a large pool of oil is formed (F). This change in the surface pattern is hypothesized to represent the roll up of a vortex sheet as it leaves the surface, similar to that portrayed in figure 4.3b. Further downstream, around the edge of the wheel, a saddle-of-separation (G) forms, as well as an additional negative bifurcation (H). This is where fluid on the backside of the wheel separates as it travels toward the outboard face. These will be addressed in further detail later in the text.

Figure 4.9 shows the inboard side of the fore wheel. Along the forward edge, we see surface streamline and pressure signatures similar to those on the outboard side, in the previous figure. The surface streamlines indicate that flow remains attached as it negotiates the edge curvature of the wheel till it experiences a sudden adverse pressure gradient at the end of curvature. Here the flow separates; correspondingly a saddle of laminar separation forms. Turbulent reattachment is then postulated along a saddle of turbulent attachment. Between the critical lines associated with each saddle, the flow recirculates in an open ended separation bubble, as on the opposite side of the wheel (fig 4.8). Considering the regions away from the singularities located at the center of the wheel, the surface streamlines between the critical lines become increasingly tangent to the critical lines. At the points labeled A on the critical line associated with the saddle-of-attachment, the flow direction reverses, resulting in the formation of positive bifurcations on each end, as indicated in the figure. Note too, that the flow between the critical lines also reverses direction and is carried over the edges of the wheel, at the points B in the figure.

The presence of the axle on the inboard side of the wheel significantly alters the flow pattern downstream of the forward edge of the wheel. After reattachment along the leading portion of the wheel, the flow experiences an extreme adverse pressure gradient ahead of the axle. It again separates along a saddle-of-separation and reattaches directly in front of the axle at a saddle-of-attachment. The critical lines of the saddles are labeled in the figure C and D respectively for the saddle-of-separation and the saddle-of-attachment. Between these lines, the recirculating flow takes the form of a horseshoe vortex at the juncture of the axle and the wheel. Note that only a single vortex is indicated by the single line of separation (C) and the single line of attachment (D). This is expected, as the incoming boundary layer is predicted to be turbulent, and turbulent juncture flow has been shown by Pierce & Tree (1990) to result in a single vortex. Using smoke visualization the authors found turbulent juncture flow, "to be strongly time-variant with large changes in the size and position of the dominant vortex structure." They also determine the existence of only a single juncture vortex using two component Laser Doppler Velocimetry. In their experiments, the time averaged center of the vortex "appeared to coincide with a clear, well scoured line around the [cylinder] in the surface flow visualization." Such a line is highlighted in figure 4.8. Similar results are presented by Pierce & Harsh (1983) using surface oil flow visualization and Eckerle & Langston (1987) using 5 hole probe measurements in conjunction with surface oil flow visualization.

Immediately downstream of the axle in figure 4.9, a clearly distinguishable negative bifurcation (E) forms, ending in a focus of separation. In the wake region on the wing-side of the axle, surface streamlines rapidly turn and wrap into the focus. In the wake region on the ground-side of the axle, surface streamlines make a much broader arc, extending nearly to the edge of the wheel before turning back toward the axle. At the downstream edge of the wheel, a saddle-of-separation (F) forms. Here, fluid not returning to the axle leaves the wheel surface.

In figure 4.9, patterns of surface streamlines and the pressure signature on the wing-side of the wheel, at the trailing edge, exhibit differences relative to those on the ground-side. This is expected to be due to the presence of the center support strut, located on the wing-side of the wheel. On this side, a rapid acceleration around the edge of the wheel is suggested by the highly favorable pressure gradient in that region. This is seen as the color gradation from yellow, to green, to blue. It is expected that the flow here is locally accelerated as it passes between the wheel and center support strut. It then separates at the saddle, labeled H. On the ground-side of the wheel, the pressure gradient is not as favorable, and surface streamlines converge to separate along a negative bifurcation, labeled **G**.

On the ground-side of the wheel, shown in figure 4.10, two adjacent pools of oil are evident in the center of the wheel image. The flow patterns observed in these pools during testing are drawn in this figure. The recirculating characteristics of these patterns suggest that the oil pools lie beneath a complex pairing of separation bubbles. In the present text, these patterns will be referred to as recirculation zones.

From the surface streamline patterns, it appears that the upstream recirculation zone is initiated along a saddle-of-separation (A) located just past 90 degrees around the wheel from the leading edge. Separation is a result of an adverse pressure gradient that becomes stronger with increasing azimuthal angle around the wheel. It is expected that separation is laminar, but reattachment is postulated to occur along a positive bifurcation (B) after the flow becomes turbulent.

This reattachment forms the downstream boundary of the upstream recirculation zone.

The existence of the downstream recirculation zone is expected to be dependent, in some way, on the process of flow separation and attachment that begins at the saddles located on the forward edges of the inboard and outboard sides of the wheel (see figures 4.8 and 4.9). As seen in figure 4.10, the two critical lines, labeled *C*, associated with the saddles-of-separation developed at the forward edges of the wheel, extend from the side of the wheel, and eventually merge with the back of the upstream recirculation zone. The positive bifurcation lines, labeled D, follow a similar course, and connect to form the trailing boundary of the downstream recirculation zone, labeled E. In the figure, this downstream boundary is colored purple to represent the critical line of a saddle-of-attachment. Fluid between the critical lines *C* and D, on each side of the wheel, is continually drawn toward the ground-side of the wheel into the downstream recirculation zone. Separation ensues along lines of negative bifurcation (F), which delineate the sides of the recirculation zone, so that the fluid within is now bounded by an enclosure. During testing, fluid within the enclosure was observed to circulate in two different states. Fluid immediately downstream of the enclosure was observed to flow in either an upstream or downstream direction, as indicated by the double headed arrows in the figure, depending on the state of circulation within the enclosure. Changes in flow state occurred erratically, and the length of time a particular state persisted, varied from less than one second, to several seconds.

Figure 4.11 shows surface patterns corresponding to the observed primary and secondary states of circulation. Figure 4.11a shows the state of flow observed a majority of the time, and therefore considered the primary state. In this state, a saddle-of-attachment forms the trailing edge of the downstream recirculation region, and flow immediately downstream of this region is in the downstream direction. This state corresponds to what is shown on the wheel in figure 4.10. In the secondary state, shown in figure 4.11b, a saddle-of-separation forms the trailing edge. Note that the flow lines within the recirculation region reverse direction; correspondingly, the surface streamlines immediately downstream also reverse direction. These models, are provided as examples of possible flow features associated with the observed states of recirculation. A clear understanding of the flow physics associated with each of these states could not be determined with currently available information.

Figure 4.12 shows that, on the wing-side of the wheel, the flow patterns are generally similar to those on the ground-side, except that features following separation are markedly different. On this side of the wheel, flow separation is initiated at a saddle (*A*) about 5 degrees beyond that on the ground-side, and is characterized by what Hornung & Perry (1984) call, a Werlé-Legendre separation. As shown in figure 4.3, the distinguishing feature of this type of separation is that the critical line beginning at the saddle persists downstream on one side, while the other side ends in a focus. The figure also shows that a positive bifurcation is often associated with this type of separation. In figure 4.12, the positive bifurcation associated with the separation, beginning at A, can be seen at the very bottom of the image, and is labeled B. It is more clearly seen when viewing the backside of the wheel in figure 4.13. This positive bifurcation is farther downstream than would normally be expected. This downstream shift is hypothesized to be due to the extreme surface curvature of the wheel.

Referring again to figure 4.12, further observations can be made about the surface streamlines downstream of the saddle-of-separation. On its inboard side, fluid is drawn up behind the critical line by the focus of separation, which rotates in a counter-clockwise direction. It appears, from the accumulation of oil, that much of the fluid is then deposited behind the outboard side of the critical line where it is eventually ejected downstream. This accumulation is labeled C in the figure. It is not clear what effect, if any, the critical lines associated with the saddles-of-separation (D) and the positive bifurcation lines (E) extending from the inboard and outboard sides of the wheel have on the separation process at this location. On the ground-side of the wheel (fig 4.10), they appeared to have a significant influence, as previously discussed.

The complexity of the surface flow structure on the backside of the wheel is evident in figure 4.13. Separation is prevalent and occurs along saddles and bifurcations that end in foci. Flow attachment is also observed, however, at a node and along a positive bifurcation.

As previously mentioned, the Werlé-Legendre separation observed on the wing-side of the wheel is expected to have a positive bifurcation associated with it (see figs 4.3 & 4.12). This bifurcation (A) is highlighted in figure 4.13 as the dashed purple and white line. After attaching along the bifurcation, flow is oriented toward the sides of the wheel where fluid feeds into the critical line of a saddle-of-separation (B) on the inboard side and a negative bifurcation (C) on the outboard side.

In the middle of the wheel, a node of attachment is encircled in black to distinguish the area where the direction of the surface streamlines is imperceptible. It is not expected that the node and positive bifurcation are related to each other, in that they do not result from the same external flow phenomenon. Evidence of their uniqueness is found in the pressure signature. At the start of the bifurcation, located at the bottom of the image, pressure is high. But as one follows the bifurcation around the wheel, the magnitude of the pressure decreases. Pressure again increases, over a broader surface area, at the attachment node. If the positive bifurcation and attachment node were a result of the same external flow phenomenon, one would expect smoother connectivity between the surface pressure features just described for each.

None of the surface streamlines originating from the attachment node appear to be oriented in the wing-ward direction. This observation, along with the orientation of the streamlines emanating from the positive bifurcation, highlight the fact that the mean flow on a major portion of the backside of the wheel is ground-ward. All surface streamlines emanating from the node separate along critical lines (B, D, E). Each of these lines ends in a very concentrated focus of separation, as denoted in the figure. The location of the saddles-of-separation associated with the critical lines can be determined by either the appearance of stagnation streamlines, or the divergence of streamlines about the critical point.

Between the critical line (E) on the outboard side and the negative bifurcation (F) on the outboard face (seen more clearly in fig 4.8), a region develops where the flow velocity is nearly zero. This is suggested by the surface streamlines and the surface pressure signature. The magnitude of surface pressure in this region is close to the ambient static pressure in the tunnel test section, as indicated by the red coloring.

One more topological characteristic is apparent in viewing the backside of the fore wheel (fig 4.13). In the lower right portion of the image, the surface streamlines suggest the formation of a saddle-of-separation (G), which has with a critical line of short extent. This was noted previously during the discussion of figure 4.9. Flow characteristics in the arc of the critical line cannot be distinguished due to the accumulation of oil in this region. This saddle is followed immediately by a negative bifurcation (H). Flow originating from the inboard side of the wheel, separates along these lines.

4.1.3 Aft Wheel

Shown in figure 4.14 is a front view of the aft wheel with surface pressure coloring and oil flow lines rendered in yellow. Immediately apparent are the two large attachment nodes encircled in black. The wing-side node is clearly the largest and exhibits the highest pressure. After attachment, surface streamlines emanate from each node in all directions. Those directed toward the center of the wheel approach each other and separate along the critical lines A and B, beginning at saddles-of-separation C and D. Between the critical lines, the pressure rises. Moreover, surface streamlines follow the critical lines around the inboard edge of the wheel. On the outboard side, the critical lines merge before turning the corner at the wheel edge.

Features of the surface streamline and the region of pressure increase between the critical lines in figure 4.14, are very similar to the phenomenon previously described on the trailing outboard edge of the fore wheel (figs 4.8 & 4.13). In the vicinity of point E, in figure 4.14, the surface pressure increases significantly, and the surface streamlines diverge. These characteristics suggest that flow is directed toward the wall at this location. A surface flow pattern with these characteristics was not discovered in the literature. Therefore, further details of the flow physics associated with these surface features is not currently available.

The outboard face of the aft wheel is shown in figure 4.15. At the front-center of the wheel, around point A, the adverse pressure gradient is mild enough that the surface streamlines remain attached around the wheel edge. However, toward the wing- and ground-sides of the wheel, the gradient becomes significant and flow separation occurs along lines of negative bifurcation, labeled C and D in the figure. Downstream of separation, on the wing-side, the flow reattaches along a positive bifurcation, labeled E. Between the bifurcation lines, D and E, flow recirculation is hypothesized to occur, as suggested by the surface streamlines. At the edge of the wheel (F), the bifurcation lines merge and terminate. On the ground-side, only a single bifurcation line is readily apparent. Convergence of the surface streamlines suggests it is a line of negative bifurcation where the flow separates. This line of separation, labeled C in the figure, is located at the same downstream position as the positive bifurcation on the wing-side (D). While downstream of line C a distinct positive bifurcation is not apparent, surface streamlines suggest that reattachment does occur. The inability to distinguish a line of reattachment is likely due to the lack of resolution available using the current experimental technique. Reattachment is expected immediately downstream of separation, along a positive bifurcation, labeled G. Differences in streamwise separation location on the wing- and ground-sides in this figure appear due to the location of the adverse pressure gradient associated with each side.

Downstream of the positive bifurcation lines, that are defined in figure 4.15, the surface streamlines along the outboard face of the wheel are oriented in the downstream direction. At the edge of the wheel, an adverse pressure gradient develops and flow separates along a negative bifurcation (H). The surface streamline pattern here looks very similar to that on the outboard trailing edge of the fore wheel (fig 4.8). A large number of surface streamlines merge into the bifurcation at its ground-side end (I) and an arc is formed at its wing-side end (J), which is indicative of a focus of separation.

On the inboard face of the aft wheel, shown in fig 4.16, a significant adverse pressure gradient upstream of the axle is not apparent; this is dramatically different from what was observed on the fore wheel (fig 4.9). This difference is likely associated with differences in the flow fields that each wheel encounters. Severe distortion of both the mean and turbulent flow fields surrounding the aft wheel is expected; it is located in the wake of the fore wheel.

The surface streamlines in figure 4.16 indicate that flow from the ground-side of the front face, denoted as A in the figure, does not separate at the wheel edge, and streamlines maintain their direction toward the axle. However, on the wing-side of the wheel, at B in the figure, the flow separates along a negative bifurcation (C) and is expected to immediately reattach along a positive bifurcation (D). The streamlines here are redirected away from the axle as they converge along the negative bifurcation. The fact that flow separates on one side of the wheel, and not the other, is expected to be due to differences in severity and location of the adverse pressure gradient at the wheel edge. Viewing the flow pattern of figure 4.16 as a whole, it is skewed toward the wing-side.

Around the axle, a vortex dominates the juncture flow, and is highlighted by a the critical lines of a saddle-of-separation and a saddle-of-attachment. The critical lines associated with each of these saddles are labeled E and F in the figure, and color coded accordingly. On this wheel, the critical lines do not suggest formation of a horseshoe vortex as was hypothesized for the juncture on the fore wheel (fig 4.9). Here, the critical lines of the saddles merge on the ground-side of the axle and terminate. This suggests the vortex does not continue around this side of the axle, but rolls up asymmetrically on only the wing-side of the axle. The skewing of the streamlines ahead of the critical line E, suggests the formation of what Perry & Chong (1987) call a distorted saddle on a finite thickness shear layer, shown in figure 4.17. In figure 4.16 a cyan line labeled G, is drawn. It is oriented at an angle to represent the direction of the streamlines that intersect the singularity of the saddle-of-separation. The exact angle, θ, that this line makes with the critical line E is uncertain, however, since oil patterns that define the streamlines between the critical lines E and F have been scrubbed away by the rotation of the vortex there.

The critical lines (H) extending from the front of the wheel, in figure 4.16, are associated with the saddles of separation on the front face of the wheel. As they extend around the edge of the wheel, they are skewed in the same direction as the streamlines above them. Further downstream, they join with each other and the critical line E, detectable around the axle.

Features of the wake implied by the surface streamlines and the pressure signature behind the axle on the aft wheel, shown in figure 4.16, are not as dramatic as they are behind the axle on the fore wheel (fig 4.9). This may be due to the asymmetry of the juncture vortex, which is expected to rapidly detach from the wheel surface downstream of the axle along the critical line E. Note that this line is of rather short extent downstream of the axle. The only wake features prevalent behind the axle are a slight pressure increase and a negative bifurcation, labeled I, that forms immediately downstream of the axle. A similar negative bifurcation, ending in a focus, was observed immediately behind the axle on the fore wheel. In the present case, however, the surface streamlines suggest that the bifurcation extends downstream and merges with the critical line created at the saddle-of-separation ahead of the axle; at this location, they both terminate.

On the ground-side of the wheel, shown in figure 4.18, the surface streamline patterns show little indication of flow separation or attachment. Here, the flow propagates smoothly across the tread area[1], remaining attached past 120 degrees around the wheel from the leading edge. Separation eventually becomes apparent as streamlines merge to form negative bifurcations (A and B), evident at the bottom of the figure.

Figure 4.19 shows that the surface characteristics on the wing-side of the wheel are similar to those on the ground-side, shown in the previous figure. On the wing-side, however, an apparent adverse pressure gradient is expected to result in the observed separation along a negative bifurcation, labeled A. The bifurcation begins at about -110 degrees around the wheel from the leading edge and forms as streamlines along the tread area merge together. In the lower left of the image, another bifurcation (B) forms where fluid from the inboard side of the wheel separates.

Figures 4.18 and 4.19 show an obvious difference in surface streamline characteristics as opposed to what was observed on the ground- and wing-sides of the fore wheel (figs 4.10 & 4.12). On the fore wheel, the surface streamlines indicate

[1] The tread area is define as the wheel periphery associated with the tire tread.

flow separation along saddles, at about 90 degrees in either direction around the wheel from the leading edge. On the aft wheel, surface streamlines are continuous over much of the tread area with separation occurring at locations further downstream along negative bifurcations. These differences in the flow feature are likely due to the distortion of the flow field around the aft wheel, which is located in the wake of the fore wheel.

Figure 4.20 is an image of the backside of the aft wheel. Here the flow speed is low, and the flow direction is expected to be erratic. These external flow features are suggested by the nearly uniform pressure distribution of relatively high value (compare with the backside of the fore wheel, fig 4.13). Further evidence of these external flow features is the observed behavior of the oil flow lines themselves. During testing, they often appeared to be as much under the influence of gravity as they were the external flow field. Note the consequent thickening of the lines in this region.

Some clear features of the surface flow, however, do exist in this figure. On the outboard side of the wheel, two negative bifurcations form as surface streamlines merge and separate from the surface, thereby delineating one side of a large separated region at the wheel edge. One bifurcation line (**A**) is short and is directed toward the top of the image. It intersects with the negative bifurcation (**B**) extending from the wing-side of the wheel, which was previously discussed (fig 4.19). The other bifurcation, labeled ***C***, is directed toward the bottom of the image. It is formed by the merging of surface streamlines from the ground-side of the wheel.

Though the flow direction along these two bifurcation lines is toward the same point (note the arrows at the end of each), each ends in a separate focus, as shown in the figure. This was thought at first to be an anomaly, or a mistake in surface streamline characterization. But two replications of this test under the same conditions showed the very same result. Chapman & Yates (1991) point out that, "under some conditions isolated singular points may occur so close together that it is difficult to distinguish among them."

Two other negative bifurcations are rendered in figure 4.20. The one (D) begins at the bottom of the image where numerous surface streamlines merge, and ends with another negative bifurcation at a focus. The other bifurcation labeled E, is rendered at the top of the image. In this area, and in others where streamlines are not rendered, clear interpretation of the surface flow pattern is difficult due to the low shear stresses there. Therefore, the existence of bifurcation E is uncertain.

4.2 DPIV Data Analysis

Digital Particle Image Velocimetry (DPIV) studies were conducted in a vertical plane bisecting the in-line wheels. The data plane is shown in figure 2.8. Details of the data acquisition procedure and the equipment used are given in Section 2.2.3. Aspects of the interrogation procedure and software are provided in Section 2.2.4.

A group of 50 vector images, corresponding to each of the 160 data locations shown in figure 2.8, were averaged together, and used to construct the average velocity field in the data plane around the wheels. To eliminate the 4 mm overlap between data locations (see fig 2.8), the data was computationally resampled using the technique of Landreth & Adrian (1988) with a constant Gaussian kernal of 1.3. This also afforded a mild filtering to eliminate severe discontinuities, if they existed.

4.2.1 Velocity Field in DPIV Data Plane

Figure 4.21 shows the complete vector field in the DPIV data plane created by averaging the velocity vectors images at each data location. Streamlines are also plotted at selected locations. To enhance data visualization, the vector field is also imaged in figure 4.22 using Line Integral Convolution (LIC) (Cabral & Leedom, 1993). This technique clearly identifies streamline features and characterizes vector magnitude with color.

It is clear from the figures that the mean flow around the outside of the wheels is rather symmetric, including the separated region behind the aft wheel. Between the wheels, there is a mild asymmetry apparent on the front of the aft wheels, indicated by the locations of flow attachment along the stagnation streamlines. This asymmetry allows flow from the wing-side to penetrate further into the gap region. To quantify the degree of asymmetry, the data were analyzed in greater detail. This analysis shows that, on the wing-side, the flow attaches at -30 degrees, whereas on the ground-side, it attaches at 35 degrees. This 5 degree offset is believed to be associated with the formation of a vortex that rolls up between the wheels.

To gain an understanding of why this asymmetry occurs, the u-component velocity profiles on the wing- and ground-sides of the fore wheel, at ±90 degrees were extracted from the DPIV data. They are plotted together in figure 4.23. The plot shows there is a velocity defect on the wing-side of the wheel. This defect is expected to arise from obstruction of flow created by the center support strut. Figure 4.24 shows a plot of the pressure gradient around the fore wheel as a function of azimuthal location. The plot shows a less severe peak in the adverse pressure gradient on the wing-side of the wheel, than on the ground-side. It also shows the peak is shifted around the wheel to a greater azimuthal angle. These two factors are associated with the flow to remaining attached about 5 degrees further around the wheel on the wing-side, as was noted in Section 4.1.1. This 5 degree difference in separation location on the fore wheel is believed to result in the flow asymmetry on the aft wheel.

Returning to the surface streamline and pressure data in figures 4.13 and 4.14, direct comparison can be made between these surface data and the velocity data of figures 4.21 and 4.22. In figure 4.13 red lettering highlights the attachment node and a separation saddle on the backside of the fore wheel. These two features are associated with the vortex in that location. Figure 4.13 shows the attachment nodes on the front of the aft wheel. Also highlighted are the saddles-of-separation that identify the region from which flow leaves the surface of the aft wheel and is entrained into vortex between the wheels.

4.2.2 Vorticity Field in DPIV Data Plane

Vorticity in the same plane as the aforementioned velocity was calculated using the definition of circulation and Stokes theorem. Color coded contours are plotted in figure 4.25. The expected positive and negative boundary layer vorticity on the bottom and top surfaces of each wheel is readily apparent. The onset of shedding boundary layer vorticity on the aft wheel is highlighted in the figure as the beginning of flow separation.

Figure 4.26 is a magnification of the vorticity field between the wheels. On the ground-side of the fore wheel, there exists a region of unstable vorticity, which is apparent by its discontinuous nature. This vorticity is postulated to feed into the vortex that persists between the wheels, highlighted at a location further downstream. Sites of flow separation and attachment, are readily apparent on both wheels, and are identified by adjoining regions of positive and negative vorticity. Referring back to the oil flow image of figure 4.12, a distinct line of separation is apparent on the wing-side of the fore wheel, beginning at a saddle point. Yet here in figure 4.26, we see a continuous region of attached positive vorticity extending from the wing-side of the fore wheel, around the backside, to about 200 degrees. This suggests that the extent of separation in this region is minimal, with the flow remaining close to the wheel surface, and reattaching a short distance downstream. Further evidence is provided in figure 4.12 where the positive bifurcation highlights flow attachment on the backside of the fore wheel.

Figures 4.21 and 4.22, show the mean flow state of the vortex pattern that exists between the fore and aft wheels; the vortex is located directly behind the fore wheel. There is evidence, however, that more than one mean flow state exists in this region. When assembling the velocity vector field in the DPIV data plane, averaged vector images in certain locations, highlighted by the magenta boxes in figure 4.21, did not match the surrounding pattern. For these locations, the available images were qualitatively reviewed, and grouped according to perceptible pattern. From these pattern groups, 50 images were then averaged and used to complete the composite. This suggests that flow characteristics are not stable in this region.

This initiated an expeditious look at the dynamic flow characteristics on the backside of the fore wheel using fluorescent mono-filament mini-tufts. Each tuft was cut to a length of 10 mm and attached to the wheel on a 13- x 13-mm grid. The tuft material had a diameter of 33 microns and was made highly visible with ultraviolet lighting. Video recordings of the tuft activity identified two mean flow states. In the first, and most persistent state, tuft features suggested flow remained attached to the ground-side of the fore wheel, until it encountered flow from the wing-side. At this location flow separation occurred. The separation location identified with the tufts coincides with the critical line associated with the saddle, highlighted with red lettering in figure 4.13. This location is also marked as a flow separation location on the backside of the fore wheel in figures 4.21, 4.22, and 4.26. In the second mean state, tuft activity suggested massive separation along the location marked "unstable vorticity layer" in figure 4.26. In other locations, tuft activity remained relatively unaltered.

It is hypothesized that the state of separation on the backside of the fore wheel correlates with the state of recirculation on the ground-side of the same wheel. Recall, from Section 4.1.1, that an upstream and downstream recirculation region were apparent in the oil flow topology, and that evidence suggested the trailing boundary of the downstream region erratically changed from a saddle-of-attachment to a saddle-of-separation. It is postulated that the second mean state between the wheels, evidenced by massive separation behind the ground-side of the fore wheel, exists when the downstream recirculation region on that side of the wheel, terminates with a saddle-of-separation. This is supported by the observation that the trailing end of the downstream recirculation (fig 4.10) coincides with the beginning of the unstable vorticity layer (fig 4.26) at 113 degrees around the wheel from the leading edge.

In other words, the first mean flow state, shown in figure 4.11a, occurs when the downstream recirculation region terminates with a saddle-of-attachment and the flow immediately downstream is attached; this flow eventually separates along the critical line, highlighted in figure 4.10. In the second mean flow state, the downstream recirculation region terminates with a saddle-of-separation (fig 4.11b), inducing a massive separated flow state behind the ground-side of the fore wheel. Recall, also, from Section 3.2, that there was evidence during the particle path studies that separation characteristics on the wing- and ground-sides of the fore wheel greatly affect the mean flow characteristics between the wheels.

Given the changing state of separation from behind the fore wheel, as described above, consideration must be given to what effect this will have on other flow features between the wheels; specifically its effect on the persistence of the vortex between the wheels is of interest. Figure 4.27 shows images of averaged velocity vectors for DPIV data locations 23, 24, and 25 between the wheels (refer to figure 2.8 for a broader view of these locations). Each averaged image was formed using 50 images acquired consecutively at a 5 Hz sample rate. In other words, no pattern recognition was used to collect the 50 images used in the averaged sets. The figure shows how the vortex between the wheels shift location from directly behind the fore wheel, to directly in front of the aft wheel. This is expected to result from changing separation characteristics on the backside of the fore wheel. Figure 4.27a represents the first, and primary mean flow state, with the vortex positioned behind the fore wheel. As the flow state changes, the vortex progresses downstream (fig 4.27b), to finally reside in front of the aft wheel just below the attachment node (fig 4.27c). It is expected to remain there until the flow state changes again.

4.3 Concluding Remarks

Oil flow and mean surface static pressure data were acquired on a fore and aft wheel of a 31% scale model of a 4-wheel landing gear bogie. DPIV data were also acquired in a plane bisecting the in-line wheels of the model. Tests were conducted in the BART wind tunnel at a Reynolds number based on wheel diameter of 600,000.

For the first time, the complex features of separation and attachment on a tandem wheel arrangement of a landing gear bogie have been defined in terms of the fundamental topological patterns found in the literature for cases of single bodies and surfaces. These patterns are illustrated in figure 4.1, and in the present study they were identified in isolation and in combination. Past work has shown that surface shear-stress lines produced in oil flow experiments are closely linked to surface streamlines. With this understanding, near-surface flow features associated with the surface streamline patterns have been inferred in the present study using the diagnostic logic of previous authors. In addition to the surface streamline patterns, the present study also employs distributions of the mean surface static pressure as an aid in flow feature identification. Furthermore, DPIV results have been employed to elucidate the off-surface mean flow features and states, which would otherwise be indiscernible.

Despite the unusually complex nature of separation and attachment patterns occurring on the present configuration, it is demonstrated that basic topologies can be defined. All of the basic patterns illustrated in figure 4.1 were observed, except the stable node, which is associated with separation, and the unstable focus, which is associated with attachment. These findings are in accord with those of previous investigations of simpler geometries involving isolated bodies and surfaces.

While various combinations of topological patterns are addressed in the literature, some found in the present study are not. They include:

(i) The combination of separation saddles found on the upstream end of the aft wheel shown in figure 4.14.

(ii) The combination of separation and attachment lines on the ground-side face of the fore wheel seen in figure 4.10. The features of this combination are expected to change erratically as flow characteristics were observed to change during testing.

(iii) The change in flow direction along the critical line associated with the saddle-of-attachment seen on the fore wheel in figures 4.8 and 4.9. This direction change initiated positive bifurcations.

(iv) The asymmetry resulting from the one sided merging of the critical lines associated with the saddle-of-separation and the saddle-of-attachment at the juncture of the axle with the aft wheel.

Combinations and variations of the basic topological patterns found in the present study that are addressed in the literature include:

(i) The pairing of separation and attachment lines in the formation of a separation bubble. These lines can be paired as the critical line of a saddle-of-separation followed by the critical line of saddle-of-attachment, or a negative bifurcation followed by a positive bifurcation. Examples can be seen on the inboard and outboard faces of both wheels, in figures 4.8, 4.9, 4.15, & 4.16.

(ii) A Werlé-Legendre separation, observed on the wing-side of the fore wheel in figure 4.12. This combination is documented by Hornung & Perry (1984) and incorporates a saddle-of-separation, a focus and a positive bifurcation.

(iii) Distorted saddles observed in combination at the juncture of the aft wheel with the axle, seen in figure 4.16. Perry & Chong (1987) discuss this sort of saddle, which is an aberration of a fundamental pattern. In the current study, the combination of distorted saddles consisted of a saddle-of-separation followed by a saddle-of-attachment and resulted in the formation of a vortex.

Insight into the flow field characteristics around the wheels was found in patterns of velocity, vorticity and streamlines obtained by using DPIV. Two stagnation locations on the front face of the aft wheel were found to exhibit an asymmetry of five degrees. This asymmetry is postulated to result from a corresponding five degree asymmetry in the separation locations on the wing- and ground-sides of the fore wheel. Differences in separation location on either side of the fore wheel are expected to result from differences in the location and magnitude of the peak in the azimuthal pressure gradient on the wheel, as shown in figure 4.24.

A vortex was found to persist between the in-line wheels. This vortex was also found to change position over a sufficiently long sampling time. This change in position is postulated to be linked to the erratically changing state of separation observed on the backside of the fore wheel. These changes in separation state are expected to shift the position of the vortex from directly behind the fore wheel to directly in front of the aft wheel.

Potential noise sources involve all regions that are adjacent to an unsteady flow. Especially significant are regions of unsteady flow attachment and separation. These regions and the associated flow features are listed below.

(i) The junctures of the of the axles and fore and aft wheels where turbulent flow winds up into a vortex. Here turbulent eddies are constantly impinging upon the surfaces of wheels and axles as they rotate within the vortex.

(ii) The backside of the fore wheel where turbulent flow attachment occurs along a positive bifurcation and at a node.

(iii) The downstream edges of the inboard and outboard faces on the fore wheel which shed an unsteady wake.

(iv) The ground-side of the fore wheel , where the process of flow separation exhibits erratically changing characteristics.

(v) The upstream face and inboard and outboard sides of the aft wheel which encounter turbulent eddies in the wake of the fore wheel.

(vi) The entire backside of the aft wheel which sheds a turbulent wake.

(vii) The ground-side region between the in-line wheels where a quasi-stationary vortex exists. This vortex may induce noise in two ways. The first is direct interaction with the surface of the wheel, and the second is its change in location between the wheels.

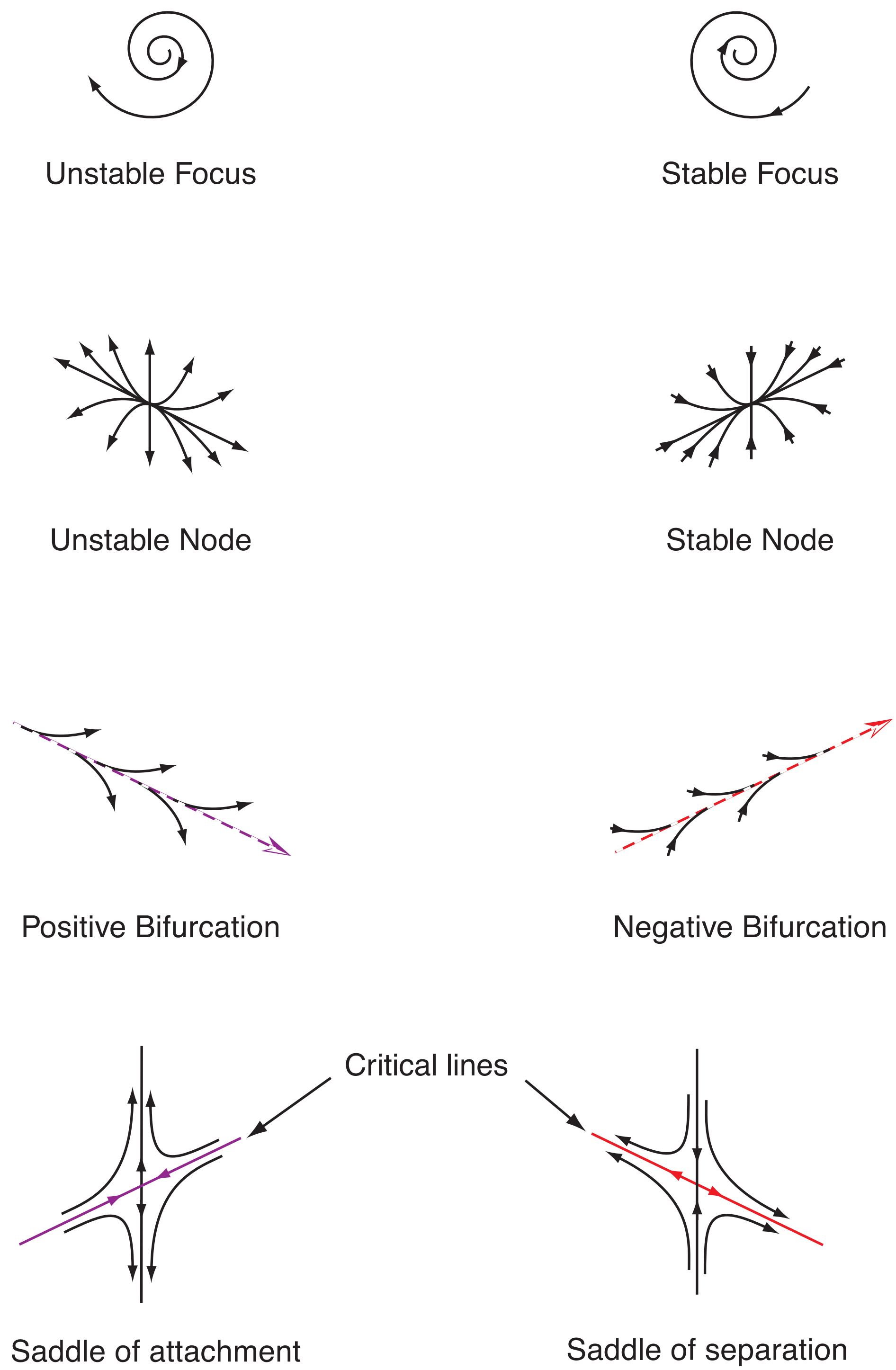

Figure 4.1 Frequently observed topological patterns.

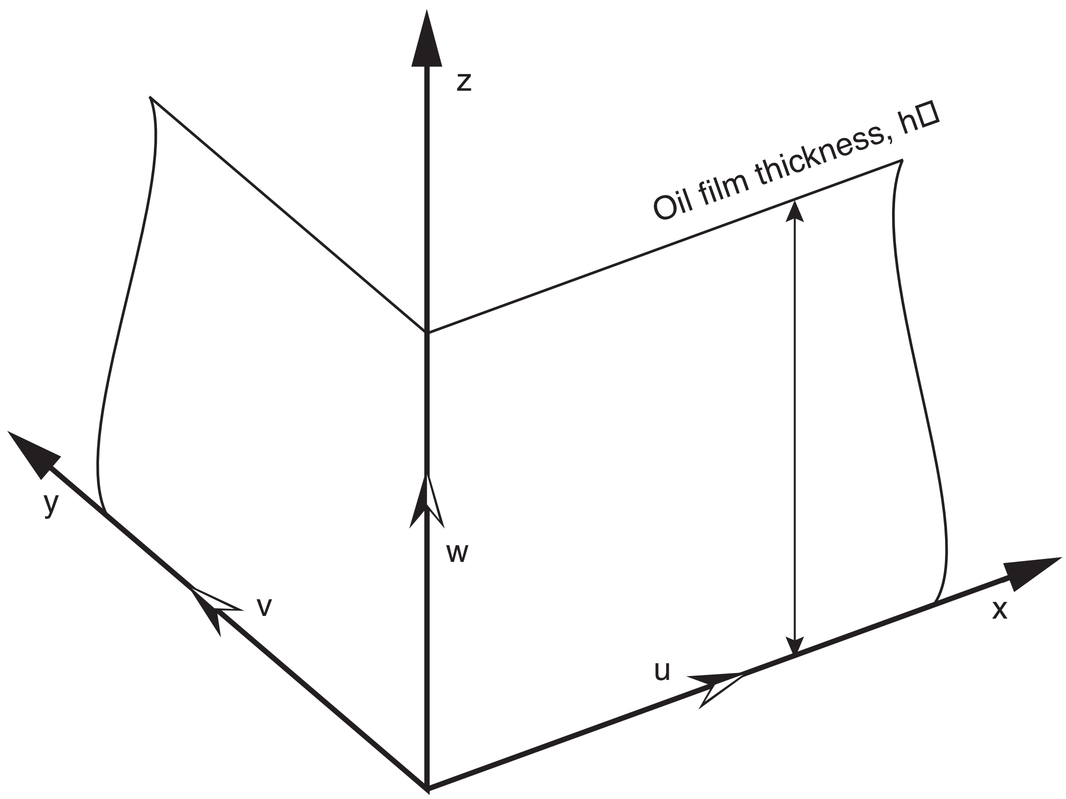

Figure 4.2 Coordinate system used to compare shear-stress lines with surface streamlines.

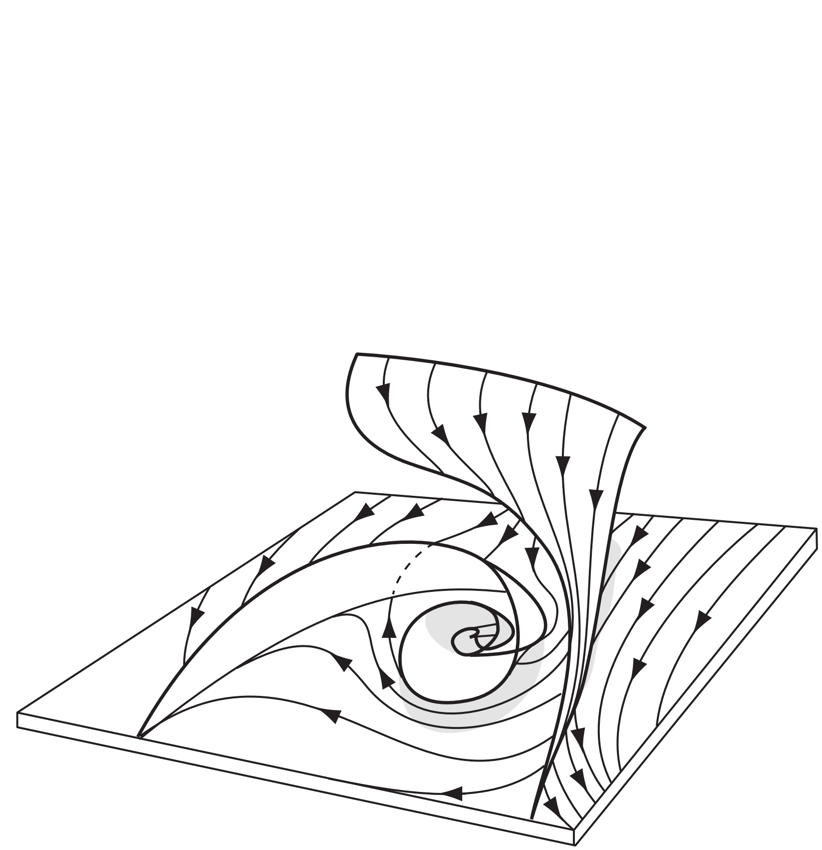

(a) (b)

Figure 4.3 Werlé-Legendre separation (Hornung & Perry, 1984) (a) Surface streamline signature (b) Inferred perspective view.

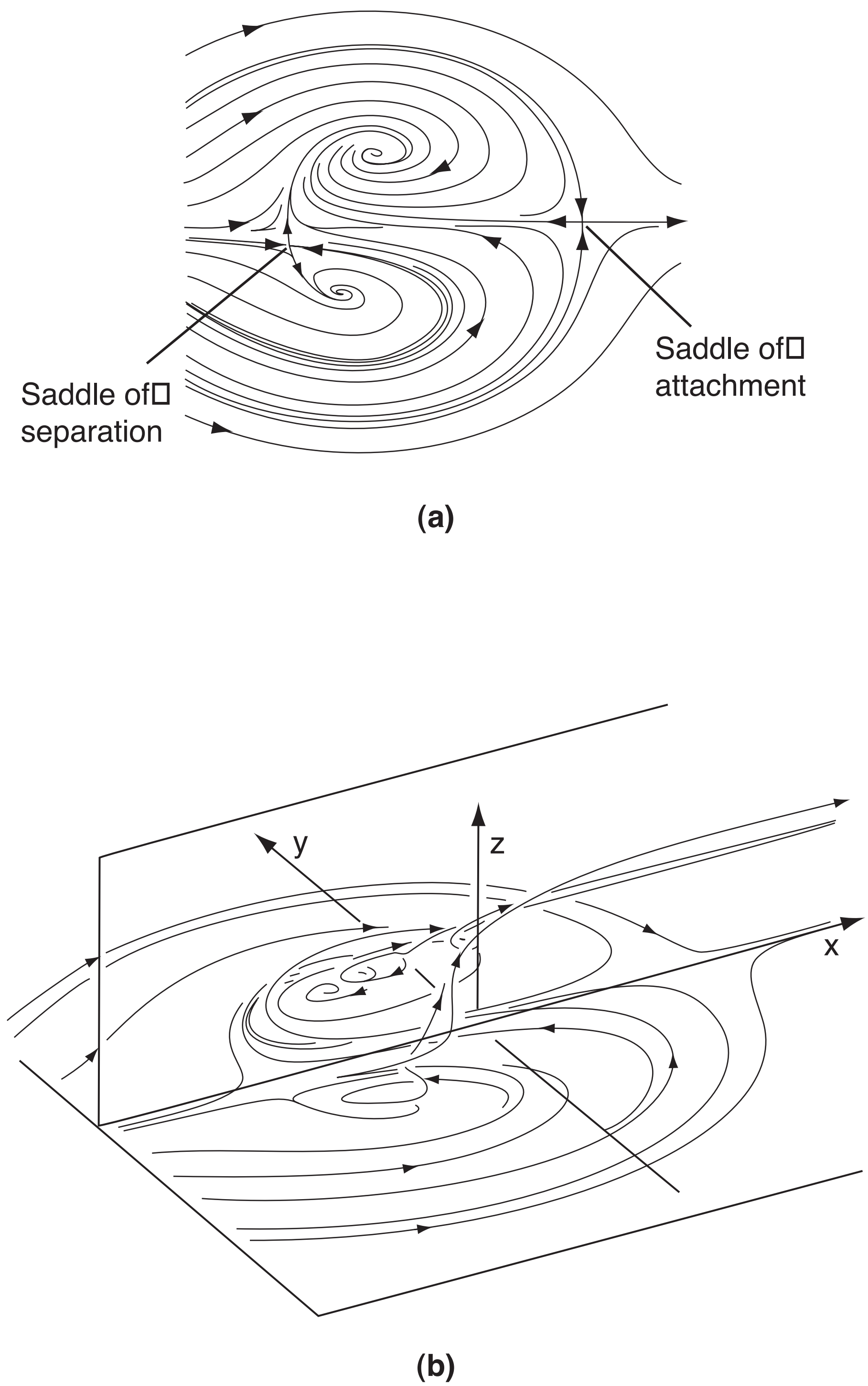

Figure 4.4 Offset separation and attachment calculated by Chong & Perry (1986). (a) Surface streamline pattern. (b) Oblique view with some out-of-plane trajectories.

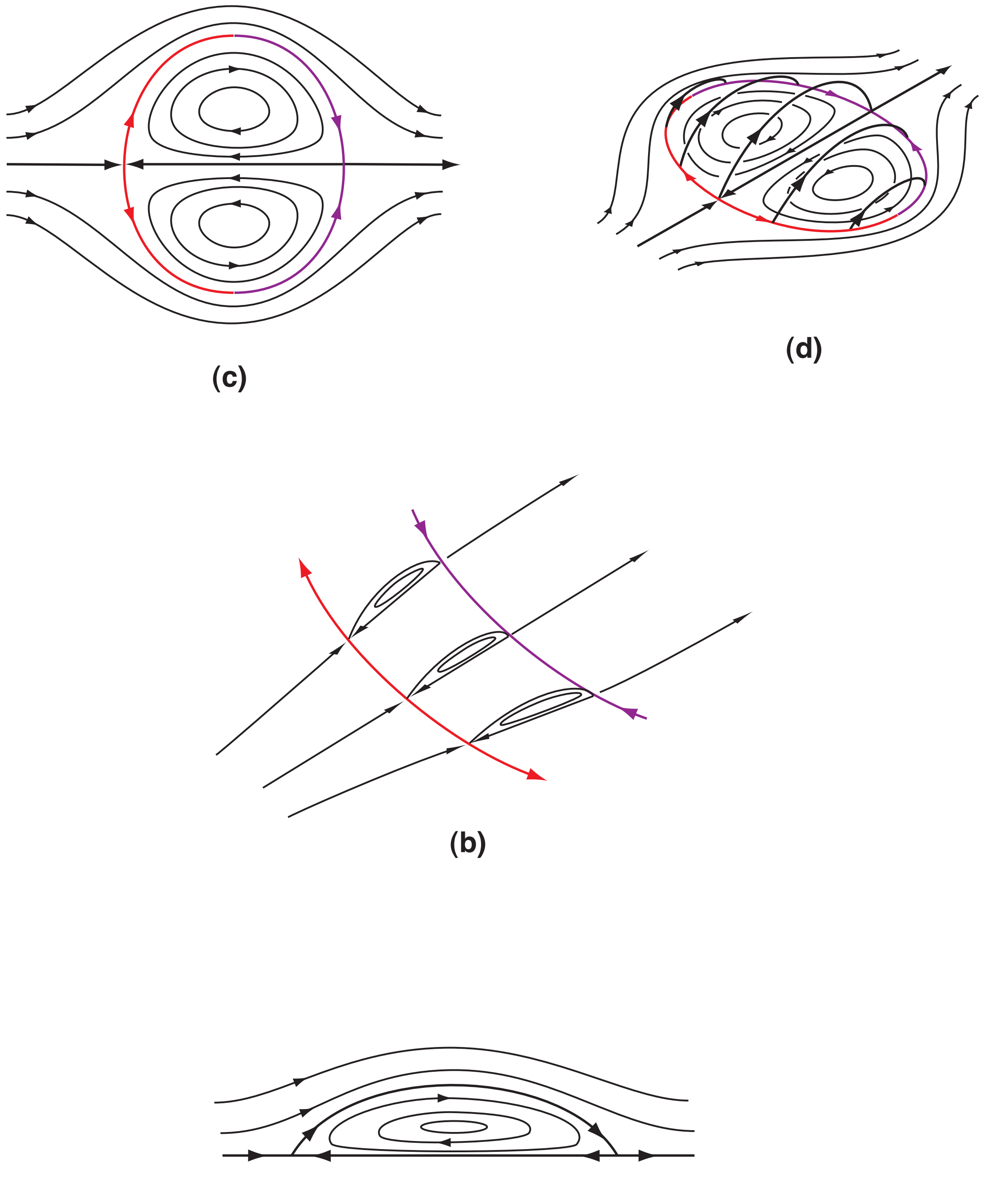

Figure 4.5 Recirculation and separation bubble definitions. (a) flow recirculation within a separation bubble (b) open ended separation bubble (c) surface streamline pattern of a recirculation zone (d) closed symmetric separation bubble. Red and purple lines represent respective separation and attachment critical lines.

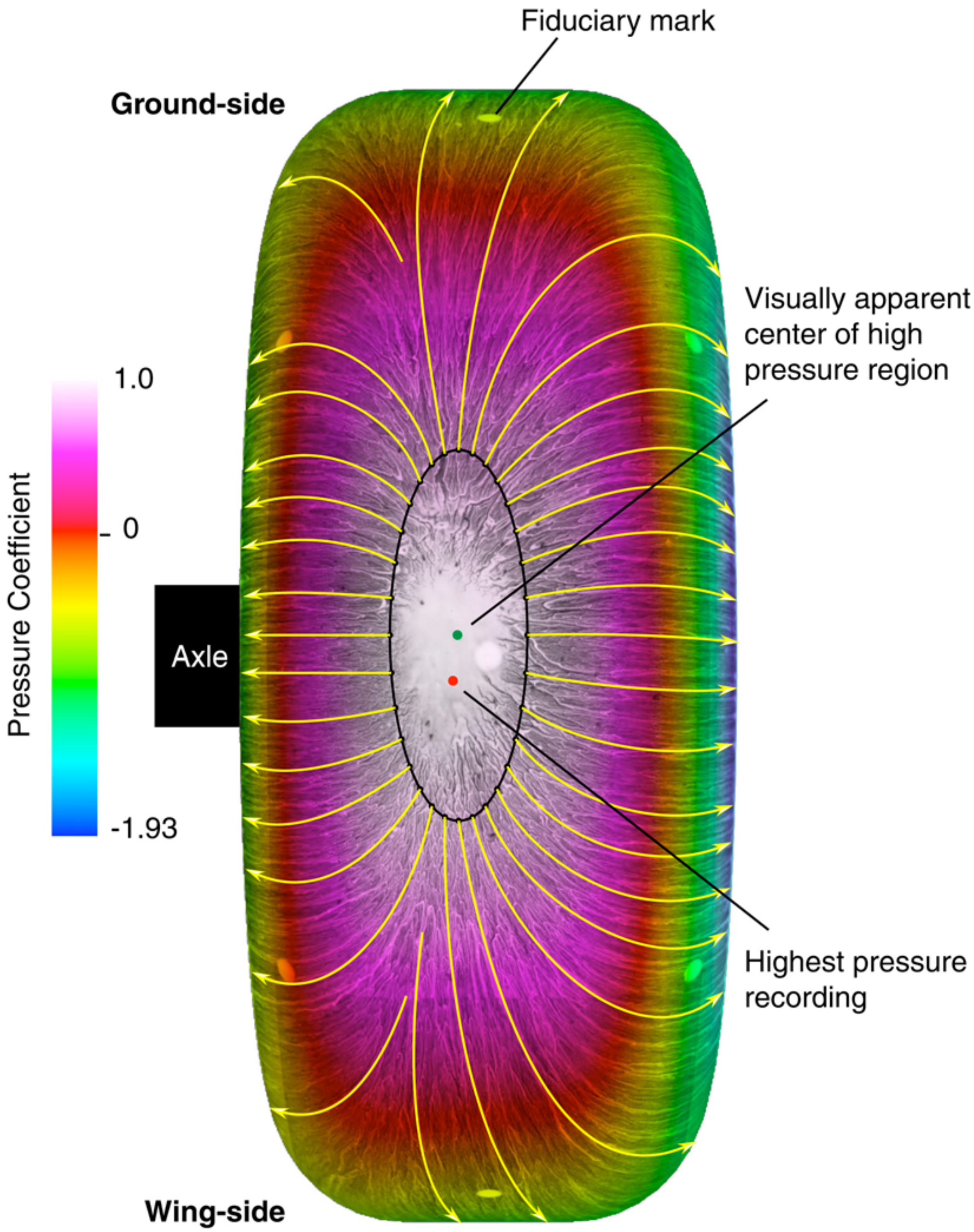

Figure 4.6 Pressure and shear stress data on front of fore wheel.

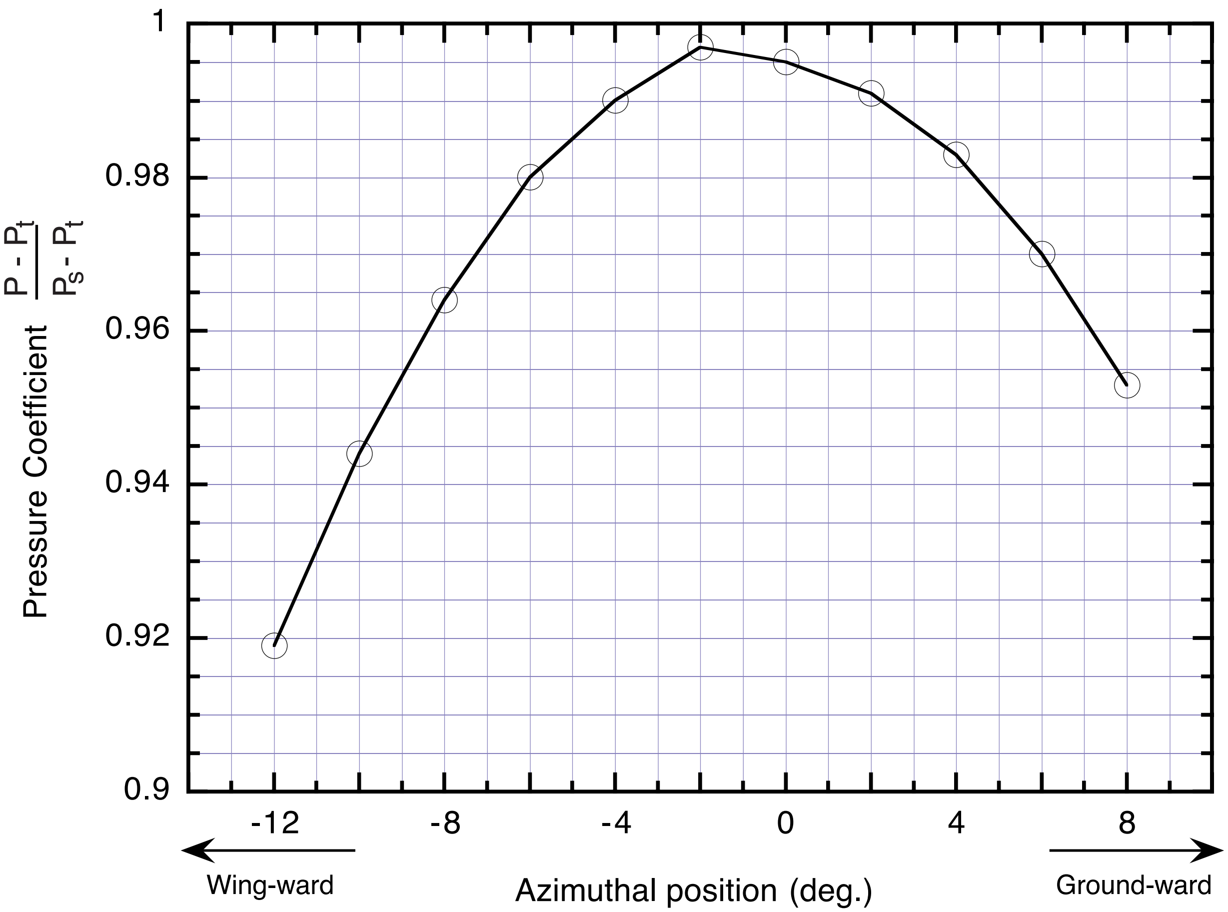

Figure 4.7 Azimuthal pressure variation on fore wheel

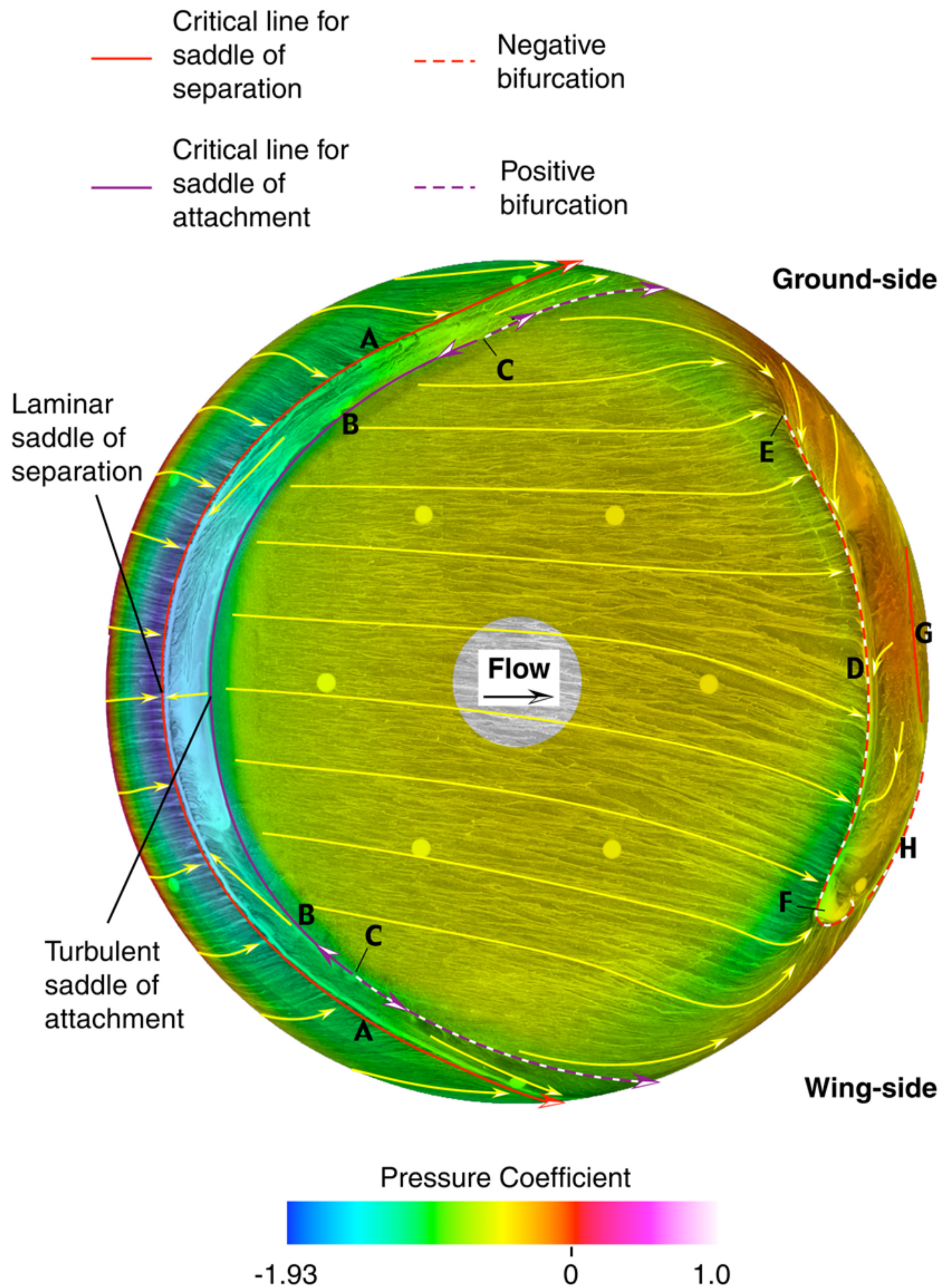

Figure 4.8 Pressure and shear stress data on outboard face of fore wheel.

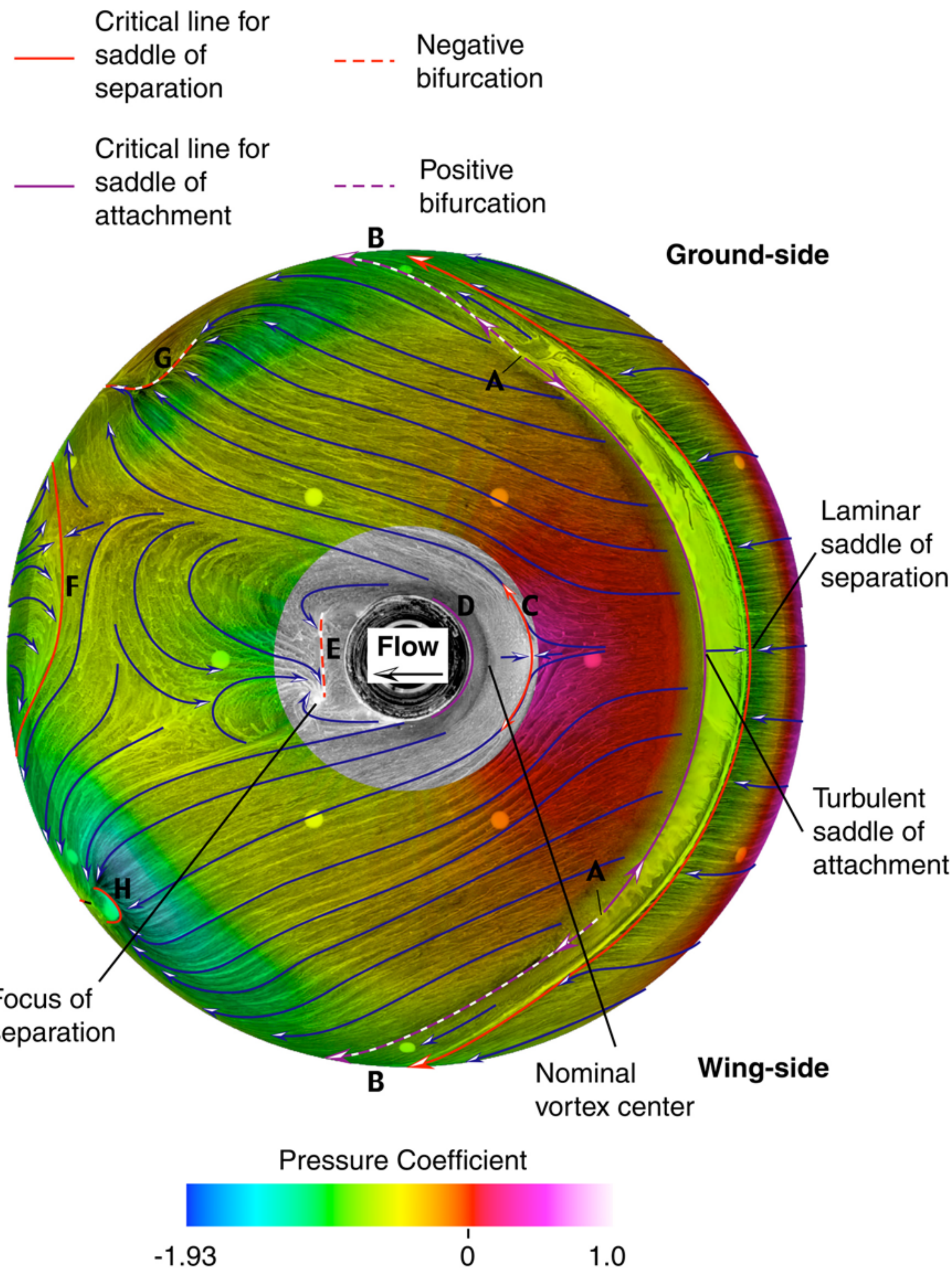

Figure 4.9 Pressure and shear stress data on inboard face of fore wheel.

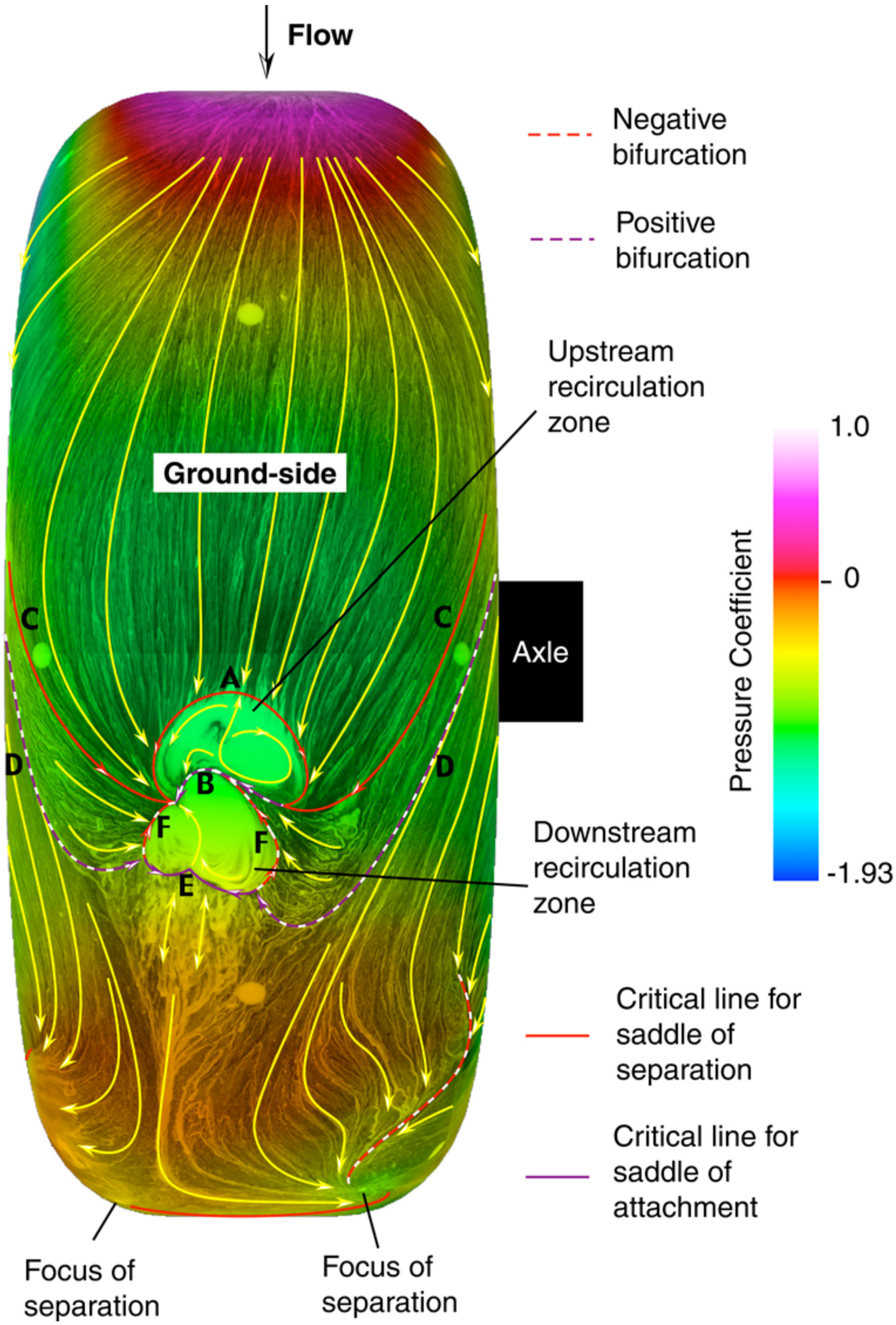

Figure 4.10 Pressure and shear stress data on ground-side of fore wheel.

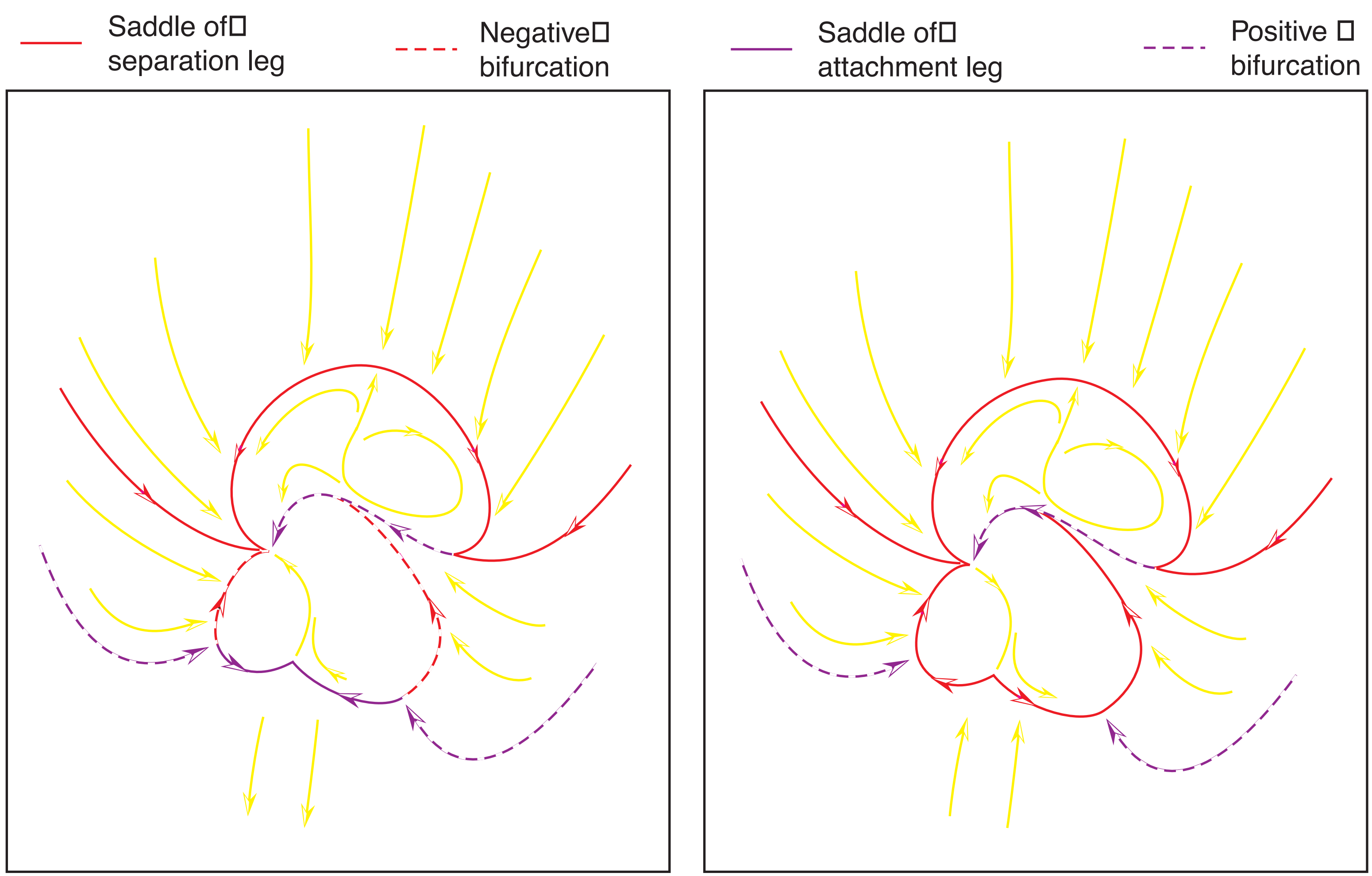

a) Primary recirculation - Trailing edge attached

b) Secondary recirculation - Trailing edge separated

Figure 4.11 States of primary and secondary recirculation on ground-side

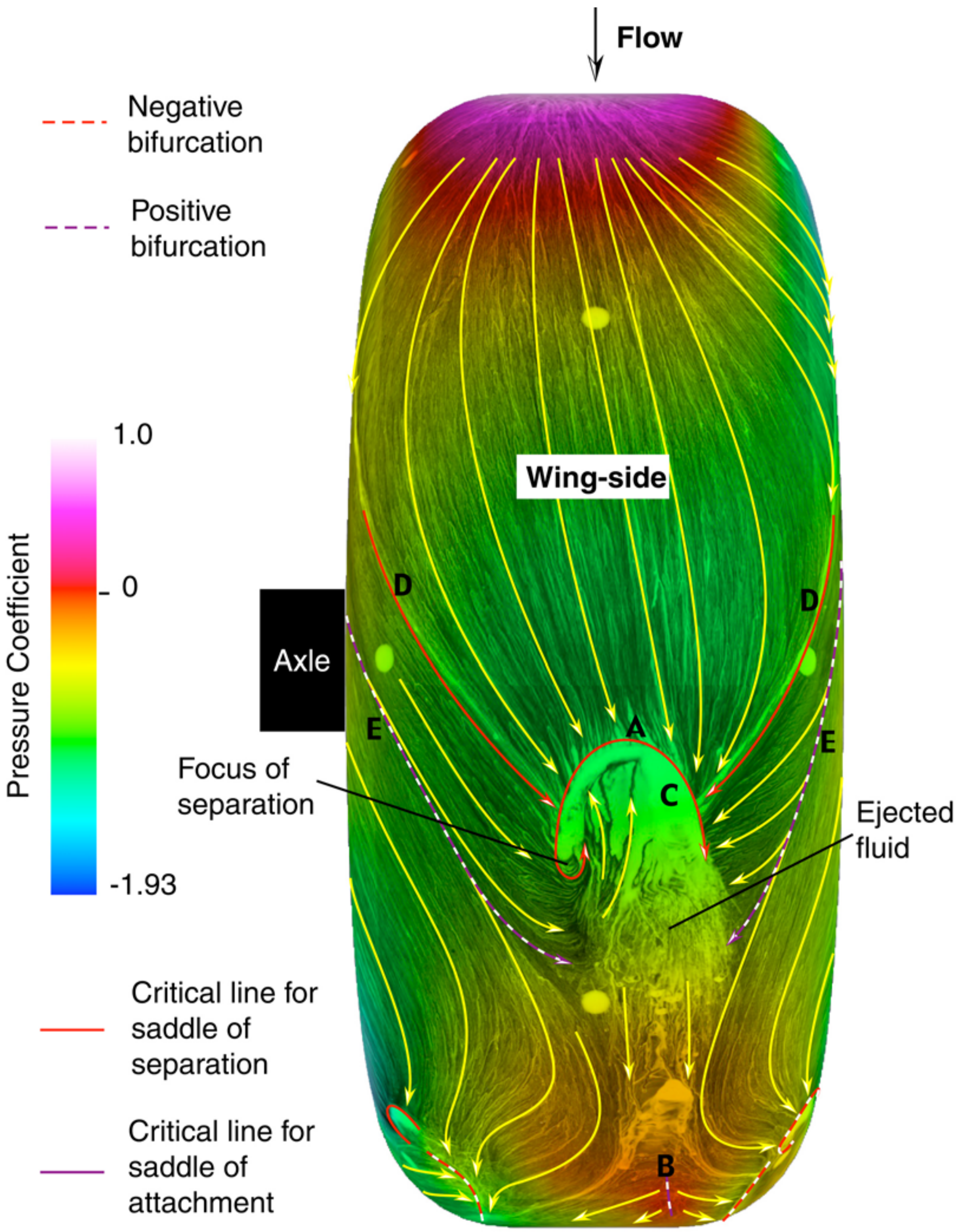

Figure 4.12 Pressure and shear stress data on wing-side of fore wheel.

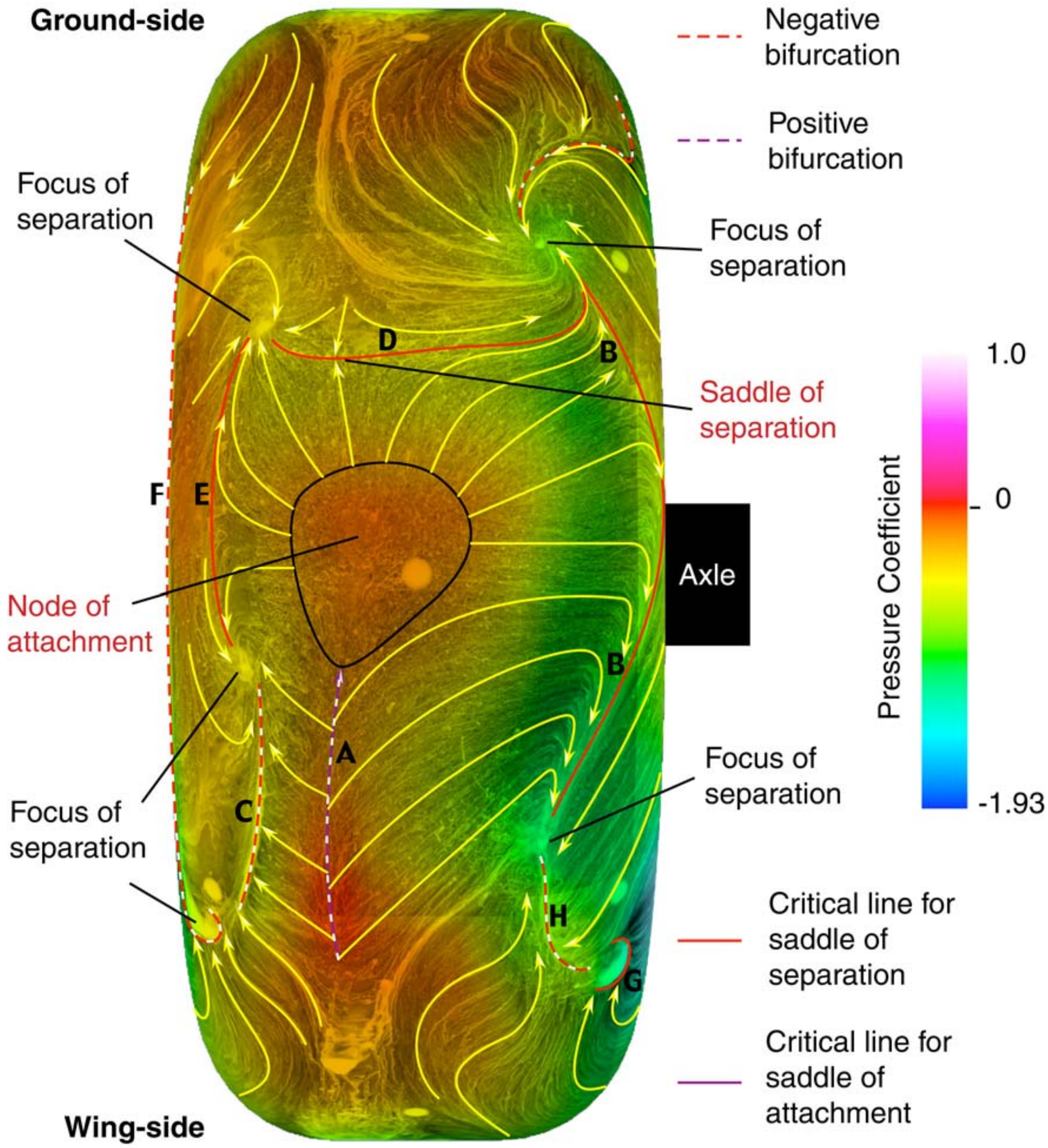

Figure 4.13 Pressure and shear stress data on backside of fore wheel.

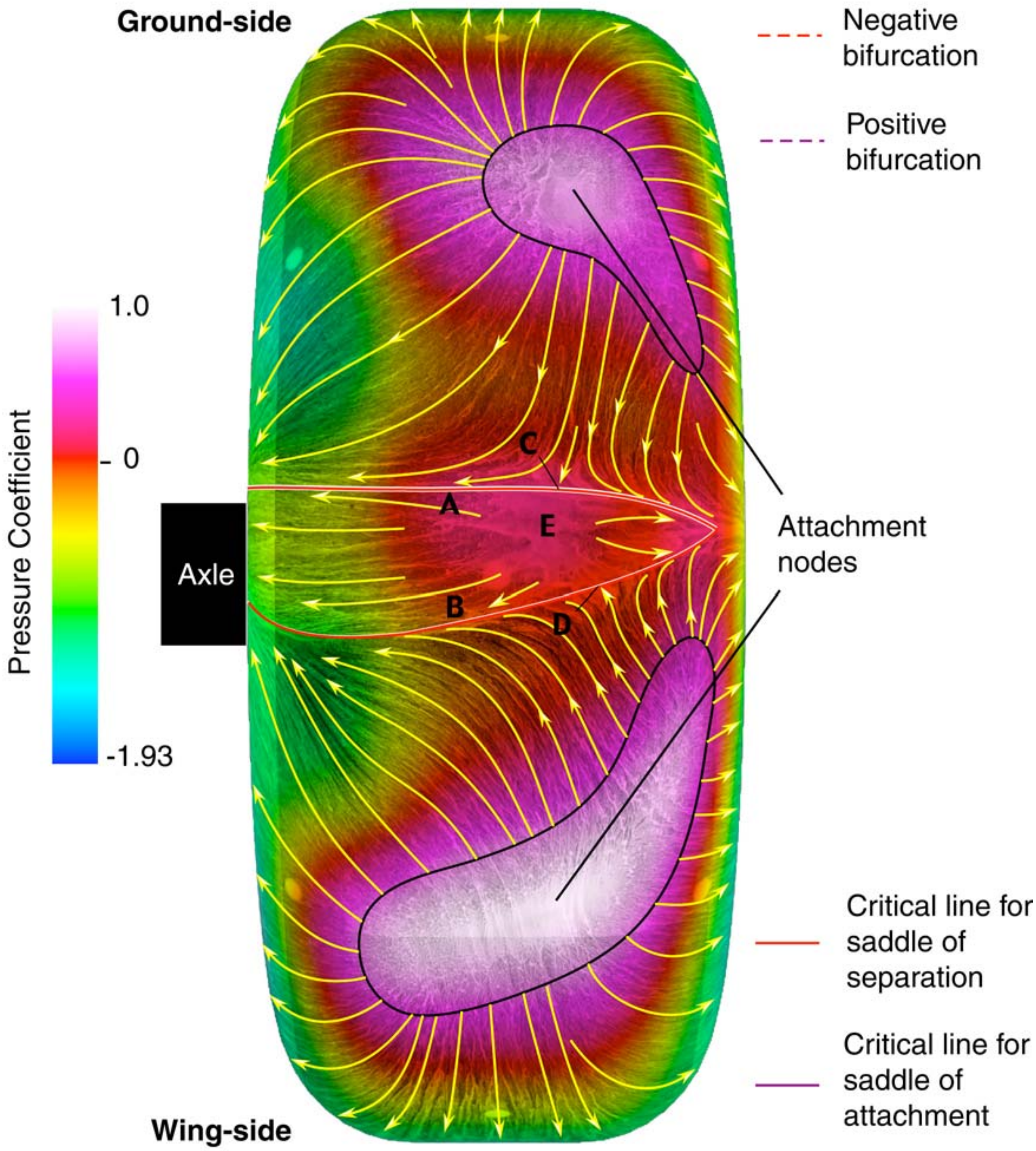

Figure 4.14 Pressure and shear stress data on front of aft wheel.

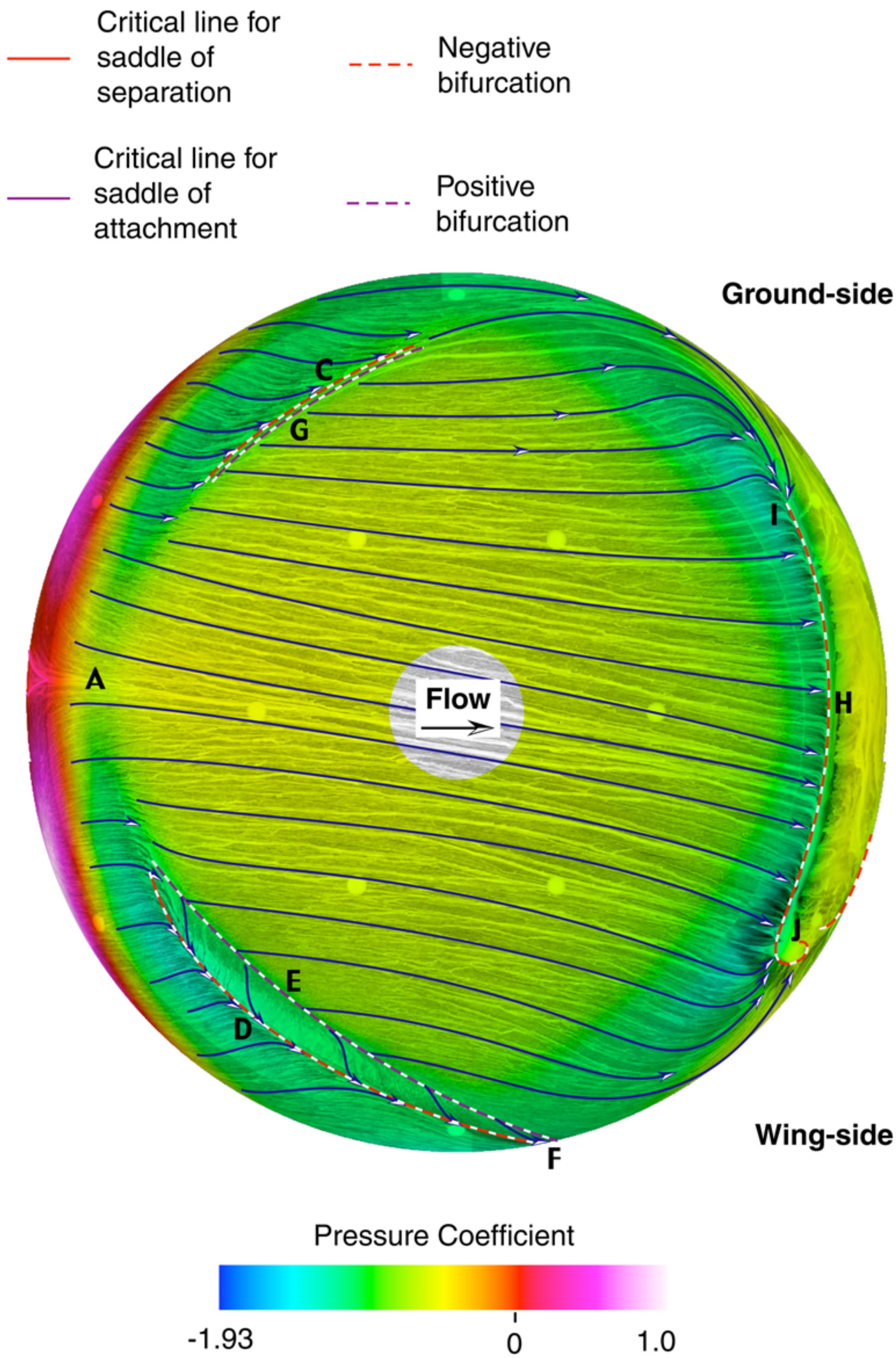

Figure 4.15 Pressure and shear stress data on outboard face of aft wheel.

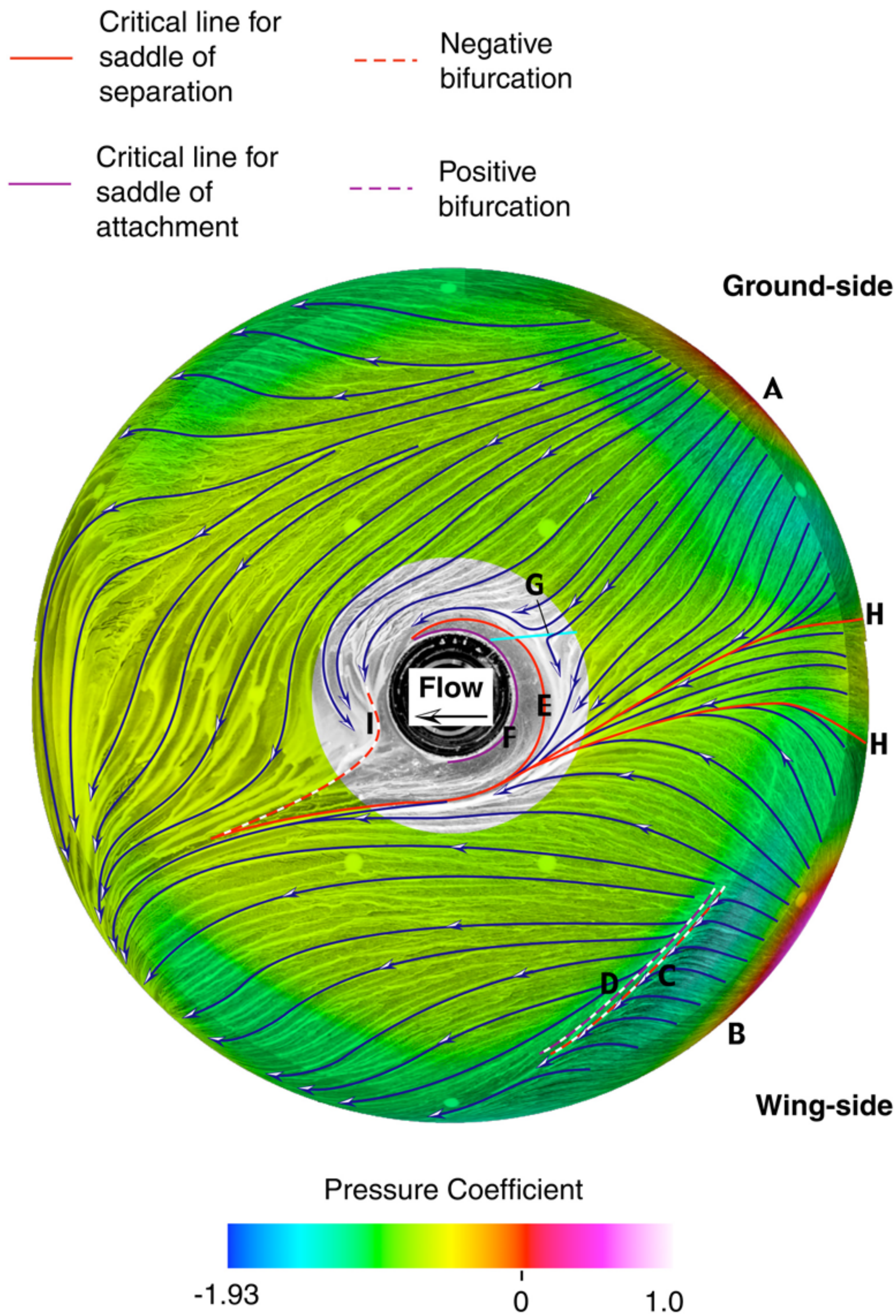

Figure 4.16 Pressure and shear stress data on inboard face of aft wheel.

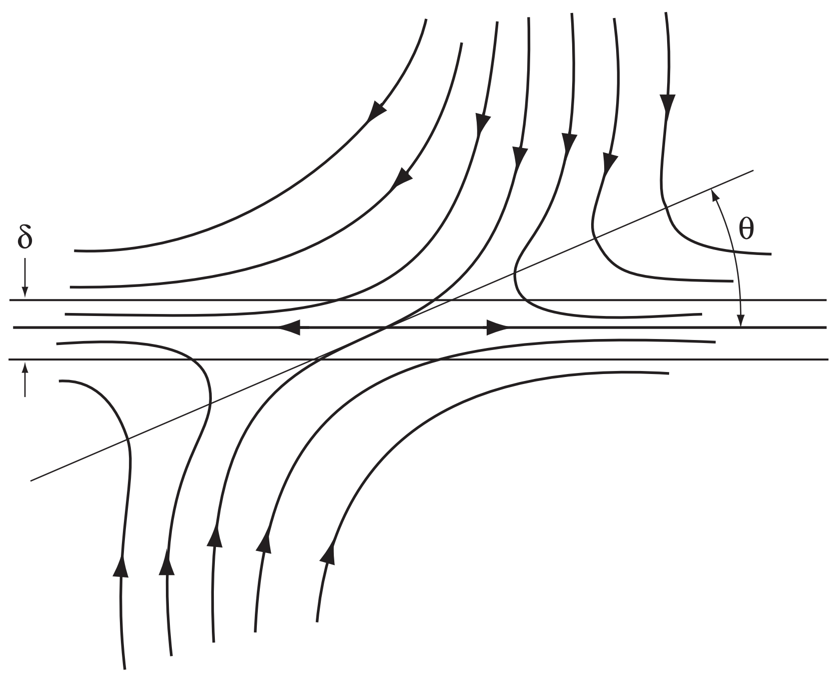

Figure 4.17 Dislocated saddle of finite-thickness (δ) shear layer. Here θ is the angle between the critical line and the tangent to the streamlines at the critical point. Taken from Perry & Chong (1987).

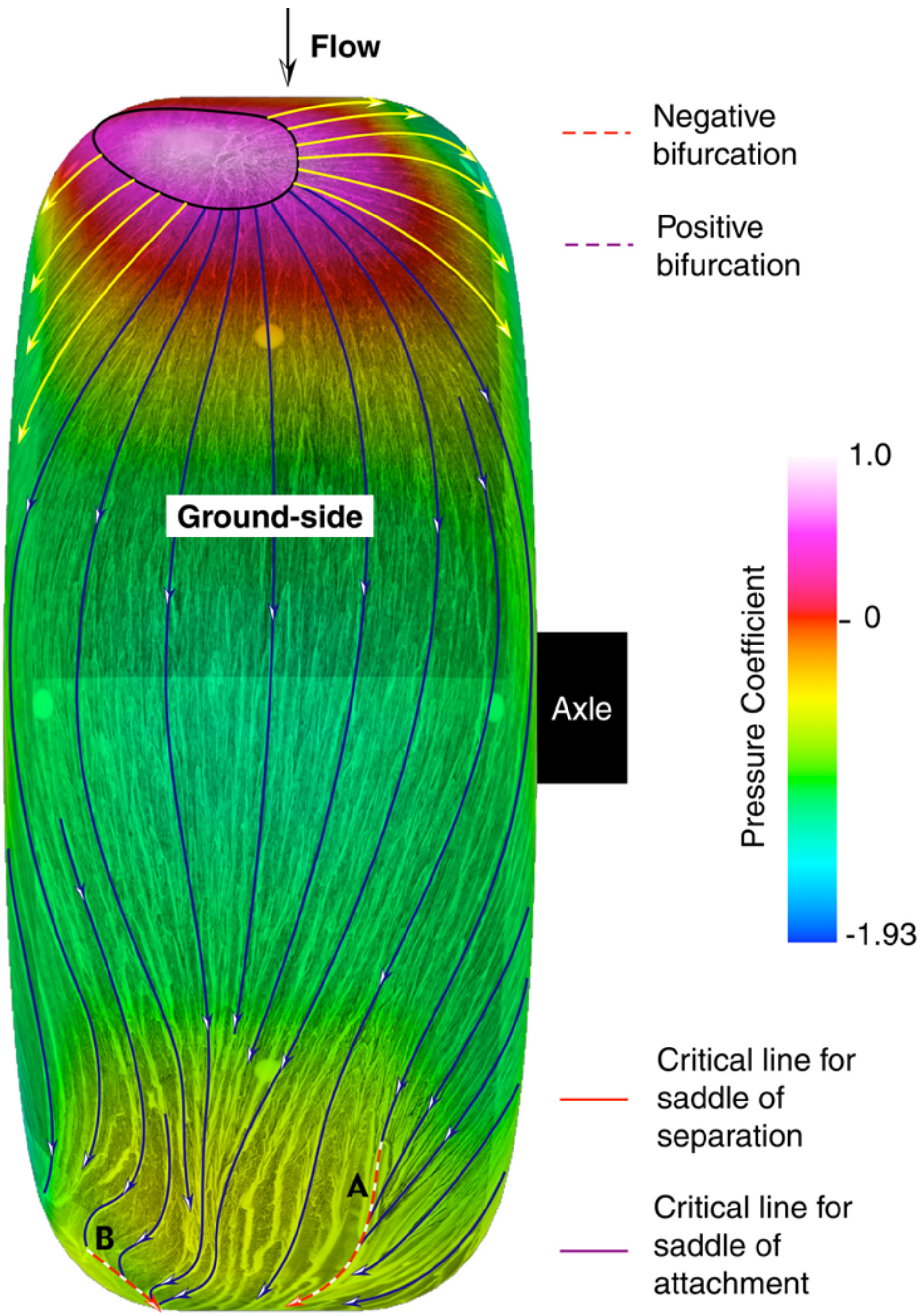

Figure 4.18 Pressure and shear stress data on ground-side of aft wheel.

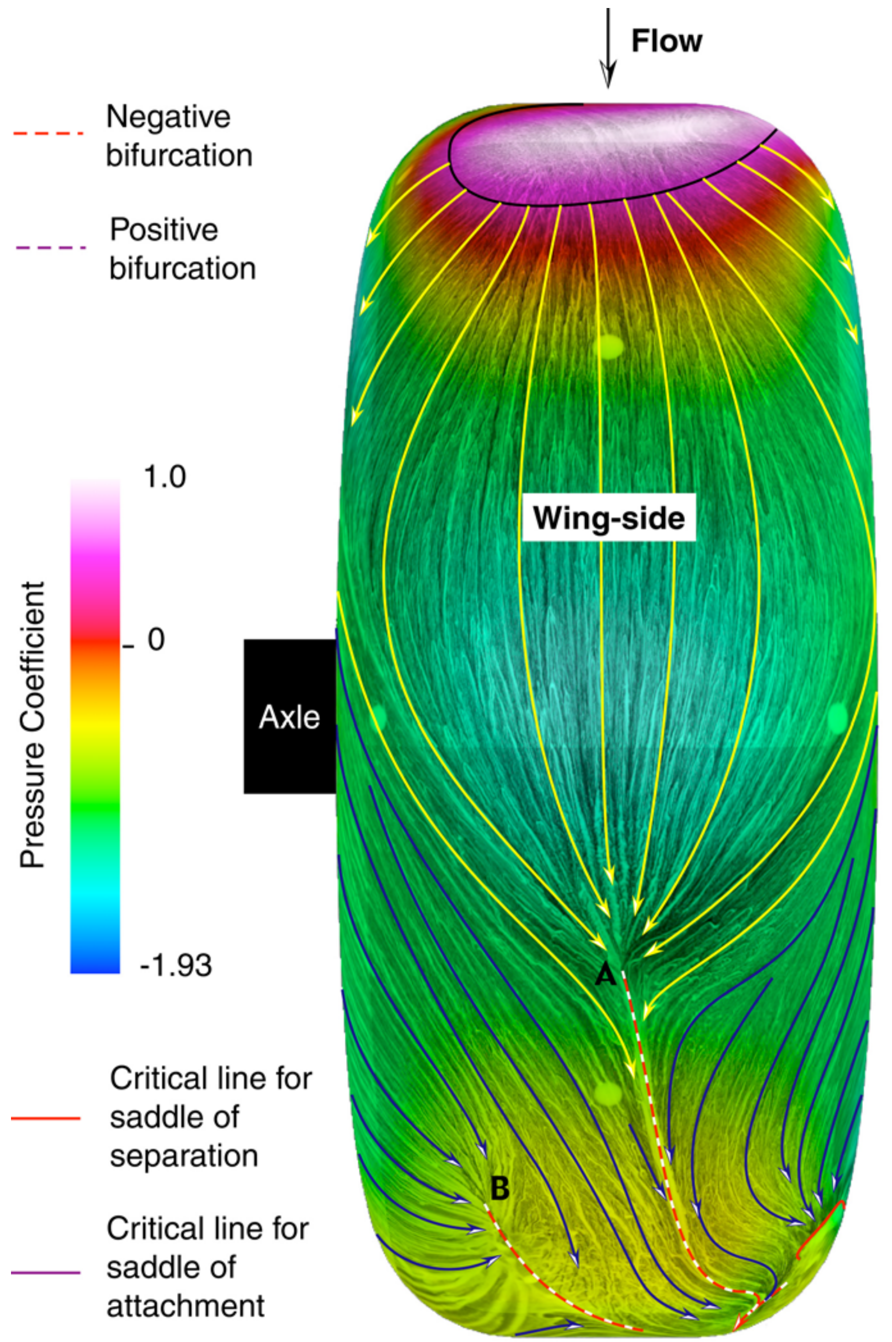

Figure 4.19 Pressure and shear stress data on wing-side of aft wheel.

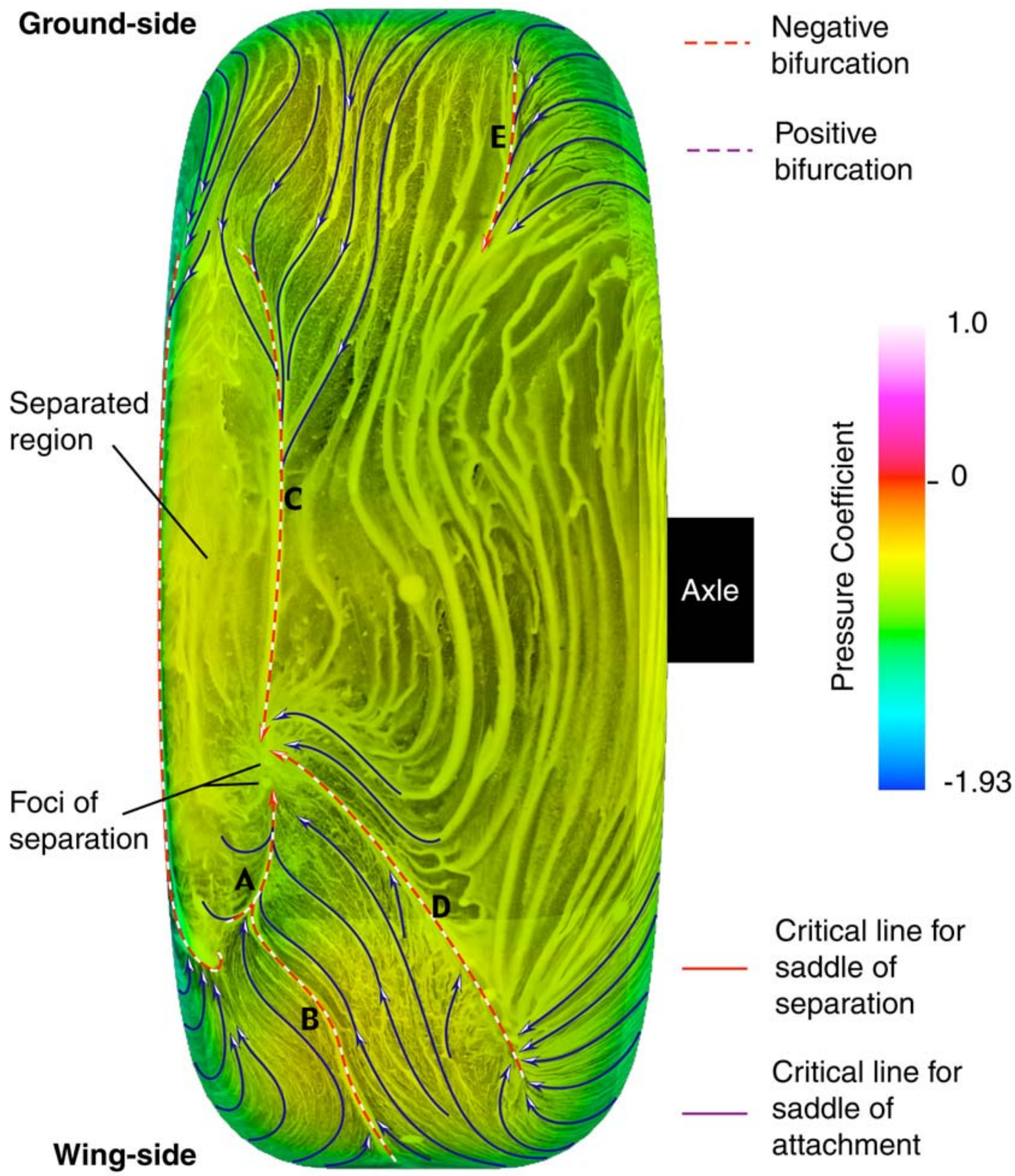

Figure 4.20 Pressure and shear stress data on backside of aft wheel.

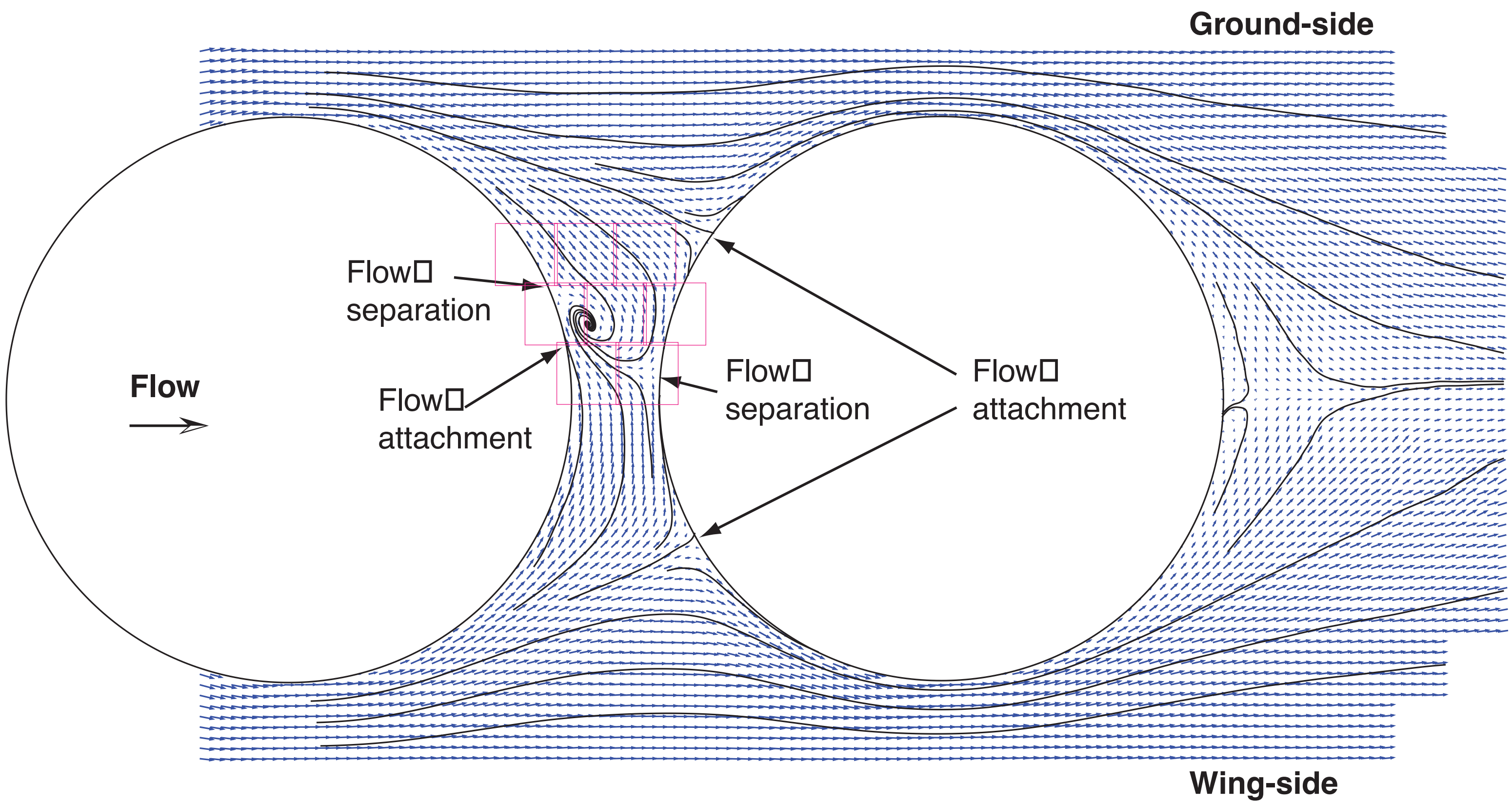

Figure 4.21 Velocity filed and streamlines in mid-plane of in-line wheels.

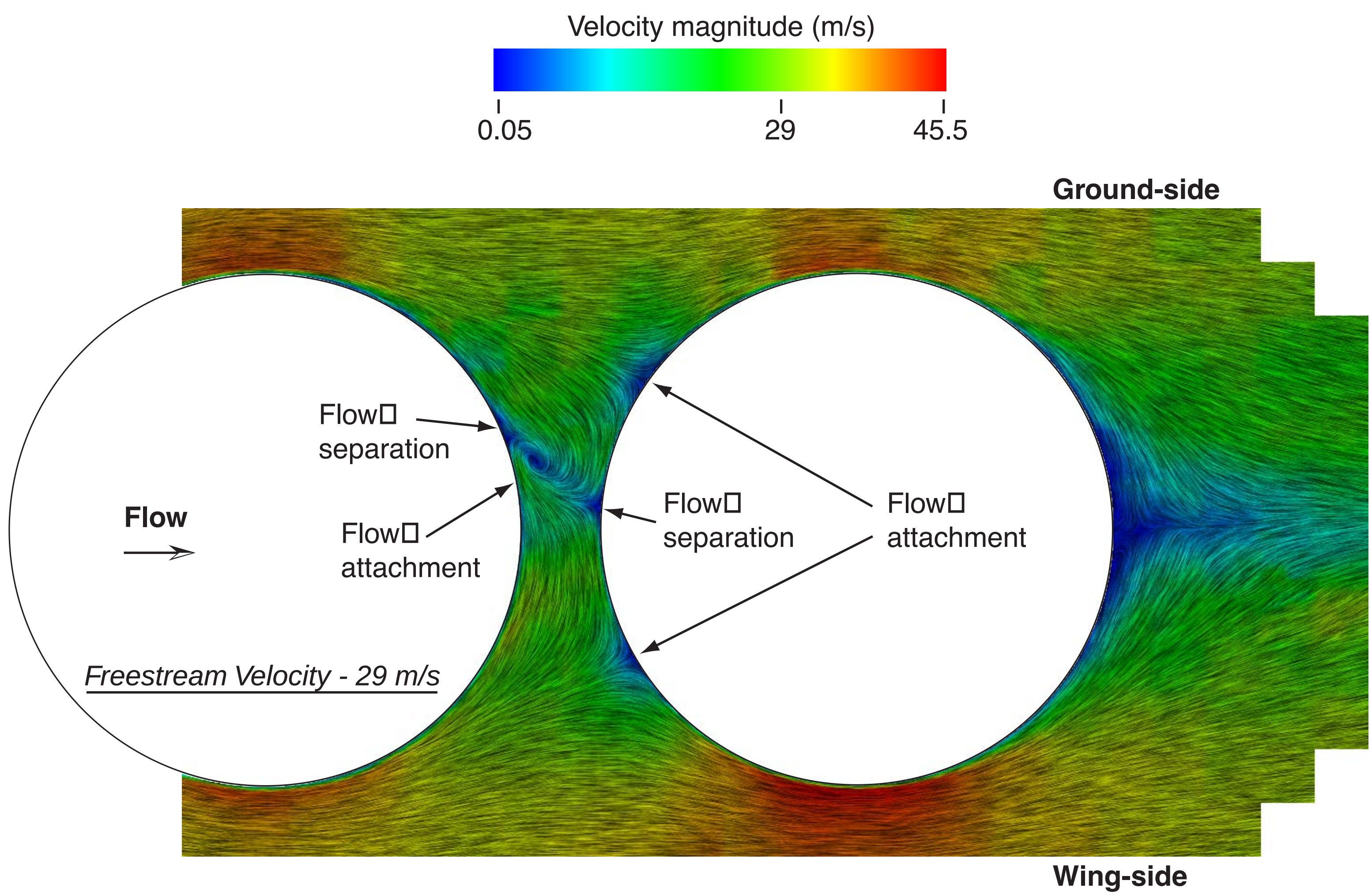

Figure 4.22 Line Integral convolution of velocity data showing streamlines and velocity magnitude.

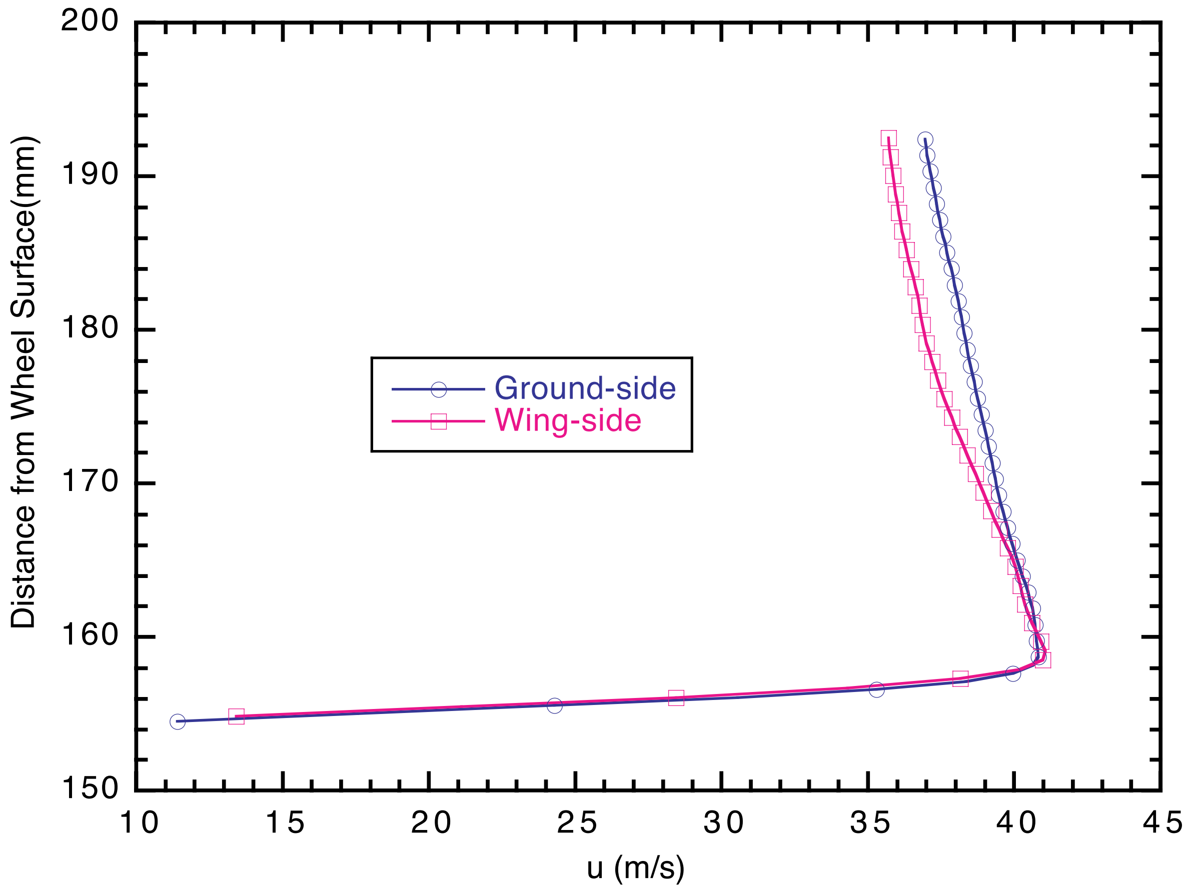

Figure 4.23 u-velocity component profiles on wing- and ground-sides of fore wheel.

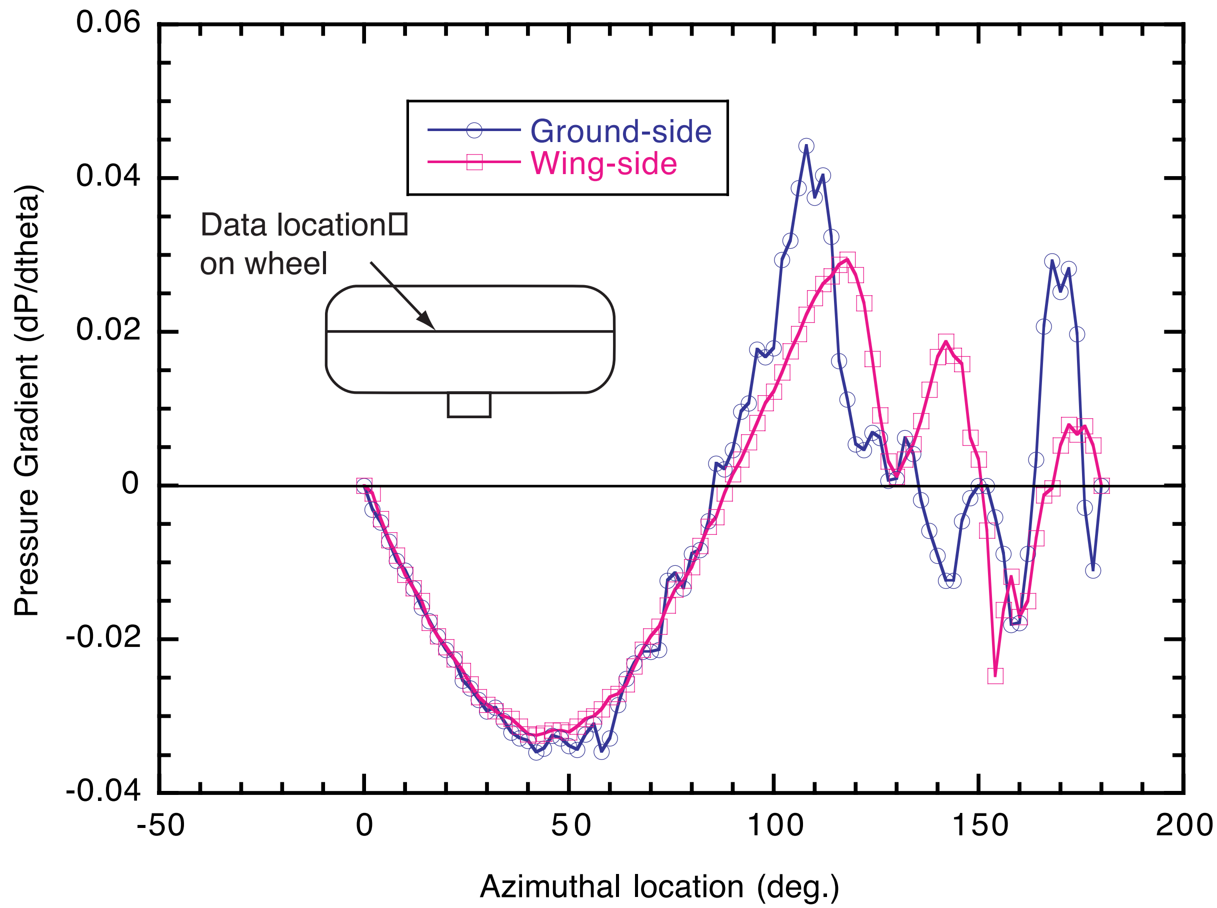

Figure 4.24 Pressure gradient on fore wheel tread.

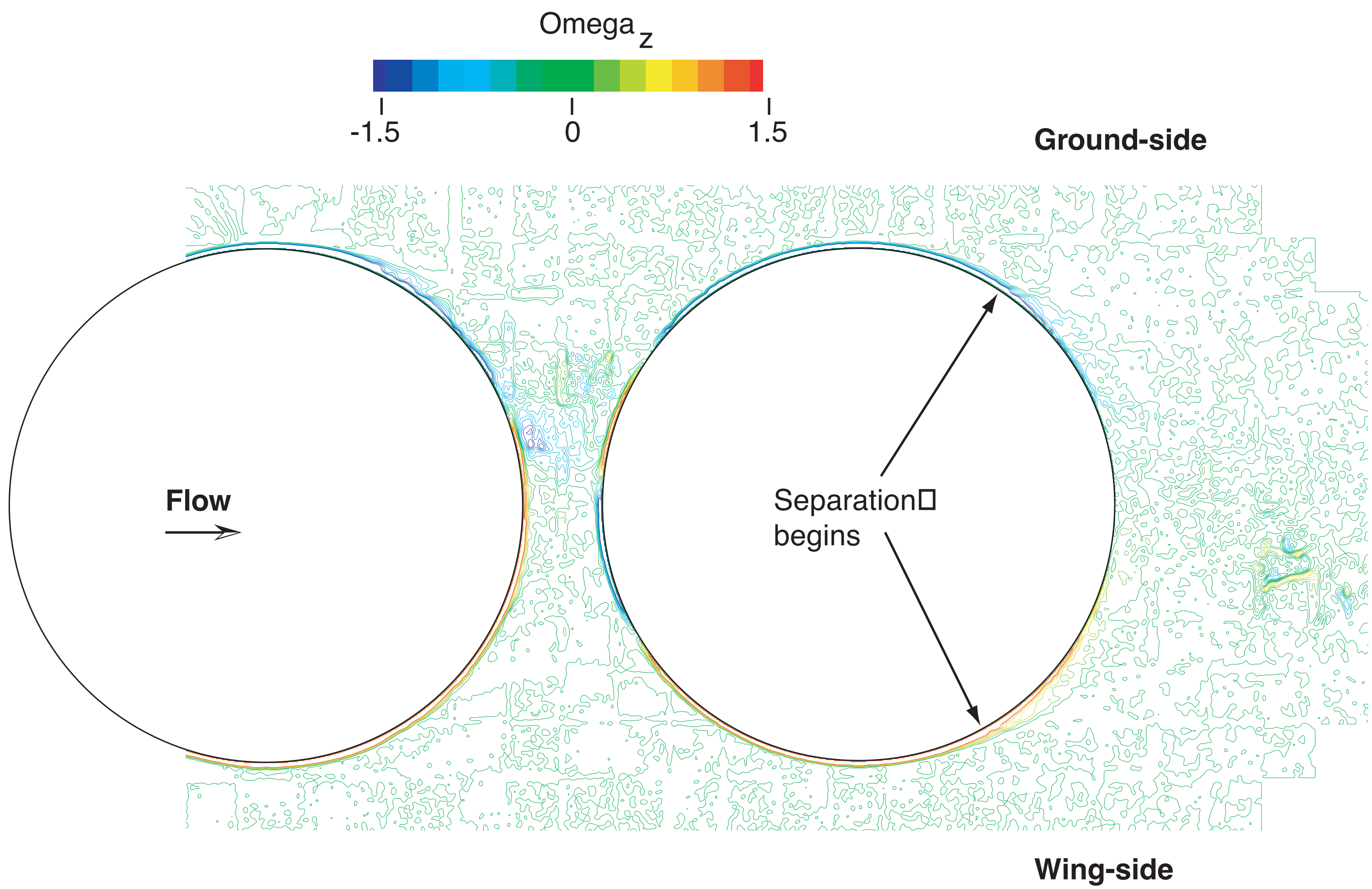

Figure 4.25 Vorticity field in DPIV data plane.

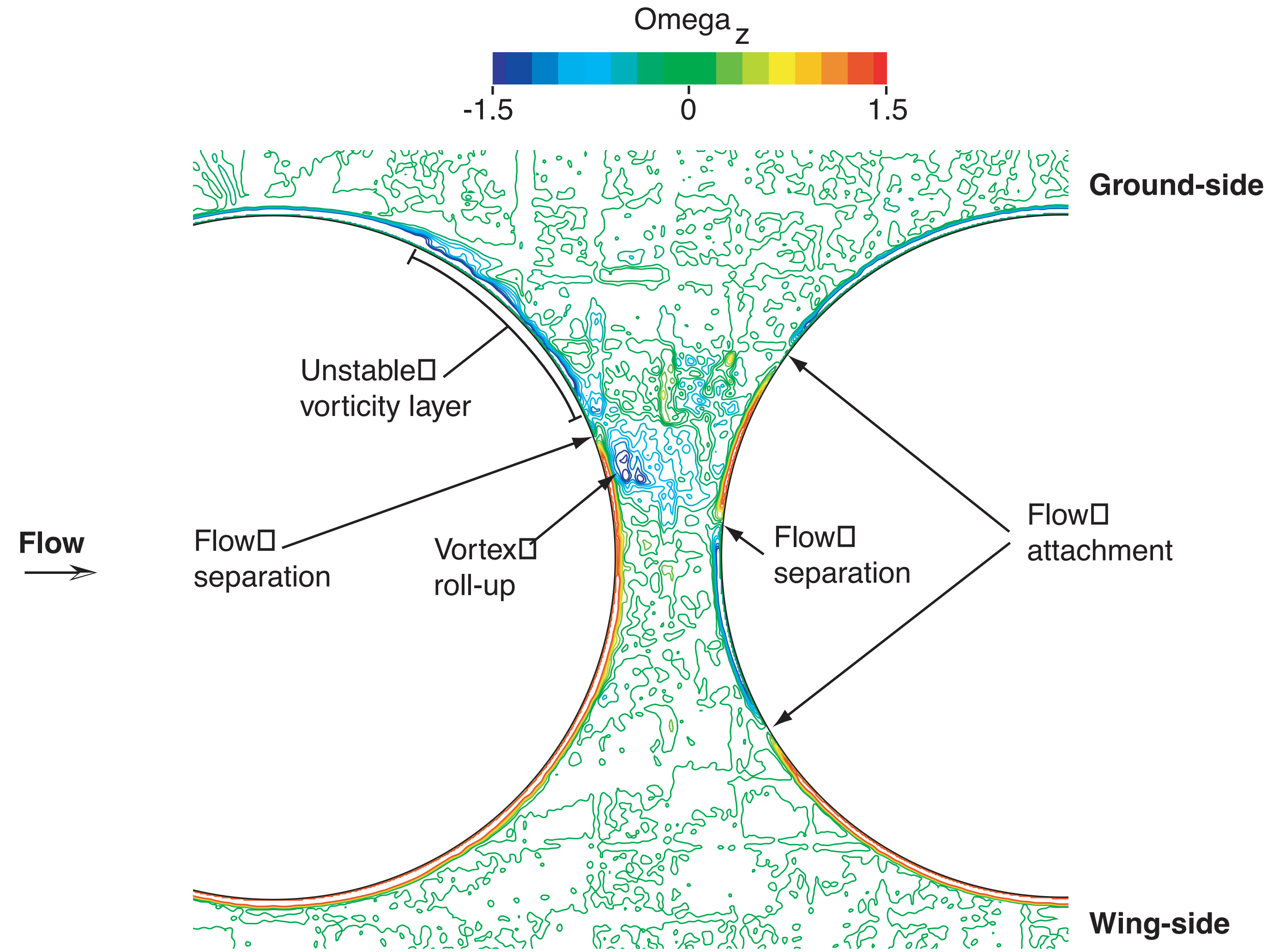

Figure 4.26 Vorticity field between wheels.

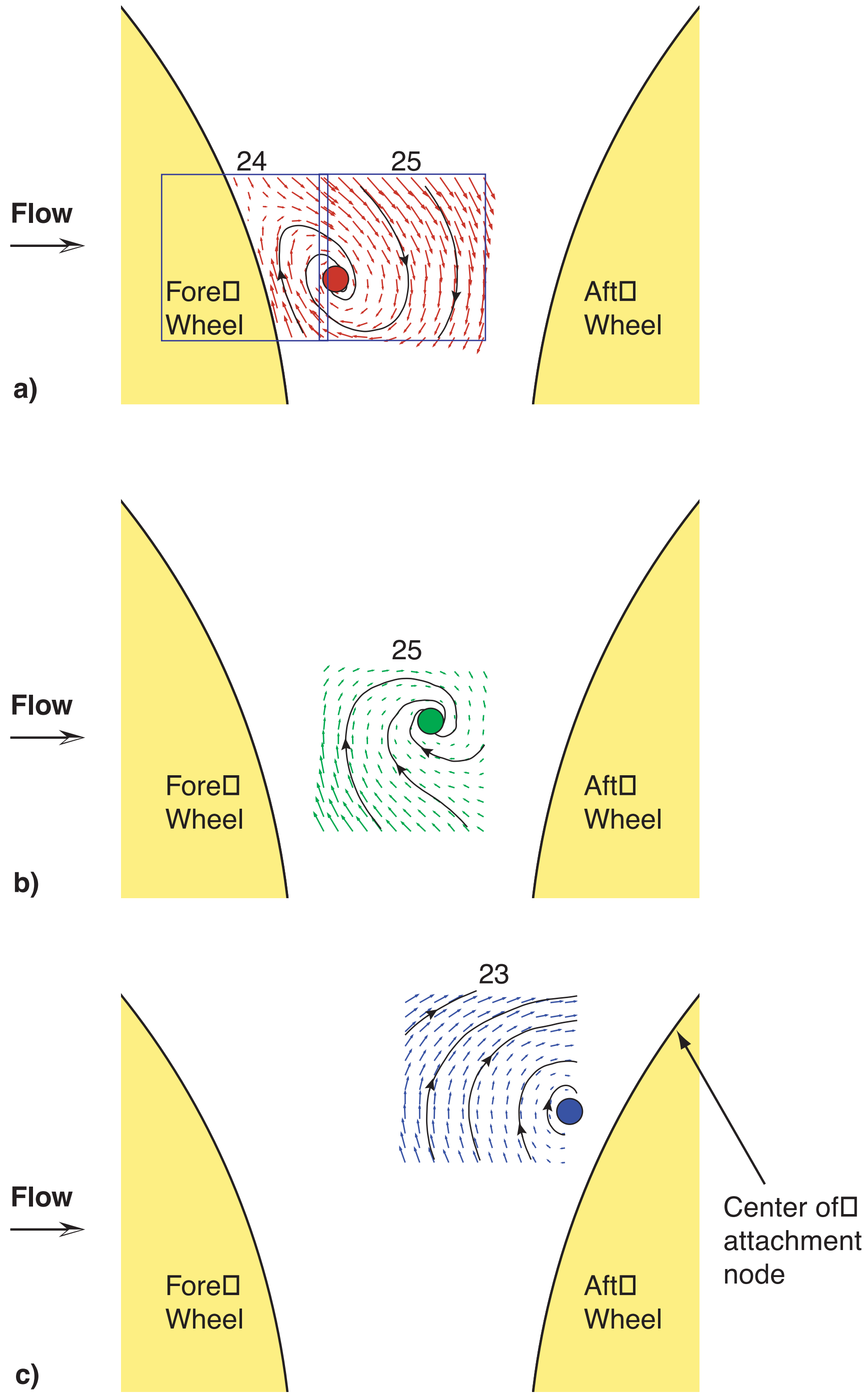

Figure 4.27 Position change of vortex between wheels.

5 Summary of Results and Recommendations

An understanding of the mean flow features associated with noise generation on a 4-wheel landing gear is a crucial step in a systematic approach to noise abatement. The present study is the first to identify these flow features by analyzing the flow field around a simplified version of the main landing gear on a Boeing 757. Two models and facilities were employed using test techniques appropriate for each facility.

The first was a 13% scale model installed in a water channel with a test section area of 33- x 30.5-centimeters. The Reynolds number based on wheel diameter was 15,000. Test techniques included dye visualization and particle path visualization in a vertical and horizontal plane. The second was as 31% scale model installed in the Basic Aerodynamics Research Tunnel (BART), which has a test section area of 71- x 102-centimeters. The Reynolds number based on wheel diameter in this facility was 600,000. Test techniques included surface oil flow visualization, mean surface static pressure measurements, and Digital Particle Image Velocimetry (DPIV).

5.1 Global, Qualitative Mean Flow Characteristics

Qualitative studies in the water channel provided a broad overview of the mean flow field around the model. Flow asymmetries were apparent in both the horizontal and vertical directions on the fore wheel. In the horizontal direction, asymmetry was apparent as the dye injected from the wheel surface, tended toward the outboard side of the wheel. In the vertical direction, there was a dramatic difference in separation location on the wing-and ground-sides of the fore wheel. Separation on the ground-side of the fore wheel occurred 18 degrees ahead of separation on the wing-side. These asymmetries are expected to be due, at least in part, to the asymmetric flow obstruction created by the center support strut on the wing-side of the model.

The difference in separation location on the wing- and ground-sides of the fore wheel significantly affected downstream flow conditions. Delayed separation on the wing-side directed the wing-side wake of the fore wheel through the gap between the fore and aft wheels. The flow that exited the gap region on the ground-side, formed a thick turbulent layer along the ground-side of the aft wheel. The energy introduced to the aft wheel surface flow through the turbulence in this layer, delayed separation of the boundary layer on the ground-side of the wheel; separation occurred at angles between 140 and 180 degrees around the wheel from its leading edge. This delay in separation resulted in a skew in the direction of the aft wheel wake toward the airframe.

The separation characteristics on the wing- and ground-sides of the fore wheel were found to be highly sensitive to very small, isolated surface protuberances. During the water channel tests a small air bubble attached itself to the ground-side of the fore wheel at the separation location. This resulted in a shift in the mean flow direction in the gap between the fore and aft wheels from a ground-ward direction to a wing-ward direction. Once the bubble was removed, the previously observed flow pattern was recovered. This suggests that separation conditions on the wing- and ground-sides of the fore wheel significantly affect the mean flow characteristics between the wheels.

5.2 Quantitative Characterization and Classification of Surface and Off-Surface Flow Patterns

Surface oil flow visualization in the wind tunnel experiments was aided by mean surface static pressure measurements. These studies allowed definition of surface streamline topologies associated with various types of flow separation and attachment. The geometric complexity of the present configuration resulted in combinations of basic topologies, i.e., surface flow patterns, that have not been previously addressed in the literature.

One particular interesting feature was the combination of two saddles of separation on the front face of the aft wheel. These were formed by surface streamlines from two separate attachment nodes that were directed toward the same point. In the region between the saddles, surface streamlines diverged and a significant rise in surface pressure was noted. Both of the features suggest flow was directed toward the wall in this region.

Another unanticipated feature that was identified involved a complex form of attachment. Two unexpected locations of flow attachment occurred on the backside of the fore wheel. One occurred along a positive bifurcation that was hypothesized to result from a Werlé-Legendre separation on the wing-side of the fore wheel. The other attachment was a node located just to the wing-side of the positive bifurcation.

It was discovered to result from flow separation from the front face of the aft wheel, which impinged upon the backside of the fore wheel.

The corresponding off-surface flow patterns were quantitatively determined using Digital Particle Image Velocimetry (DPIV). Results from the DPIV studies in a plane bisecting the in-line wheels identified flow features which would otherwise be indiscernible. The two attachment locations on the front of the aft wheel were discovered to be asymmetrically positioned around the wheel, with an offset of 5 degrees between the wing- and ground-sides of the wheel. This asymmetry is hypothesized to result from a corresponding 5 degree offset in flow separation location on the wing- and ground-sides of the fore wheel. Separation location differences on wing- and ground-sides of the fore wheel are hypothesized to result from measured differences in the azimuthal location and peak of the adverse pressure gradient on either side of the wheel.

Between the fore and aft wheels, a vortex was noted to persist. It is formed by flow separation from the front face of the aft wheel and interacts with the vorticity layer that separates from the backside of the fore wheel. This vortex pattern exists in accord with the asymmetry in attachment location on the front of the aft wheel. Evidence was also provided in these studies to suggest that the vortex does not remain at a stationary location between the wheels. Individual, as well as averaged velocity vector images from the DPIV data have identified a shift in location of the vortex that is hypothesized to result from observed, erratically changing separation characteristics on the ground-side of the fore wheel.

Finally, the present study has identified several regions about the surface of the wheel, and their associated flow features, that are likely to produce significant levels of noise. The most noteworthy is the ground-side of the gap region between the fore and aft wheels. As mentioned above, a vortex was noted to persist here and shift to different positions within the gap region. The ground-side position of this vortex makes it especially significant, since any noise it generates will be directed ground-ward. Two mechanisms of noise production may be associated with this vortex: direct interaction with the wheels as it rotates near them, and impingement on the wheels as it changes position between them.

5.3 Recommendations for Further Study

Considering the aforementioned observations, there is potential for further investigation of unresolved issues. The following recommendations are made:

(i) *Reynolds Number Dependence* Characterization of the mean flow features around the present configuration at two different Reynolds numbers has highlighted some associated differences. Some differences might also be expected as flight Reynolds numbers are approached. At the highest Reynolds number presently studied, topological surface features on the wing- and ground-sides of the fore wheel, suggest laminar separation conditions. At flight Reynolds numbers, turbulent separation conditions are expected. This may result in some changes in the mean flow features that alter the noise producing mechanisms associated with this configuration. A study of the mean flow features around a configuration similar to the present, at flight Reynolds numbers, is therefore recommended.

(ii) *Fluctuating Surface pressures* The most important mechanism of flow noise generation for the present configuration is the contact of a fluctuating flow field with a solid surface. This produces pressure fluctuations that are sufficiently energetic results in broadband noise of high amplitude. In the present study, regions of flow attachment and separation were identified, but information on the pressure fluctuations associated with these locations would be valuable. In order to narrow down the most significant regions of flow noise generation around the present configuration, the fluctuating pressures on the wheel surfaces should be determined.

(iii) *Dynamics of Vortex Between Wheel* The present study has verified the persistence of a vortex on the ground-side of the gap region between the fore and aft wheels. This vortex is expected to play a significant role in noise production as it rotates near the surface of each wheel and shifts position within the gap. Further details of the vortex dynamics including its formation, motion within the gap region and possible loss of organized structure would be helpful in validating its importance as a noise source.

5.4 Noise Abatement Considerations.

Noise abatement with the current configuration is a difficult issue since wheels must be round and it is the bluff body feature of the wheels that is significantly problematic. However, the present study has identified the gap region between the fore and aft wheels as a significant source of noise. In this region, flow, postulated to be turbulent, attaches to the backside of the fore wheel and the front side of the aft wheel. A vortex has also been discovered to persist in this region with significant noise producing capability. Therefore, in order to effect the greatest reduction in noise, we might constrain our noise abatement considerations to this region. To that end, the following noise reduction measures are proposed:

(i) To directly affect the existing flow field between the wheels, one solution would be to break up the mean flow structure by introducing an obstruction. Such an obstruction could be as obtrusive as a solid body conformed to the shape of the wheels or as obscure as an array of loosely fitted strings attached to rods located at the wing- and ground-sides of the wheels.

(ii) Alterations could be made to the existing 4-wheel configuration, such as adjusting the relative spacing between the in-line wheels to affect flow interaction between them. A rotation of the 4-wheel arrangement might also be considered such that the fore wheels are positioned overtop of the aft wheels during initial aircraft approach. This would eliminate the flow characteristics of the in-line wheels altogether. As the ground is approached, the wheel arrangement could be mechanically rotated into position, or rotation could result freely as the aft wheels contacted the ground. Variations in wheel size might also be considered. By reducing the size of the aft wheels and moving them closer to the fore wheels, a more aerodynamic wheel combination would result.

(iii) Finally, the 4-wheel configuration could be eliminated altogether by replacing it with a 3-wheel configuration. This would eliminate the flow characteristics of the in-line wheels, with the added benefit of aircraft weight reduction.

References

Adrian, R. J. (1991) Particle-Imaging Techniques for Experimental Fluid Mechanics, Annual Review of Fluid Mechanics, vol. 23, pp. 261-304.

Bliss, D. B. & Hayden, R. E. (1976) Landing Gear and Cavity Noise Prediction. NASA CR-2714.

Block, P. J. W. (1997) An Experimental Investigation of Airframe Component Interference Noise. AIAA-77-56.

Cabral, B. & Leedom, L. (1993) Imaging Vector Fields Using Line Integral Convolution. Computer Graphics Proceedings '93, ACM SIGGRAPH, pp. 263-270.

Chapman, G. T. (1986) Topological Classification of Flow Separation on Three-Dimensional Bodies. AIAA Paper 86-0485

Chapman, G. T. & Yates, L. A. (1991) Topology of Flow Separation on Three-Dimensional Bodies. Appl. Mech. Rev., vol. 44, no. 7, pp. 329-345.

Chong, M. S. & Perry, A. E. (1986) Synthesis of Two- and Three-dimensional Separation Bubbles. Australasian Fluid Mechanics Conference, 9th, Auckland, New Zealand, Dec. 8-12, 1986, Proceedings (A88-32526 12-34).

Coon, M. D. & Tobak, M. (1995) Experimental Study of Saddle Point of Attachment in Laminar Juncture Flow. AIAA-95-0785.

Crighton, D. G. (1991) Airframe Noise. NASA Reference Publication 1258, vol. 1, WRDC Technical Report 90-3052, Aeroacoustics of Flight Vehicles: Theory and Practice, Ed. Hubbard, H. H.

Curle, N. (1955) The influence of Solid Boundaries Upon Aerodynamic Sound. Proc. Roy. Soc., vol. A 231, pp. 505-514.

Dallmann, U., Hilgenstock, A., & Reidelbauch, S. (1990) On the Footprints of Three-Dimensional Separated Vortex Flows Around Blunt Bodies. AGARD-CP-494.

Dobrzynski, W. M. & Buchholz, B. (1997) Full-Scale Testing on airbus Landing Gears in the German Dutch Wind Tunnel. AIAA-97-1597-CP.

Eckerle, W. A. & Langston, L. S. (1987) Horseshoe Vortex Formation Around a Cylinder. ASME Journal of Turbomachinery, Vol. 109, pp. 278-285.

Fink, M. R. (1977) Airframe Noise Prediction Method. FAA-RD-77-29.

Gibson, J. S. (1972) The Ultimate Noise Barrier - Far Field Radiated Aerodynamic Noise, INTER-NOISE 72 Proceedings, pp. 332-337, Oct. 6, 1972, Washington, D. C.

Gibson, J. S. (1974) Nonengine Aerodynamic Noise Investigation of a Large Aircraft. NASA CR-2378.

Hardin, J. C., Fratello, D. J., Hayden, R. e., Kadman, Y., & Africk, S. (1975) Prediction of Airframe Noise. NASA TN D-7821.

Hayden, R. E., Kadman, Y., Bliss, D. & Africk, S. (1975) Diagnostic Calculation of Airframe Radiated Noise. AIAA Paper No. 75-485.

Healy, G. J. (1974) Measurement and Analysis of Aircraft Far-Field Aerodynamic Noise. NASA CR-2377.

Hersh, A. S. , Putnam, T. W. , Lasagna, P. L. and Burcham, F. W. jr. (1976) Semi-

Empirical Airframe Noise Prediction Model. AIAA Paper No. 76-527.

Heller, H. H. & Dobrzynski, W. M. (1977a) Sound Radiation from Aircraft Wheel-Well/Landing Gear Configurations. Journal of Aircraft, vol. 14, no. 8, pp. 768-774.

Heller, H. H. & Dobrzynski, W. M. (1977b) Unsteady Surface Pressure Characteristics on aircraft Components and Farfield Radiated Airframe Noise. AIAA Paper 77-1295. 4th AIAA Aero-Acoustics Conference, Atlanta, GA., Oct. 3-5, 1977.

Heller, H. H. & Dobrzynski, W. M. (1978) A Comprehensive Review of Airframe Noise Research. Presented at the 11th Congress of the International Council of the Aeronautical Sciences (ICAS), Lisboa, Portugal, 10-16 September 1978. vol. 1, Eds.: Singer J. & Staufenbiel, R.

Hornung, H. & Perry, A. E. (1984) Some Aspects of Three-Dimensional Separation, Part I: Streamsurface Bifurcations. Zeitschrift fuer Flugwissenschaften und Weltraumforschung. vol. 8, pp. 77-87.

Hunt, J. C. R., Abell, C. J., Peterka, J. A. & Woo, H. (1978) Kinematical Studies of the Flows Around Free or Surface-Mounted Obstacles; Applying Topology to Flow Visualization. J. Fluid Mech. Vol. 86, pp. 179-200.

Joint DOT-NASA (1971) Civil Aviation Research and Development (CARD) Policy Study. DOT TST-10-5 and NASA SP-266.

Landreth, C. C. & Adrian, R. J. (1988) Measurement and Refinement of Velocity Data using High Image Density Analysis in Particle Image Velocimetry. Applications of Laser Anemometry to Fluid Mechanics: Proceedings of the 4th International Symposium, edited by R. J. Adrian, T. Asunuma, D. Durão, F. Durst, & J. Whitlaw, Springer-Verlag, Berlin, pp. 484-497.

Legendre, R. (1965) Lignes de courant d'un écoulement continu. La Recherche Aérospatiale, Vol. 105, pp. 3-9.

Lighthill, M. J. (1952) On sound Generated Aerodynamically, Proc. Roy. Soc., vol. a 221, pp. 564-587.

Lighthill, M. J. (1954) Turbulence as a Source of Sound. Proc. Roy. Soc., vol. A 222, pp. 1-32.

Lighthill, M. J. (1963) In *Laminar Boundary Layers* (Ed. L. Rosenhead), pp. 48-88. Oxford University Press.

Meinhart, C. D., Barnhart, D. H. & Adrian R. J. (1994) Interrogation and Validation of Three-Dimensional Vector Fields. In Developments in Laser Techniques and Applications to Fluid Mechanics, R. J. Adrian et al. (Eds.), Springer-Verlag, Berlin, pp. 379-391.

Peake, D. J. & Tobak, M. (1982) Three-Dimensional Separation and Reattachment. AGARD-LS-121.

Perry, A. E. & Chong, M. S. (1986) A Series-Expansion Study of the Navier-Stokes Equations with Applications to Three-dimensional Separation Patterns. J. Fluid Mech. Vol. 173, pp. 207-203.

Perry, A. E. & Chong, M. S. (1987) A Description of Eddying Motions and Flow Patterns Using Critical-Point Concepts. Ann. Rev. Fluid Mech., Vol. 19, pp. 125-155.

Perry, A. E. & Fairlie, B. D. (1974) Critical Points in Flow Patterns. Proceedings of Turbulent Diffusion in Environmental Pollution. Vol. 18B, pp. 299-314, Eds.: Frenkiel, F. N. & Munn, R. E.

Pierce, F. J. & Tree, I. K. (1990) the Mean Flow Structure on the Symmetry Plane of a Turbulent Junction Vortex. ASME Journal of Fluids Engineering, Vol. 112, pp. 16-22.

Preisser, J. S. (1980) Airframe Noise Measurements on a Supersonic Transport Small-Scale Model. Journal of Aircraft, vol. 17, no. 11, pp. 795-801.

Putnam, T. W., Lasagna, P. L. & White, K. C. (1975) Measurements and Analysis of Aircraft Noise. AIAA Paper No. 75-510.

Revell, J. D., Healy, D. J. & Gibson, J. S. (1975) Methods for the Prediction of Airframe Aerodynamic Noise. AIAA Paper No. 75-539.

Seal, C. V., Smith, C. R., Akin, O. & Rockwell D. (1995) Quantitative Characteristics of a Laminar, Unsteady Necklace Vortex System at a Rectangular Block-Flat Plate Juncture. J. Fluid Mech., Vol. 286, pp. 117-135.

Sen, R. (1996) Private communication.

Squire, L. C. (1962) The Motion of a Thin Oil Sheet Under the Boundary Layer on a Body. AGARDOgraph 70.

Tobak, M. & Peake, D. J. (1982) Topology of Three-Dimensional Separated Flows. Ann. Rev. Fluid Mech., vol. 14, pp. 61-85.

Visbal, M. R. (1989) Structure of Laminar Juncture Flows. AIAA-89-1873.

Werlé, H. (1962) Separation on Axisymmetrical Bodies at Low Speed. La Recherche Aéronautique, Vol. 90, pp. 3-14.

Willert, C. E. & Gharib, M. (1991) Digital Particle Image Velocimetry. Experiments in Fluids vol. 10, pp. 181-193.

Vita

Barry S. Lazos was born on June 1, 1957 in Memphis, Tennessee to Paul A. and Christine S. Lazos. After graduating from Norfolk Christian High School in June 1975, the author began working as a Mercedes Benz auto mechanic until 1979 when he began studies at Old Dominion University in Norfolk, Virginia. During his college career he worked four co-op terms, one for IBM in Owego, New York and three at the NASA Langley Research Center in Hampton, Virginia. In May, 1985 he graduated magna cum laude with a Bachelor of Science in Mechanical Engineering. He began working full time as a research scientist at NASA Langley in June, 1985, specializing in turbulent boundary layer modification for drag reduction. In August, 1986 he began part time graduate work at the George Washington University graduate extension in Hampton, Virginia and received a Masters of Science in May, 1993. He was then accepted as a doctoral candidate in the Department of Mechanical Engineering and Mechanics at Lehigh University in September 1993.

The author's publications include:

Wilkinson, S. P.; Anders, J. B.; Lazos, B. S.; Bushnell, D. M. (1987) Turbulent drag reduction research at NASA Langley: Progress and plans. Int. J. Heat and Fluid Flow, vol. 9, no. 3, pp. 266-277.

Wilkinson, S. P. & Lazos, B. S. (1987) Direct drag and hot-wire measurements on thin-element riblets. IUTAM Symposium on Turbulence Management and Relaminarization, Bangalore, India, Jan19-23.

Wilkinson, S. P. & Lazos, B. S. (1987) Near-wall turbulence alteration through thin streamwise riblets. IUTAM Symposium on Turbulence Management and Relaminarization, Bangalore, India, Jan19-23.

Wise, M. A. & Lazos, B. S. (1988) Robotic tool-exchange system. NASA Tech. Brief LAR-13558.

Lazos, B. S. & Wilkinson, S. P. (1988) Turbulent viscous drag reduction with thin-element riblets. *AIAA Journal*, vol. 26, no. 4, pp. 496-498.

Lazos, B. S. (1989) Effects of contamination on riblet performance. *J Aircraft*, vol. 26, no. 7, pp. 684-686.

Lazos, B. S. (1993) An Experimental investigation of the structural features of a shear-driven 3-D turbulent boundary layer. Masters Thesis, George Washington Univ.

The authors referenceable oral presentations include:

Lazos, B. S. & Wilkinson, S. P. (1987) Turbulent viscous drag reduction and related mechanisms with thin-element riblet arrays. Presented at the Sixth Engineering Mechanics Specialty Conference sponsored by the Engineering Mechanics Division of the American society of Civil Engineers and the Buffalo Section of ASCE. State University of New York at Buffalo, Buffalo, New York, May 20-22, 1987.

Lazos, B. S. & Robinson, S. K. (1991) Coherent structures in a 3-D turbulent boundary layer. Presented at the 44th annual meeting of the Division of Fluid

Dynamics of the American Physical Society, Arizona State University, November 24-26 1991.